Torque Modulation and Self-Sensing for Separately Excited Synchronous Electrostatic Machines

By

Aditya N. Ghule

A dissertation submitted in partial fulfillment of

the requirements for the degree of

Doctor of Philosophy

(Electrical Engineering)

at the

UNIVERSITY OF WISCONSIN-MADISON

2019

Date of final oral examination: October 31, 2019

The dissertation is approved by the following members of the Final Oral Committee:
Daniel C. Ludois, Associate Professor, Electrical and Computer Engineering
Thomas Jahns, Professor, Electrical and Computer Engineering
Bulent Sarlioglu, Associate Professor, Electrical and Computer Engineering
Eric L. Severson, Assistant Professor, Electrical and Computer, Mechanical Engineering

Abstract

The development of electrostatic machines with torque densities comparable to air-cooled electromagnetic machines (1.5 $^{N\text{-}m}/_{Kg}$) has driven the need for medium voltage drive systems. However, there are no off-the-shelf medium voltage drives at this power level and the appropriate control framework for these new machines has yet to be established. This thesis presents a physics-based approach towards the development of a control framework for electrostatic machines. Key research objectives include experimental demonstration of high bandwidth torque modulation and development of methodologies for rotor position self-sensing. Self-sensing may also be called sensorless control in this field of study.

An approach based on understanding the duality between electrostatic machines and electromagnetic machines is pursued for drive and control development. Methods for controlling the terminal voltage of the electrostatic machine are investigated. A complex vector synchronous frame PI regulator is proposed for controlling machine terminal voltage. The controller is implemented on a medium voltage current source inverter to drive an electrostatic machine. Dynamic performance of the voltage regulator is experimentally verified by evaluation of the controller frequency response function and dynamic stiffness. Electrostatic machine torque modulation using charge oriented control is experimentally demonstrated.

Both model based methods and injection based methods are investigated for esti-

mation of rotor position. Rotor position at medium and high speeds is estimated from back-mmf signal based self-sensing. The back-mmf (or a back-current) signal is extracted from a voltage observer developed using the machine model. Zero and low speed position self-sensing is achieved using high frequency signal injection based self-sensing which takes advantage of the separate excitation to track a high frequency signal injected on the machine stator resulting in high precision self-sensing without additional hardware. Closed loop voltage and speed control operation is experimentally demonstrated. Key advantages and challenges involving rotor position self-sensing implementation with an electrostatic machine are discussed.

Acknowledgements

I have been fortunate to have had an opportunity to study at the University of Wisconsin-Madison. I take this opportunity to humbly acknowledge all those, without whose support this thesis would not have been possible.

First, I would like to express my deepest appreciation for my advisor Prof. Daniel C. Ludois for his support and guidance throughout the research project. I thank him for introducing me to electrostatic machines and giving me the opportunity to work on such an interesting project. His patient and constructive feedback on all aspects of the project ranging from experimental setup development to writing has been an invaluable learning experience. I could not have asked for a better experience for my PhD.

I would like to thank my committee members Prof. Jahns, Prof. Sarlioglu and Prof. Severson for their time and valuable feedback.

I would like to thank Prof. Lorenz for introducing me to the field of physics-based control design. His guidance during my masters project has been instrumental in developing my understanding of motor control systems.

I am indebted to those in Prof. Ludois's research group. Many thanks to Baoyun Ge and Peter Killeen for the insightful discussions and collaboration on the electrostatic machine project. I would like to thank Ryan Knippel and Skylar Hagen for their guidance and suggestions in using the machining tools for prototyping. I would like to thank the team at C-Motive Technologies for their help and valuable support during the project.

I would like to thank Kyle Hanson for his recommendations while developing experimental setup. I thank Helene Demont and Kathy Young for the continuous support and being a very important part of my WEMPEC experience.

I would like to thank my WEMPEC peers Kevin Frankforter, Seth McElhinney, Adam Shae, Perry Channegowda, Andy Schroedermeier, Kang Wang, Huthaifa Flieh, Ashray Manur, Mahima Gupta, Wenbo Liu, Dheeraj Bobba, Ryoko Imamura, James Swanke and many others for their support and the stimulating discussions. Special thanks to all the

current and past residents of 2568 and 1548 Engineering Hall. I would like to thank Tim Slininger, Marc Petit, Peter Killeen and Apoorva Athavale for taking the time to review parts of this work and offer valuable feedback.

I thank Dr. Ajit Patwardhan and Dr. Vinod Walivadekar for their guidance. I thank Dr. Dave Seidl from Unico, Inc. for his guidance. I would like to thank my teachers from my undergraduate education Dr. Dharme and Dr. Talange for their guidance all the way from my introduction to the field of electrical engineering.

To my friends in Madison: thank you for making my stay in Madison memorable. Abhishek, Pranali and Nishant, thank you for being a constant source of support in Madison for almost a decade. My friends Aditya, Ketan, and Akshay, thank you for always encouraging me. Rika and Ranga thank you for always being there, even after moving out of Madison. I take this opportunity to thank my friends from India, Mihir, Pratik, Harshawardhan, Salil and Kaustubh for keeping me motivated from across the globe.

Finally, I would like to express my deepest gratitude to my family - my parents Sujata and Nandakumar Ghule, without whose support I would not be here today and my grandparents Sunanda and Dr. Hari M. Ghule for always believing in me . Whatever I am today is all because of you. A special thanks to my aunt and uncle: Sushma and Vijay Bokil, and cousins Neha and Ameya, I could not have done this without you.

Table of Contents

Page

List of Tables **viii**

List of Figures **ix**

List of DSP and MATLAB Codes **xvi**

Introduction **xix**

Motivation xix

Summary of Chapters xxiii

1 A review of the State of the Art **1**

1.1 Electrostatic Torque Production 1

1.2 Types of Rotating Electrostatic Machines 2

1.3 Electrostatic Machine Design 5

1.4 Electrostatic Machine Torque Modulation 10

1.5 Chapter Summary and Research Opportunities 13

2 Drive Development for Electrostatic Machines **16**

2.1 Duality between Electrostatic and Electromagnetic Machine Dynamics . 16

2.2 Charge Oriented Control 20

2.3 Power Electronics for Electrostatic Drive 21
2.4 Power Electronic Device Considerations for Electrostatic Drives 26
2.5 Steady State Drive Limit Curves 28
2.6 Summary 34

3 Torque Modulation for SEM **36**
3.1 A review of the State of the Art 36
3.2 Complex Vector Modeling of SEM 40
3.3 Voltage Regulation for a Capacitive Load 43
3.4 Voltage control for SEM 44
3.5 Complex Vector Voltage Regulation in the Discrete Time Domain 47
3.6 Experimental Verification of Torque Modulation 48
3.7 Voltage Regulator Performance 55
3.8 Voltage Regulation for Salient Pole Machines 62
3.9 Summary 62

4 Rotor Position Self-Sensing **64**
4.1 Introduction 64
4.2 A Review of Self-Sensing Methodologies 66
4.3 Self-Sensing for Separately Excited Electrostatic Machines 71
4.4 Back-MMF Based Self-Sensing 73
4.5 High Frequency Signal Injection Based Self-Sensing for SEM 82
4.6 Saliency based self-sensing 96
4.7 Wide Operating Range Self-Sensing 99
4.8 Self-Sensing Implementation Challenges 101
4.9 Summary 102

5 Conclusions, Contributions and Recommended Future Work 103

5.1 Conclusions 103

5.2 Contributions 105

5.3 Recomended Future Work 108

Bibliography 111

Appendix A Parameter Estimation for Electrostatic Machines 121

A.1 A review of the State of the Art 121

A.2 Steady State Parameter Estimation for SEM 122

A.3 Summary 124

Appendix B Firmware Development for SEM Control Platform 125

B.1 Space Vector Modulation Configuration for CSI 125

B.2 Front-End PWM Configuration 130

B.3 Voltage Regulator 132

B.4 Self-Sensing 133

Appendix C Steady State Performance Curves for SEM 134

C.1 Stator Side Field Weakening 134

C.2 Rotor Side Field Weakening 137

List of Tables

TABLE		Page
1	Comparison of Copper Loss at Holding Torque	xxiii
1.1	Comparison of performance metrics of different types of electrostatic machines	9
1.2	Summary of machine control methods used by prior researchers.	13
2.1	Comparison of medium voltage drive topologies	27
3.1	SEM1 Specifications.	48
3.2	$BSH1003P11A2A$ Specifications.	48
3.3	Dyno Drive Specifications.	49
3.4	Controller Gains for FRF evaluation.	56
3.5	Controller Gains for DS evaluation.	58
4.1	Encoder Cost Comparison.	66
4.2	Motion controller and position tracking observer eigen values, and filter bandwidths	89
B.1	Sector Changes	125

List of Figures

FIGURE		Page
1	Electricity consumption in commercial and industry applications with shaded portion showing share of electricity consumed by electric motors[1]	xx
1.1	Electrostatic Induction machine	3
1.2	Variable elastance machine	4
1.3	Separately excited synchronous machine	4
1.4	Front view of SEM1 [2]	9
1.5	Back view of SEM1 [2]	9
1.6	Opamp based drive system for electrostatic induction micromotor[3]	10
1.7	Torque Vs Speed for an Electrostatic Induction Machine[3]	11
1.8	Motor drive circuit[4]	12
1.9	Motor operation plots[4]	12
2.1	Circuit model for a) Electromagnetic machine, b) Electrostatic machine.	17
2.2	Phasor diagram for a salient pole synchronous electrostatic machine	20
2.3	Voltage regulator block diagram	21
2.4	CSI with an electrostatic machine model	22
2.5	VSI with an electrostatic machine model	23
2.6	Block diagram for control of SEM using a high voltage VSI	24

2.7 Low voltage VSI with step up transformers and an electrostatic machine model 25
2.8 Block diagram for control of SEM using a low voltage VSI with step-up transformers 26
2.9 Semiconductor device ratings from Digikey [5] 28
2.10 Machine currents, voltages,torque, power and power factor limit curves with field weakening at $I_{bus} = 200mA$, $V_{lim} = 4000V$ and $V_{fd} = -8000V$ 30
2.11 Machine dq-axis and field voltage during field weakening with $I_{bus} = 200mA$, $V_{lim} = 4000V$ and $V_{fd} = -8000V$ 31
2.12 Machine dq-axis and total current during field weakening with $I_{bus} = 200mA$, $V_{lim} = 4000V$ and $V_{fd} = -8000V$ 31
2.13 Circle diagram for stator side field weakening 32
2.14 Machine currents, voltages,torque, power and power factor limit curves with field weakening implemented by reducing rotor field voltage at $I_{bus} = 200mA$, $V_{lim} = 4000V$ and $V_{fd} = -8000V$ 33
2.15 Circle diagram for rotor side field weakening 34

3.1 Block diagram of a voltage-controlled CSI [6] 38
3.2 Stationary and synchronous reference frames 41
3.3 Electro-mechanical block diagram of a three phase separately excited synchronous electrostatic machine shown in the synchronous reference frame 41
3.4 Complex vector block diagram of a non-salient synchronous electrostatic machine with the back-mmf decoupled, shown in the synchronous reference frame 43
3.5 Bock diagram of an RC load with a synchronous reference frame PI voltage regulator, shown in the synchronous reference frame 44

3.6 Complex Vector Voltage Regulator block diagram for a three-phase RC load, shown in the synchronous reference frame 45
3.7 Complex Vector Voltage Regulator block diagram the SEM with the back-mmf decoupled, implemented in the synchronous reference frame 45
3.8 Pole migration for CVVR shown in the synchronous reference frame 46
3.9 Frequency response function magnitude and phase in the synchronous reference frame with varying synchronous frequency. Tuned to a 150 Hz bandwidth..... 46
3.10 Electrostatic machine test setup showing SEM, load motor and torque transducer..... 49
3.11 Block diagram showing experimental setup comprising of SEM, load motor and torque transducer..... 50
3.12 TI 28379D Control Card 51
3.13 SVM hexagon showing the six sectors for CSI-PWM 52
3.14 EMCO-FS40 High voltage power supply used for rotor excitation 53
3.15 CSI Drive hardware configuration for SEM testing showing the front-end with the CSI and the SEM equivalent circuit 54
3.16 Circuit diagram of passive snubber circuit for voltage balancing and hard-ware realization of the series-stack switch..... 54
3.17 Orthogonal components of a linear rotating chirp signal with frequency varying from zero to 100 Hz..... 56
3.18 Experimental complex vector FRF for a complex vector synchronous frame PI regulator with f_{bw} = 150 Hz for f_e = 30 and 100 Hz..... 57
3.19 Complex vector synchronous frame PI voltage regulator with disturbance current injection for disturbance 58

3.20 Experimental complex vector dynamic stiffness for a complex vector synchronous frame PI regulator with f_{bw} = 150 Hz and f_{bw} = 300 Hz for f_e = 30Hz (18.75 rpm) 59
3.21 Experimental evaluation of torque command tracking response showing scaled q-axis voltage command in the synchronous reference frame and measured shaft torque at stall with V_{fd} = 5 kV 60
3.22 Experimental evaluation of torque command tracking response showing scaled q-axis voltage command in the synchronous reference frame and measured shaft torque at f_e = 50 Hz (31.25rpm), 100 Hz (62.5rpm) and 150 Hz (93.75rpm) with V_{fd} = 3 kV..... 61
3.23 Bock diagram of an RC load with a synchronous reference frame PI voltage regulator, shown in the synchronous reference frame 63

4.1 Visual representation of a (left) 8-pole rotor and a (right) 96 pole rotor where each black segment is a rotor pole 65
4.2 Self-sensing methodologies for separately excited electrostatic machines ... 71
4.3 Back-mmf state filter shown in the stationary reference frame..... 74
4.4 Position tracking observer shown in discrete time for extraction of position signal using back-mmf signals 75
4.5 Block diagram of position estimation using back-mmf self-sensing 75
4.6 Estimated back-mmf using back-mmf state filter at V_{qs}^{e} =0 V, I_{bus} =100 mA, V_{fd} = 2.5kV, with machine held at constant speed of (top) 60 rpm (96 Hz) and (bottom) 90 rpm (144 Hz)..... 76
4.7 Measured and estimated speed using using back-mmf based self-sensing at V_{qs}^{e} =0 V, I_{bus} =100 mA, V_{fd} = 2.5kV, with machine held at constant speed of (top) 60 rpm (96 Hz) and (bottom) 90 rpm (144 Hz) 77

4.8 Effect of inverter harmonics on back-mmf based position estimation showing estimated q-axis back-mmf with the machine held at a constant speed of 60 rpm (96 Hz) and rotor voltage V_{fd} = 2.5 kV at inverter voltage top: V_{qs}^{e} =0 V, center: V_{qs}^{e} =250 V, bottom: V_{qs}^{e} =500 V..... 78

4.9 Harmonic spectrum of estimated back-mmf with V_{qs}^{e} =500 V, I_{bus} =100 mA, V_{fd} = 2.5kV, with machine held at constant speed of 60 rpm (96 Hz) 79

4.10 Closed loop torque control using back-mmf based self-sensing showing (top) the measured, estimated position and the position estimation error and (bottom) the q-axis voltage command, response and measured torque with the machine rotating at a constant speed of 60rpm (96Hz) and a field voltage of 2.5 kV 80

4.11 Block diagram of injection based self-sensing with high frequency signal injected on the rotor and resulting signal measured on the stator 82

4.12 Block diagram of injection based self-sensing with high frequency signal injected on the stator and resulting signal measured on the rotor 83

4.13 Equivalent circuit model of the SEM showing machine q-axis (top) and d-axis (bottom), shown in the synchronous reference frame 83

4.14 Measured spectrum of the voltage signal measured at the rotor terminals showing the (top) full spectrum and (bottom) zoomed in spectrum at ω_e = 32 Hz (20 rpm) and 20 mA carrier current at f_c = 750 Hz under no load and a 3.5 kV DC field voltage removed using high-pass filer placed at 100 Hz..... 86

4.15 Signal demodulation and position tracking observer for extracting rotor position and speed using injection signal based self-sensing..... 87

4.16 Block diagram of system implementation of closed loop speed control of SEM using injection based self-sensing..... 89

4.17 Measured and estimated electrical position with V_{qs}^{e} = 0 V with machine rotating at 20 rpm (32 Hz) with an injected signal of 30 mA 90
4.18 Measured and estimated mechanical position with V_{qs}^{e} = 0 V with machine rotating at 20 rpm (32 Hz) with an injected signal of 30 mA 91
4.19 Measured and estimated electrical position with V_{qs}^{e} = 500 V with machine rotating at 20 rpm (32 Hz) with an injected signal of 30 mA 92
4.20 Measured and estimated mechanical position with V_{qs}^{e} = 500 V with machine rotating at 20 rpm (32 Hz) with an injected signal of 30 mA. 93
4.21 Closed loop speed control using a) encoder feedback and b) Estimated position with an injected signal of 30 mA with V_{fd} = 2.5 kV 94
4.22 Actual and computed delay using 4.19 95
4.23 Filter phase delay compensation showing improvement in estimated position error with rotor voltage $V_{fd} = 2.5\ kV$ 96
4.24 Negative sequency component of the injection frequency voltage (top) and measured electrical position(bottom) with the machine held a constant speed of 12rpm (19.2 Hz) with an injected signal of 10 mA at a frequency of 450 Hz 97
4.25 Saliency tracking observer to estimate position based on saliency based self-sensing 98
4.26 Block diagram of system implementation of wide operating range self-sensing 99
4.27 Rotor position estimation over a wide speed range using injection based self-sensing below 45 rpm and using back-mmf based self-sensing at high speed with an injection current of 20mA at f_c = 750 Hz 100

A.1 Normalized resistance estimates at different load resistances using an injected current of 10 mA at 10 Hz in the q-axis 123

A.2 Normalized resistance estimates at different load resistances using an injected current of 10 mA at 10 Hz in the q-axis 124

B.1 Switching states for CSI modulation in a switching period 126

B.2 Space vector modulation for CSI 126

B.3 Front-end circuit diagram showing H-Bridge, high frequency transformer and rectifier 131

B.4 Switching states of H-Bridge for DC current source front end 131

B.5 Block diagram of DC bus current regulator showing inverter command feedforward 132

List of DSP and MATLAB Codes

B.1 PWM configuration setup 127
B.2 PWM compare value updates 129
B.3 Complex Vector Voltage Regulator 132
B.4 Voltage Observer 133
C.1 Stator Side Field Weakening 134
C.2 Rotor Side Field Weakening 137

Nomenclature

List of key symbols, subscripts and abbreviations are given below.

Symbol	Description
s	Derivative with respect to time: $^{d}/_{dt}$
C	Capacitance
I	Current (peak)
L	Inductance
M	magnetomotive force
Q	Charge
R	Resistance
V	Voltage (peak, line-line)

Subscript	Description
$()_e$	electrical quantity
$()_{fd}$	rotor field quantity
$()_m$	mechanical quantity
$()_{qd}$	complex vector $()_q$ -j$()_d$
$()_r$	rotor quantity
$()_s$	stator quantity

Superscript	Description
$()^*$	Commanded quantity
$()^e$	synchronous reference frame
$()^s$	stationary reference frame
$\hat{()}$	estimated quantity

Abbreviations	Description
CSI	Current Source Inverter
DSP	Digital Signal Processor
CVVR	Complex Vector Voltage Regulator
DS	Dynamic Stiffness
FRF	Frequency Response Function
MCU	Microcontroller Unit
MEMS	Microelectromechanical System
MMF	Magnetomotive Force
PCB	Printed Circuit Board
PI	Proportional Integral
PM	Permanent Magnet
SEM	Synchronous Electrostatic Machine
SVM	Space Vector Modulation
VSI	Voltage Source Inverter

Introduction

Significant efforts are underway on a global scale for improving the efficiency of industrial processes to reduce energy costs and the environmental carbon footprint. The past few decades have witnessed widespread use of electric machines in various industrial and commercial processes. Almost all of these machines harness electromagnetic power conversion to convert electrical energy to mechanical energy. Along with improving the operating efficiency, there is a rising interest in developing sustainable solutions for driving this energy conversion. The introduction summarizes the motivation for investigating electrostatic machines as viable candidates for replacing certain electric machine applications, and provides a background for the need to develop high performance controllers for electrostatic machines.

Motivation

Approximately 45% of the energy produced globally is consumed by electric motor driven applications [7]. This includes applications ranging from industrial processes like manufacturing, material handling and transport to residential applications like HVAC and household appliances. The use of electric motors in commercial and industrial applications is highlighted in Fig. 1[1]. Along with rising demand for electric machines, there is also a need to reduce machine weight, increase power density and reduce the machine

volume. Permanent magnet based electric machines which allow significantly high power densities have found a large scale use in industrial drives for high performance servo systems. However, the driving force behind the increased power densities and high performance lies in the extensive use of materials such as Copper (Cu), magnetic steel and permanent magnets in these machines. The high conductivity and thermal performance makes copper a very attractive material for machine windings. However, there has been considerable financial pressure due to the fluctuating costs of copper in the past decade [8].

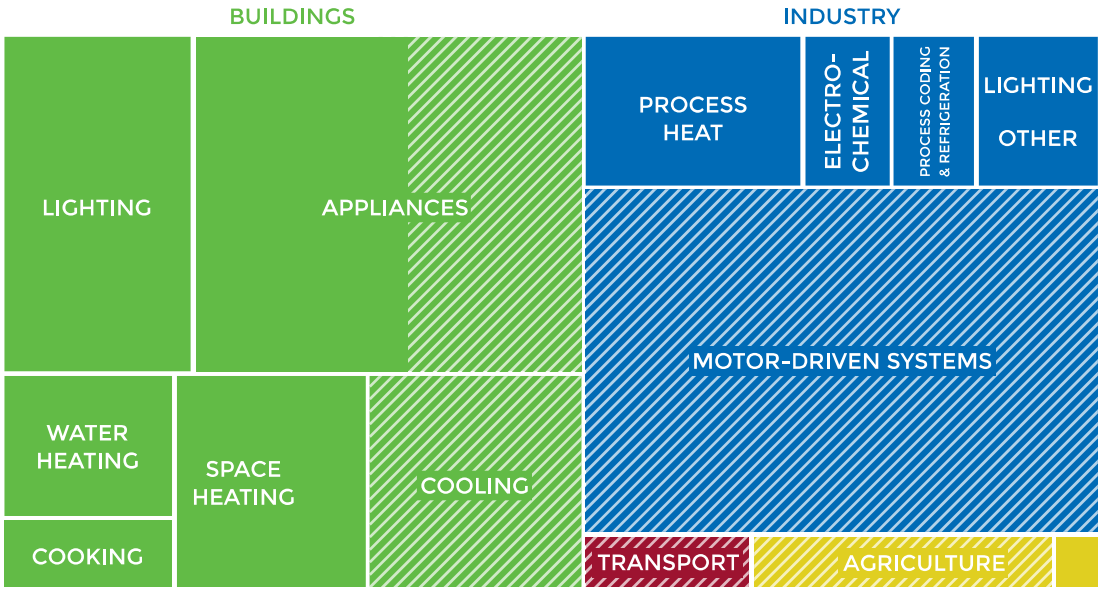

Figure 1, Electricity consumption in commercial and industry applications with shaded portion showing share of electricity consumed by electric motors[1]

Another major material which enables permanent magnet machines are the permanent magnets which mainly consists of materials such as Neodymium (Nd), Boron(B), Dysprosium (Dy), Samarium (Sm) and Cobalt (Co). Among these, there is high uncer-

tainty in the availability of rare-earth materials such as Neodymium, Samarium and Dysprosium. These form the primary materials required for commercial permanent magnets such as NdFeB and Sm-Co. The rise in demand has exerted a stress on the availability of these resources which is reflected in the fluctuating prices [9]. Along with the pricing uncertainty, the extraction of rare-earth minerals has also created growing environmental concerns [10]. There has been an increasing interest in investigating machines with rare-earth free materials [11]. Machines employing rare-earth free magnets as well as reduction of rare-earth magnets in the machine are being investigated.

Electromagnetic machines have been harnessed to power applications requiring speeds from standstill to thousands of rpm. For low speed applications it is usually cost effective and more suitable from a weight-size perspective to use a high speed machine with a mechanical gearbox [12]. Large fans used for ventilation systems are usually run using a gear box. There are various drawbacks of the mechanical gearbox such as maintenance, reliability, additional dynamics, etc. A low speed direct drive can eliminate some of the drawbacks. However, using a PM machine at low speeds might require a high pole count machine or significant over-sizing of the machine to account for copper losses when running at high torque levels.

Many electromagnetic machines rely on shaft mounted fans for cooling [13]. Electromagnetic machines generate rated copper loss at rated torque irrespective of the running speed. Running such machines at standstill requires significant derating or a low duty-cycle operation. This creates difficulty in operations which require full torque over a wide operating range including standstill. Servo drives and robotic actuators are examples of such applications. The machine has to have special cooling or has to be thermally over-designed to be able to withstand the temperature rise due to losses at rated torque at zero speed. In some cases, hydraulic systems are preferred instead of electric actuators to avoid the copper loss for high torque zero speed applications.

Electrostatic machines can be an ideal alternative to address these challenges associated with electromagnetic machines. Electrostatic machines require dielectrics which can be plastics and other non-metallic materials. Rare-earth materials are not required as the machine does not utilize magnetic induction. Since the machine runs on high voltage at low currents, widely available conductors such as aluminum can also be used for manufacture of conducting surfaces.

The performance of an electrostatic machine is especially interesting for zero and low speed applications. It develops torque by charging a capacitor. Theoretically it can hold torque indefinitely without any loss once the capacitive terminal is charged. In practice there is a small leakage current across the capacitor terminals which creates a small amount of conduction loss at standstill. Table 1 shows a comparison of copper loss at holding torque between electromagnetic machines and electrostatic machines. The watt loss per Nm torque developed for an electrostatic machine is significantly lower compared with the loss for the induction and the PM machines. The electrostatic machine design exhibits an optimal torque production for a high pole count [2] the high pole count reduces synchronous mechanical speeds which makes the machine suitable for low speed direct-drive applications.

Use of such an electrostatic machine requires the development of control methods to achieve high bandwidth torque modulation required for servo applications. Along with torque modulation, the machine provides some unique challenges for rotor position measurement due to the significantly high pole count of 96. Investigation of self-sensing methods for electrostatic machines can help eliminate high-resolutions position sensors required due to the high pole count.

Table 1, Comparison of Copper Loss at Holding Torque

Motor Type	Model	Rated Torque	Cu Loss at rated torque at stall	
		[Nm]	[W]	[W/Nm]
PM	bsh1003p11A2A [14]	8	93	11.625
Induction	W22 0.12 kW 10P80 [15]	2.05	56.4 (at 0.5Nm)	112.8
Electrostatic	SEM 1 [2]	7.5	5	0.667

Summary of Chapters

The electrostatic machine exhibits characteristics which makes it an attractive alternative for certain industrial and consumer applications. This thesis investigates the development of a controller platform which includes torque modulation, parameter estimation and self-sensing to enable electrostatic machines to exhibit dynamic performance comparable to electromagnetic machines.

- Chapter 1 outlines a review of the state of the art. Past and present work in the field of electrostatic machine design and control is summarized. Research opportunities are identified.

- Chapter 2 discusses development of a drive system for the SEM. Duality between electromagnetic machines and electrostatic machines is discussed. Power electronics topologies for driving an electrostatic machine are compared.

- Chapter 3 develops a high performance voltage regulator to control the terminal voltages of the SEM. SEM torque modulation is experimentally verified by implementing the proposed voltage regulator on a medium voltage current source inverter based drive.

- Chapter 4 details the development of self-sensing methods for the SEM. Back-mmf based and high frequency injection based methods which when combined can provide estimates over a wide operating range are proposed and experimentally verified.
- Chapter 5 presents key conclusions and contributions offered by this research. Recommended future work in the areas of drive design and controller performance discussed.
- Appendix A discussed the methods used for estimation of machine parameters used for controller in Chapter 3 and Chapter 4.
- Appendix B details the firmware development for the digital controller along with CSI configuration.
- Appendix C presents the simulation computations for the drive limit curves presented in Chapter 2.

CHAPTER 1

A review of the State of the Art

This research investigates the development of a drive system for high performance control of a separately excited electrostatic machine. This chapter presents a summary of past work in the field of electrostatic machine design and operation. A review of control methods and power supply topologies associated with past work in electrostatic machines is summarized. Research opportunities for developing electrostatic machine controls are identified based on the previous work.

1.1 Electrostatic Torque Production

A current carrying conductor placed in a magnetic field experiences mechanical forces which are harnessed to perform mechanical work. The mechanism for energy conversion is *electromagnetic* in nature and the machines developed to harness this mechanism are called *electromagnetic machines*. These are the most common type of machines which find applications in areas ranging from household appliances to industrial manufacturing

processes and traction vehicle applications. Another mechanism of electro-mechanical energy conversion is the force produced when a charge is placed in an electric field. The resulting field is an *electrostatic* force and the machines which employ this mechanism are called *electrostatic machines*. Another way of looking at the two types of torque generation is that electromagnetic torque requires charge in motion while electrostatic torque requires the presence of charge.

One of the first demonstrations of torque production using electrostatic forces was by Benjamin Franklin with the electric carousel in 1748 [16]. This was a simple demonstration of how charges in an electric field can be utilized for producing torque. Since then, electrostatic machines have been embodied in various forms at a range of power and torque levels. Based on the application, the machines range from the MEMS level, low power machines to high voltage, fractional horsepower. The next section discusses the types of rotating electrostatic machines.

1.2 Types of Rotating Electrostatic Machines

1.2.1 Electrostatic Induction Machines

An electrostatic induction machine relies on a traveling potential wave inducing a charge on a rotor plate which lags behind the potential wave. This machine has been investigated by [3] ,[17] and [18]. The machine does not require position feedback or closed loop operation for applications not requiring a high dynamic performance. The rotor dielectric constant and conductivity influence machine torque production. Equation 1.1 shows the torque produced by an electrostatic induction machine [2] where C_m is the stator-rotor mutual capacitance and G represents the machine conductance. The machine slip is given by s. Fig. 1.1 shows a radial electrostatic induction machine with A,B and C denoting

the phases of a three-phase stator.

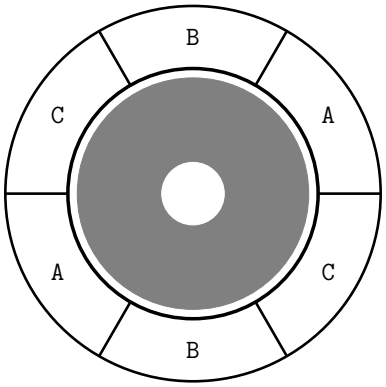

Figure 1.1, Electrostatic Induction machine

$$T_{ind} = \frac{3P}{2}|V_s|^2 \frac{s\omega_e C_m (C_m G_r - C_r G_m)}{G_r^2 + s^2 \omega_e^2 C_r^2} \tag{1.1}$$

1.2.2 Variable Elastance Machines

This type of machine is a dual of a variable reluctance machine. The machine is designed to have a spatially varying capacitance. The machine is then driven with square wave voltages. The torque produced by the machine is proportional to the square of the voltage and the capacitance variation as seen in (1.2). Figure Fig. 1.2 shows a variable elastance machine where A,B,C and D denote the stator phases. The design of the rotor creates a variable capacitance.

$$T_e \propto V^2 \frac{dC}{d\theta} \tag{1.2}$$

Different aspects of machine design for controlling the characteristics of such a machine were investigated by [19],[15],[20] and [21].

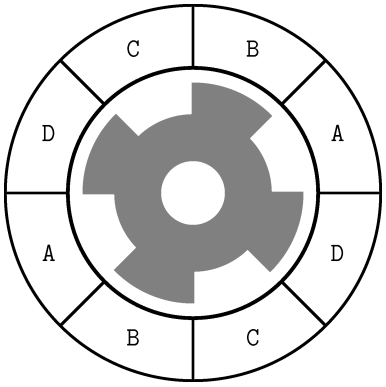

Figure 1.2, Variable elastance machine

1.2.3 Separately Excited Synchronous Electrostatic Machines

A separately excited synchronous electrostatic machine has an external DC rotor excitation. Fig. 1.3 shows a radial flux type, separately excited electrostatic machine where A,B and C show the stator phases and P and N shows the poles of the rotor excitation. Equation (1.3) shows the torque generated by the machine which includes the saliency and field torque components. A salient machine will be able to produce field torque and saliency torque. A non-salient machine on the other hand will be able to generate only field torque. The field can be excited by multiple methods such as slip rings or brushes or wireless power transfer.

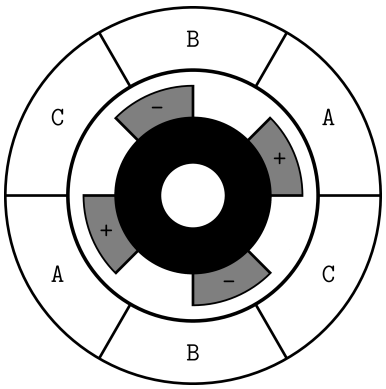

Figure 1.3, Separately excited synchronous machine

$$T_e = \frac{3P}{2}[(C_{ds} - C_{qs})V_{qs}^e V_{ds}^e - C_{md}V_{fd}V_{qs}^e] \tag{1.3}$$

1.3 Electrostatic Machine Design

1.3.1 MEMS Scale

Electrostatic machines have become popular at the MEMS scale mainly due to the relative ease of manufacturing and higher power density compared to their electromagnetic counterparts at a micro scale [18], [22]. These machines operate at the micro to milliwatt power level.

Utilization of electrostatic forces for high speed applications has been explored at the MEMS scale by S. F. Nagle et al.[23],[3]. The machine, of the electrostatic induction type was manufactured on a silicon wafer substrate. The machine was designed for high speeds up to 300,000 rpm. The machine runs at 90V and requires excitation frequencies up to a megahertz. The machine is capable of delivering 5.8 mW of power at a maximum torque of 2μNm. It has been pointed out that the performance of this machine was limited due to mechanical strength of the tethers holding the rotor and not the electric breakdown. The actual voltage breakdown capability of the machine would make the micromotor comparable to performance achieved by electromagnetic machines in the macro scale.

Fan et al. [24] investigated the development of variable capacitance type micro-actuators manufactured using integrated circuit manufacturing processes.

The work by B. Bollée [25] investigated the comparison between electrostatic machines and electromagnetic machines under similar operating conditions. It was observed that the performance of electrostatic machines is primarily limited due to the low voltage

breakdown strength which can be improved by using vacuum environments. The study investigated multiple embodiments of high pole count synchronous (varying capacitance) as well as asynchronous electrostatic machines. Synchronous machines of a very small size were found to have torque generation capacity of a practical interest to power applications such as clock mechanisms.

The work in [26] investigated the development of electrostatic induction type machines for mechatronics application and were able to achieve a 0.2N thrust force with a film type actuator.

1.3.2 Macro-scale

At the macro-scale, one of the first demonstrations of electrostatic machines was a variable capacitance synchronous electrostatic machine developed in 1933 by J.G. Trump [27]. A vacuum was employed to boost the breakdown strength of the machine which would allow higher power operation. The machine had a two-pole design with a synchronous speed of 3600 rpm at 60 Hz excitation frequency. The machine could be operated both, as a motor and as a generator. The machine test setup included a separate assembly which could bring it up to synchronous speed. The machine demonstrated a 55W output power with a 73kV excitation. The experiment demonstrated a machine efficiency better than 99 %. The development of the vacuum electrostatic machine was to illustrate the simplicity of electrostatic design compared with the electromagnetic machines. The work also includes ten different electrostatic machine designs which range from AC to DC type and operating as motors and generators.

Another investigation of improving the power density of electrostatic machines by N. J. Felici is described in [28], where high pressure gases were used for improving the breakdown strength. An axial flux type variable capacitance machine capable of generating

750 W of power at 250 kV was developed as a part of this study.

Shinsei Corporation developed a peg-style DC electrostatic machine, capable of delivering 100 W power running at 10,000 rpm with a 0.1 Nm torque [29]. The voltage breakdown strength was enhanced substantially by running the machine in a vacuum environment which enabled terminal voltages up to 100 kV Both the stator and rotor were excited to produce torque. The machine ran at 95% efficiency.

T. Niino et al. developed one of the first electrostatic machines to use a dual excitation [30]. The work described a multi-phase, higher power linear machine where both the stator and the rotor were excited to generate a high torque. The single slider generated 1.6 W power with a thrust force of 4.4 N. A second prototype manufactured using 50 layers of the linear machine was able to demonstrate a 310 N thrust force. The torque could be increased by using multiple stator and rotor layers. A similar technique was investigated for rotary machines. However, the generated torque was found to be highly influenced by mechanical design. The machine generated a maximum power of 36 mW and a maximum torque of 0.69 mNm. A machine design based on a similar design was investigated as a potential candidate for operation near a magnetic resonance imaging (MRI) environment.

A fluid filled, 3D-printed variable-elastance type electrostatic machine was presented in [31]. The machine demonstrated a torque density of 0.22 Nm/Kg which is comparable to induction machines of a similar size. The machine has a rated voltage of 7 kV to generate a 1.5 Nm torque. The 3D printed machine experimentally demonstrated the possibility of using additive manufacturing for development of electrostatic actuators. The 3D-printing is utilized to optimize the surface area for torque production and a fluid is filled in the machine to increase the dielectric strength and further increase the voltage breakdown strength.

1.3.3 Separately Excited Synchronous Electrostatic Machine at UW-Madison

The main limitation of electrostatic machines when compared with the electromagnetic machine is the approximately five orders of lower energy density in found in electrostatic machines [19]. Improvements in multiple aspects of torque production in the past five years resulted in the development of a high torque density, fractional horsepower-scale, separately excited synchronous electrostatic machine [2],[32]. The various improvements in the process of machine design to achieve the high torque density include [32]:

- Utilizing a dielectric liquid to allow high electric shear stress [33]: The dielectric liquid allows a higher voltage breakdown strength and also increases the dielectric constant for increasing capacitance.
- Improving contact surface area [19], [34],[35]: Methods such as 3-D printing based manufacturing and PCB based machine design are used for increasing the surface area.
- Electrode optimization [15]: The shape of the electrode is modified for optimal performance.
- Manufacturing improvements [15] and [21].
- Separate Excitation [31],[2]: A separate excitation is applied on the rotor for increasing torque generation.

This type of separately excited electrostatic machine will be referred to as SEM for the rest of the thesis.

Table 1.1 summarizes specifications for different types of electrostatic machines [2].

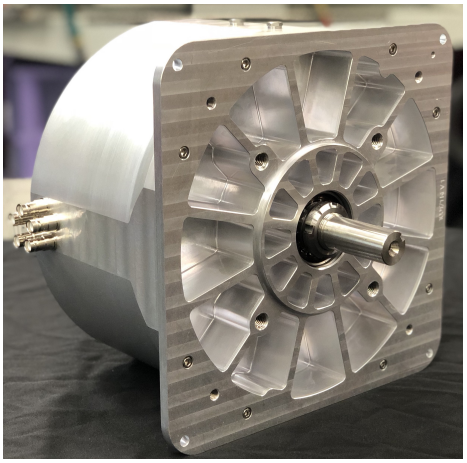

Figure 1.4, Front view of SEM1 [2]

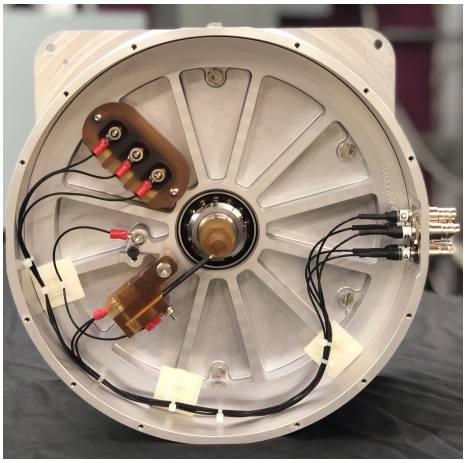

Figure 1.5, Back view of SEM1 [2]

Table 1.1, Comparison of performance metrics of different types of electrostatic machines

	Power	Torque	Speed	Voltage	Type*
	W	Nm	rpm	kV	
J.G. Trump [27]	5.5E+1	1.5E-1	3.6E+3	7.3E+1	Sync
N. J. Felici [28]	5.0E+2	6.4E0	7.5E+2	2.5E+2	Sync
B. Bollée [25]	2.0E-4	3.2E-6	6.0E+2	2.2E-1	Ind
B. Bollée [25]	1.0E-4	4.8E-6	2.0E+2	2.2E-1	Sync
S.F. Bart [18]	7.9E-7	7.5E-10	1.0E+4	1.0E-1	Ind
T. Niino [30]	3.6E-3	6.9E-4	2.0E+2	1.8E0	S, Sync
S. F. Nagle [3]	5.8E-2	2.0E-6	2.7E+5	9.0E-2	Ind
Shinsei Corp. [29]	1.0E+2	1.0E-1	1.0E+4	1.0E+2	DC
B. Ge [31]	2.0E+1	1.2E0	5.0E+2	7.0E0	Sync
B. Ge [21]	3.0E+1	2.0E0	5.0E+2	9.0E0	Sync
B. Ge [2]	1.0E+3	8.0E0	1.2E+3	8.0E0	S, Sync

*Ind - Induction Machine , Sync - Synchronous Machine, DC- DC Machine

S - Separately Excited.

1.4 Electrostatic Machine Torque Modulation

This section summarizes approaches that have been utilized to control the aforementioned electrostatic machines.

An electronic op-amp based drive, as shown in figure 1.6 was employed for testing the induction machine developed by Nagle et al. [3]. The drive relies on a frequency command signal which generates the required stator frequency output for the machine. There is no closed-loop control over the rotor speed or torque. Figure 1.7 shows the torque speed curve of the MEMS electrostatic machine [3].

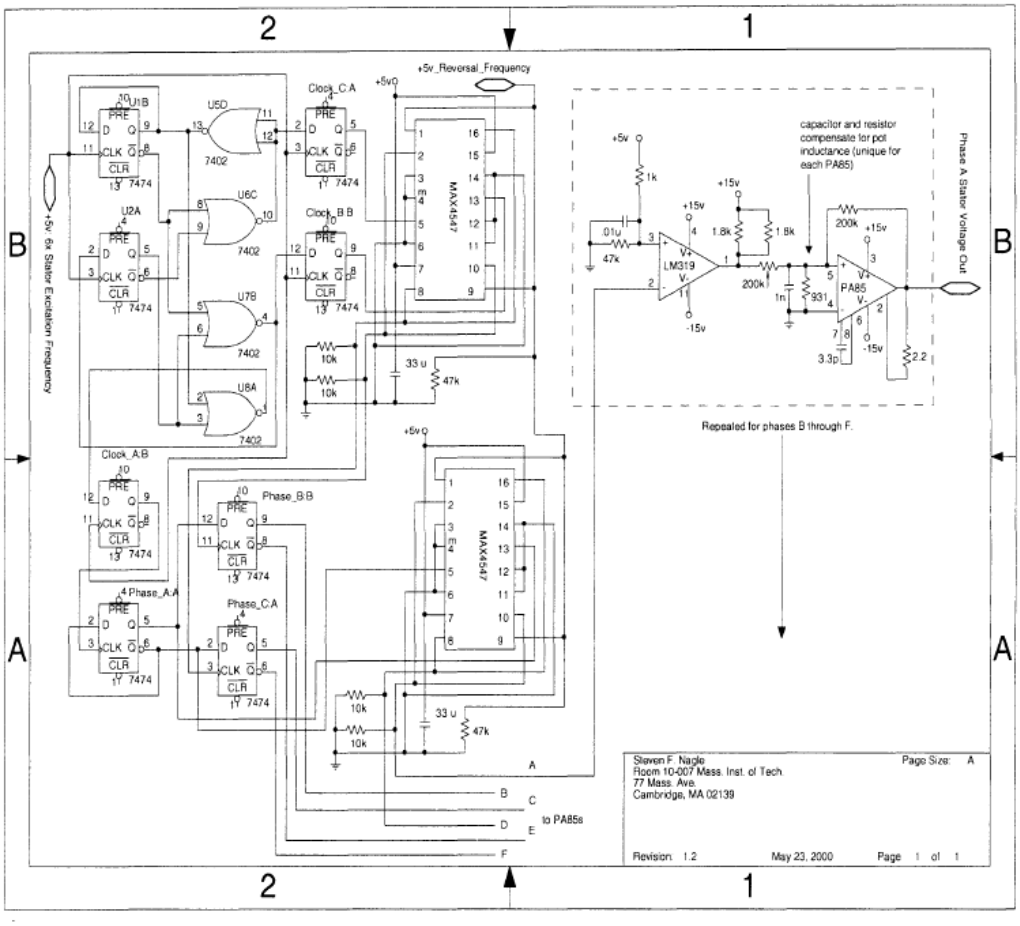

Figure 1.6, Opamp based drive system for electrostatic induction micromotor[3]

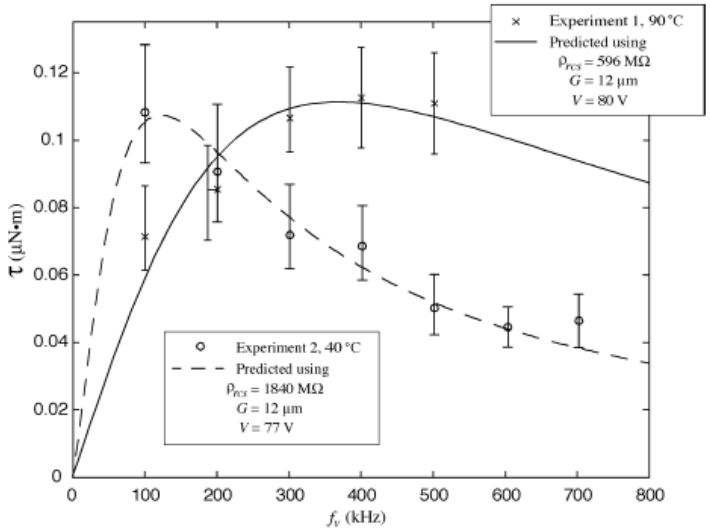

Figure 1.7, Torque Vs Speed for an Electrostatic Induction Machine[3]

Another approach for the same induction-type machine was investigated by T. C. Neugebauer et al. in [36]. This work was mainly directed at developing a drive capable of operating at frequencies up to 2 MHz and voltages up to 300 V. A multilevel, multi-phase topology was chosen to power the machine with a voltage of 150 V at 280 kHz. The machine was run in an open loop mode with speed controlled by changing the excitation frequency. The research identified that the power electronics required for the driving the machine was orders of magnitude larger than the machine itself. The magnetics for the inverter proved to be a limiting factor if operation over a wide range was desired.

The high voltage variable capacitance electrostatic machine developed by J. G. Trump was brought up to synchronous speed using a separate motor assembly [27]. The machine was connected to the grid using high-voltage transformers. The system was capable of running in the motoring and generating modes. However, there was no closed-loop control over the machine torque.

Work presented by B. Bollée [25] discusses starting mechanisms for synchronous

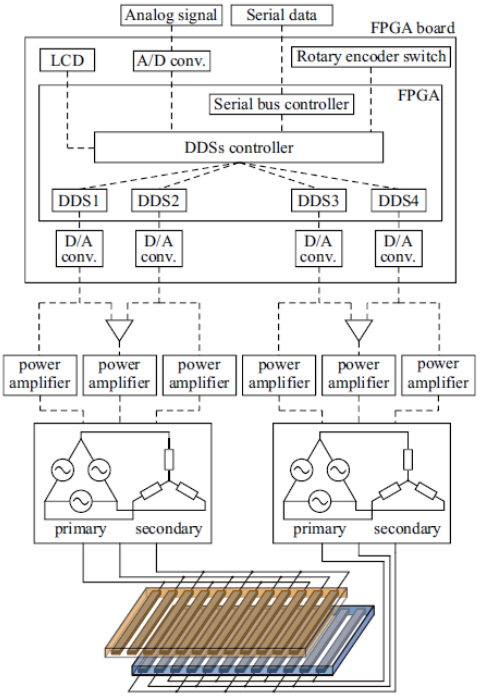

Figure 1.8, Motor drive circuit[4]

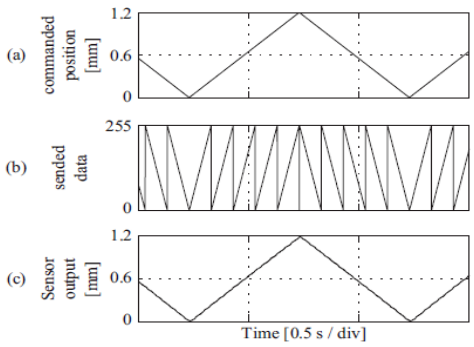

Fig. 11. The electrostatic motor film

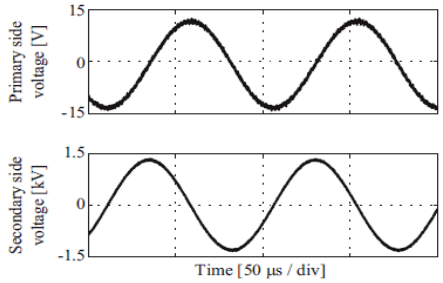

Figure 1.9, Motor operation plots[4]

machines in detail. The machine was controlled in open loop and relied on the torque generated, initial position and rotor inertia to achieve an successful start condition.

A drive system was developed for the dual excitation motor [30] by F. Kimura et al.[4]. A field programmable gate array (FPGA) based system was developed to generate command signals to the drive which consisted of step-up transformers to control the position of the linear machine. Figures 1.8 and 1.9 show the FPGA based drive design and the control plots for the machine [4].

Table 1.2 summarizes the control methods used for electrostatic machine control in previous work.

Table 1.2, Summary of machine control methods used by prior researchers.

	Type*	Power Source	Control Method	Position Feedback
J.G. Trump [27]	Sync	HV Transformer	**Open Loop**	N
N. J. Felici [28]	Sync	Run as generator	**Open Loop**	N
B. Bollée [25]	Sync	square wave voltage	**Open Loop**	N
B. Bollée [25]	Ind	220V, 50Hz	**Open Loop**	N
T. Niino [30]	S, Sync	Commercial Supply	**Open Loop**	Y
S. F. Nagle [3]	Sync	Linear Amp	**Open Loop**	N
Shinsei [29]	DC	Amp	**Open Loop**	Y
B. Ge [31]	Sync	Linear Amp	**Open Loop**	Y
B. Ge [21]	Sync	Linear Amp	**Open Loop**	Y
B. Ge [32],[2]	S, Sync	Linear Amp	**Open Loop**	Y

*Ind - Induction Machine , Sync - Synchronous Machine, DC- DC Machine

S - Separately Excited.

1.5 Chapter Summary and Research Opportunities

This chapter summarizes different types of electrostatic machines along with methods used for testing the machines. It can be seen from the review of the current and past work in the field of electrostatic machines that **there is no conventional off-the-shelf drive or control methodology available for regulating the electrostatic machine torque** . Previous studies in electrostatic machines have been limited to machine design and optimization. It is also seen that **majority of the work associated with developing power supplies for the machine has been for testing machine performance rather**

than achieving torque modulation. Research opportunities to investigate various aspects of drive design are summarized as follows.

1.5.1 Electrostatic Machine Drive Requirements

- A drive systems needs to be developed for achieving closed-loop torque modulation of electrostatic machines.
- A thorough analysis of the machine dynamics and power requirements is necessary to be able to determine a drive system design and subsequently implement a closed loop control algorithm.
- A control methodology that can modulate torque over a wide operating region including zero speed needs to be developed.

1.5.2 Duality

- The duality between electrostatic machines and electromagnetic machines has been well established for machine design [2]. This duality can be further analyzed to provide an approach in developing a drive system for the electrostatic machine.
- The performance improvements that have been developed for electromagnetic systems need to be evaluated for use in electrostatic machines in their dual form.

1.5.3 Power Electronics

- Different power electronic topologies need to be investigated based on machine requirements for powering the machine.
- Control methods for the different topologies need to be identified.

1.5.4 Voltage Control

- A voltage regulator for a CSI needs to be developed.
- This presents an opportunity to develop a high bandwidth voltage regulator taking SEM dynamics into consideration.

1.5.5 Rotor Position Self-Sensing

- The requirement for a position sensor for operating the machines shown in Table 1.2 indicates an opportunity for self-sensing.
- Elimination of position sensors by implementation of self-sensing methods can aid in reducing the cost, weight and volume footprint of the SEM.

CHAPTER 2

Drive Development for Electrostatic Machines

It was seen from the review of the state of art in Chapter 1 that no off-the-shelf drive solution exists for an SEM. This chapter focuses on design consideration for developing a drive solution for the electrostatic machine. The duality between electromagnetic and electrostatic systems is investigated for identifying possible solutions. Power electronics topologies are investigated to identify viable candidates for the inverter design.

2.1 Duality between Electrostatic and Electromagnetic Machine Dynamics

The duality between series RL and parallel RC circuits has been well established. This duality has been explored in depth in [31] for the purpose of torque production. The inductance(L) and the capacitance(C) are material property dependent parameters for electromagnetic and electrostatic systems respectively. The energy storage capability of these systems is a function of the physical parameters along with the energy source

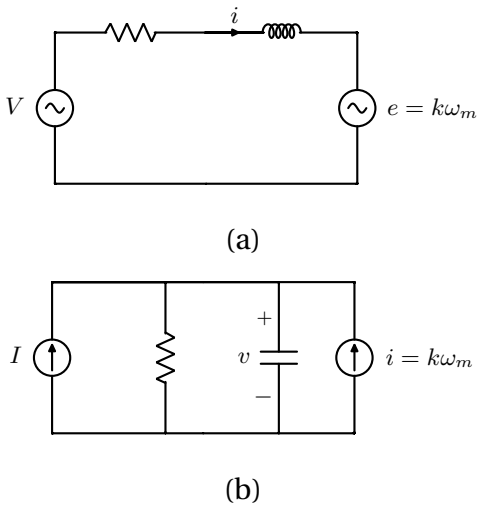

Figure 2.1, Circuit model for a) Electromagnetic machine, b) Electrostatic machine.

(current for electromagnetic) and (voltage for electrostatic). The dynamics of these systems are governed by the ability to modulate the energy source for a given value of the physical parameters. Figure 2.1 shows the block diagrams for electromagnetic and electrostatic machines. The electromagnetic machine model includes a series resistance and inductance which is dependent on the machine winding and the material used for the machine. The electro-mechanical coupling for this machine is a rotational velocity dependent back-emf. For the capacitive machine, the model includes a parallel resistance and capacitance which depend on the machine materials and construction. The electro-mechanical coupling in this case is a back-current generated due to the rotating rotor charge.

The dual nature of these systems can be extended to control mechanism. The dynamics of the dual systems can be controlled as:

- An electromagnetic machine can controlled by controlling the current flowing through an inductor.
- An electrostatic machine can be controlled by controlling the voltage across the

capacitor terminal.

The series resistance and the parallel resistance provide a source of damping (alternatively seen as machine loss) for the electromagnetic and electrostatic systems.

It can be seen from the RL and RC circuit diagrams that the two systems have very similar dynamics based on the physical parameters. The RL circuit has a time constant given by $^{L}/_{R}$ and the RC circuit has a time constant of RC.

The current flowing through the RL circuit in the electromagnetic machine can be controlled by controlling flux or voltage-seconds supplied to the machine. Similarly the terminal voltage of the electrostatic machine can be controlled by controlling the charge or ampere-seconds supplied to the capacitor. This gives an insight into the ideal drive topologies for electromagnetic and electrostatic machines. The ideal power source topologies for two types of machines can be identified as:

- A voltage source is used to control the current in an RL circuit.
- A current source is used to control the output terminal voltage of an RC circuit.

2.1.1 Current Source Inverter for Electrostatic Machine Control

The torque generated by an electrostatic machine is proportional to the terminal voltage of the machine. This can imply that an output voltage controlled power supply can be used directly for controlling an electrostatic machine. This is true for basic testing of the machine. Consistent with this, it can be seen that all the previous demonstrations of electrostatic machines fundamentally used voltage sources for testing the machine. The voltage source serves as an attractive approach for testing the low voltage high frequency MEMs scale machines where the output voltages can be easily synthesized by electronic devices. For small time-constants, the voltage supply can have very fast dynamics so

that it does not affect machine operation. A voltage source would be sufficient to run a machine in open loop applications. Voltage supplies can be broadly classified into two categories:

2.1.1.1 Linear Supplies

Linear power supplies can be used for synthesizing high bandwidth voltage signals. Linear supplies use the linear reagion of the I-V curve of a transistor for amplification. Linear supplies can also be used to achieve the high voltages required for some of the electrostatic machines. However one major drawback of using linear supplies is the reduced efficiency. This would limit the use of linear voltage supplies to applications where power supply efficiency is not a major concern.

2.1.1.2 Switched Supplies

Both voltage source and current source inverters can be used for realizing a voltage supply. A voltage source cannot be directly connected to an electrostatic machine due to the large switching currents arising out of the capacitive load. An inductor is required to limit inrush and ripple current. However, addition of the inductor creates an LC resonance, which can cause undesirable dynamic response. The current source, on the other hand, can be connected to a capacitive load directly to control the voltage. Considerations of the dynamic response along with the higher efficiency exhibited by switched power supplies at the macro-scale implies that a CSI will be the ideal drive type for electrostatic machines.

Electrostatic and electromagnetic duality can also be another path of determining the drive type. An electromagnetic machine's output torque is dynamically controlled by controlling the flux (volt-seconds) which eventually controls the machine current.

Similarly, a CSI can be used to control the charge (ampere-seconds) sourced by the drive to control its terminal voltage which generates mechanical torque.

2.2 Charge Oriented Control

Figure 2.2 shows the phasor diagram for a salient pole synchronous electrostatic machine in the steady state. This is similar to the phasor diagram for a separately excited synchronous magnetic motor. The rotor induced back-MMF (a back-current) vector M is orthogonal to the rotor charge vector Q_{dr}. The rotor charge is aligned with the d-axis. This orientation with the rotor charge allows independent control of the electric field and torque. With the rotor charge oriented with the d-axis, the machine torque can be controlled by controlling the q-axis voltage. The phasor diagram in Fig. 2.2 depicts the machine in a motoring mode. A negative q-axis voltage is shown due to the fact that the machine generates a positive torque for a negative q-axis voltage as shown in the machine torque equation (2.3).

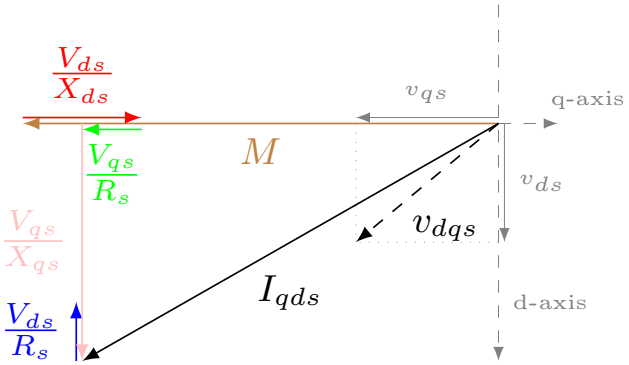

Figure 2.2, Phasor diagram for a salient pole synchronous electrostatic machine

2.3 Power Electronics for Electrostatic Drive

Figure 2.3 shows the system block diagram for a drive for an electrostatic machine. A voltage command is computed from the electro-mechanical equation of the SEM with the rotor charge oriented with the d-axis. A voltage regulator will generate the required current command by comparing the voltage command to the feedback voltage signals from the machine. The voltage regulator design is elaborated in Chapter 3. The current command is fed to a suitable current excitation which then provides the necessary ampere seconds to drive the machine. To implement charge-oriented control, the position of the rotor is necessary. A mechanical encoder or a position estimation algorithm can be used for position feedback.

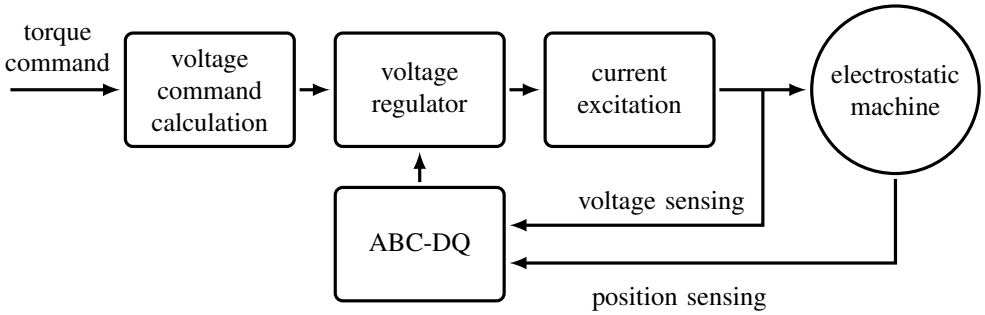

Figure 2.3, Voltage regulator block diagram

The drive requires a current excitation for powering the machine. Different topologies which can be used for the current excitation are summarized in the next section along with application specific advantages and challenges.

2.3.1 High voltage CSI

A current source inverter is the ideal drive topology for the electrostatic machine. The CSI sources ampere-seconds which can be modulated to regulate the voltage on the machine terminals. Figure 2.4 shows the model of a current source inverter with an

electrostatic machine. The DC supply in this topology is a current source with an inductor. The switches for the CSI need to have a high voltage blocking capacity to be able to generate medium voltage levels for the SEM. The inverter can be operated in six-step mode for an ampere-per-hertz operation or in PWM mode for voltage regulated operation. A CSI driven control topology would need the voltage feedback for controlling the ampere seconds sourced to the capacitor terminals. This requires a very simple control structure without the need to measure machine currents. The control topology shown in the block diagram in Fig. 2.3 can be implemented with a CSI for controlling the SEM.

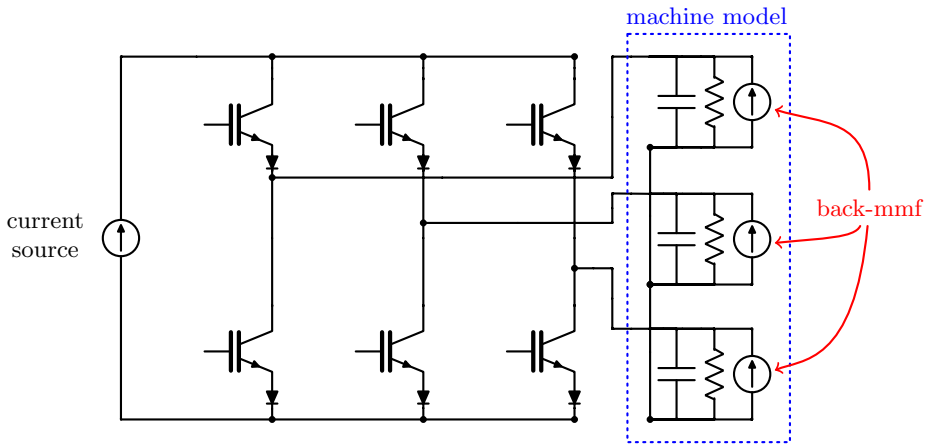

Figure 2.4, CSI with an electrostatic machine model

The advantages of using a CSI topology for the SEM are:

- Direct connection to a CSI which requires a capacitor on the output: The SEM exhibits capacitive terminal properties which are the ideal terminal properties for a CSI.

- The AC system has a single-order response which makes developing a controller simple: Neglecting system parasitics, the CSI-SEM system exhibits single-order dynamics which allows a simple control structure to be utilized for control.

- The inverter has the ability to generate low frequency and DC voltages which is essential for low speed and holding torque operation of the SEM.

The major drawbacks associated with this topology lie in the device availability and device ratings which are addressed in Section 2.4 in this chapter.

2.3.2 High voltage VSI

The current source drive that is necessary for the electrostatic machine can also be achieved using a stiff current source generated by a voltage source drive. This is done by placing inductors at the output of a VSI. A voltage loop is implemented to provide voltage control for the drive. This topology will also need high voltage inductors and switches. Figure 2.5 shows a model of a high voltage VSI with output inductors connected to the SEM.

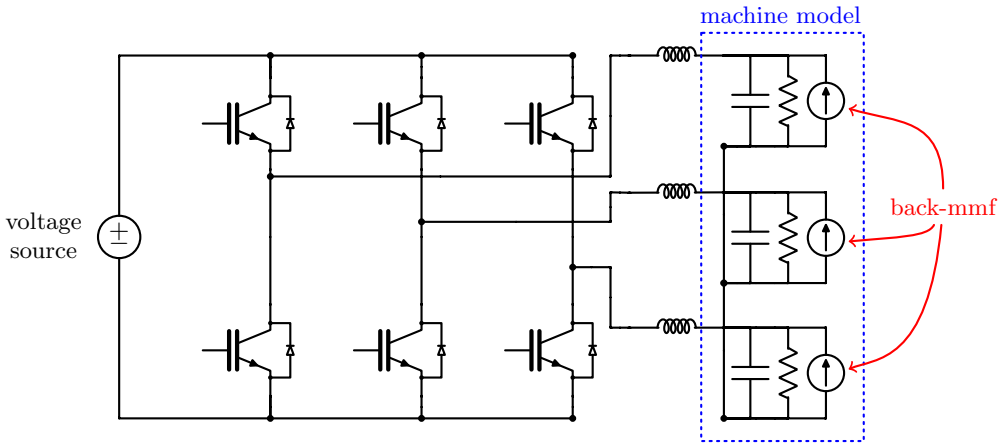

Figure 2.5, VSI with an electrostatic machine model

The advantages of this topology are:

- Relatively simple dynamics which aid in implementing a simple control structure.

- The inverter has the ability to generate low frequency and DC voltages for supporting low speed and holding torque operation.

The challenges associated with this topology are:

- Management of inductor current dynamics.
- Requirement of high voltage inductors and devices.
- The output inductors and the machine capacitance creates an LC resonance which can add undesirable dynamics if not considered during system design.

The controller topology for this drive is shown in Fig. 2.6. An inner current loop can be implemented with the VSI for enhancing controller performance.

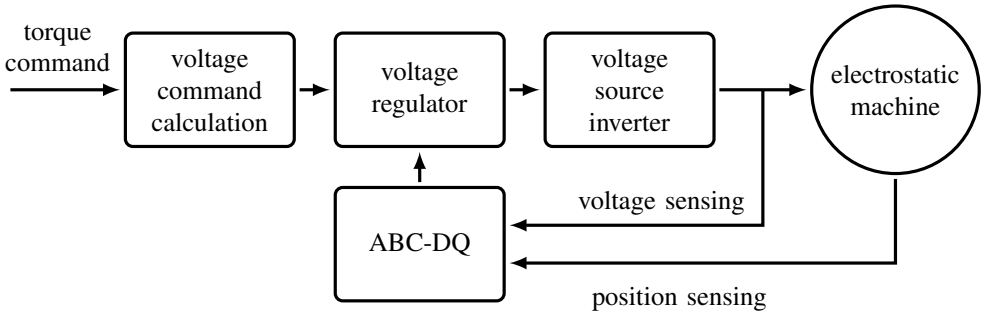

Figure 2.6, Block diagram for control of SEM using a high voltage VSI

2.3.3 Low voltage VSI with Step-up Transformers

Another alternative for the drive is to utilize high voltage step-up transformers. The current in the primary of the transformer can be controlled with the VSI to control the voltage across the output of the transformer. The advantage of this topology is that the system can utilize off-the-shelf power electronics with the step-up transformer. A voltage loop is required for controlling the voltage at the output of the transformers. The main

limitation of this method is that it cannot be used for zero speed control of the machine. The transformer design will limit the low frequency operation of this topology. However, for high speed constant speed applications such as direct drive fan loads, the transformer size is reduced due to the high frequency. The low voltage inverter topology can be an attractive alternative to use of high voltage blocking devices due to drive complexity and cost.

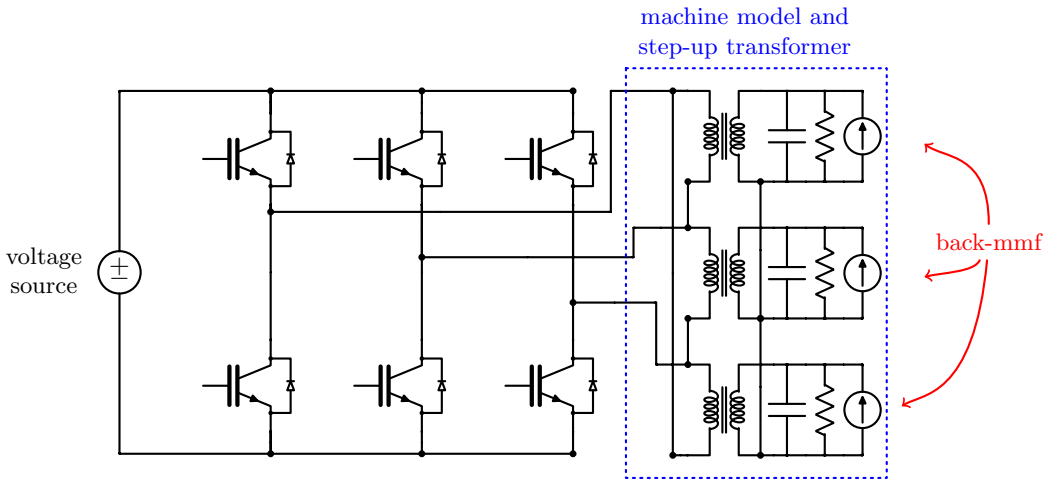

Figure 2.7, Low voltage VSI with step up transformers and an electrostatic machine model

The key benefits of this topology are:

- The use of low voltage off-the-shelf drive.
- Attractive for constant speed applications.
- Lower design complications in the inverter due to low voltage.

The major drawbacks of this topology are:

- Operation at stand still is not achievable.
- Low speed operation is limited by transformer design.

- Complicated dynamic response due to the addition of transformers.
- Non-linear behavior of transformers.

The controller topology for this drive is shown in Fig. 2.8. The VSI with the step-up transformer system needs a current loop to control transformer current. A voltage loop can be implemented outside the current loop to control the machine terminal voltage. The transformer model needs to be studied properly for transformer non-linearities such as saturation. The transformer frequency response limits the performance of the drive.

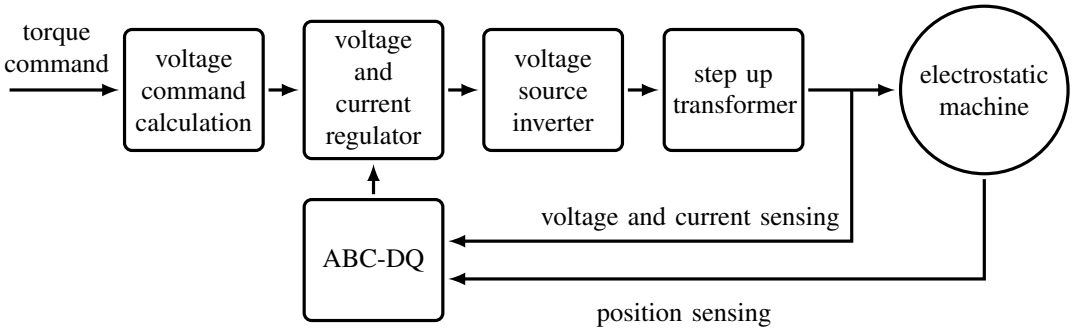

Figure 2.8, Block diagram for control of SEM using a low voltage VSI with step-up transformers

Table 2.1 gives a summary of comparison between the advantages and challenges associated with the different drive topologies for controlling an electrostatic machine.

2.4 Power Electronic Device Considerations for Electrostatic Drives

The comparison of drive topologies discussed in Section 2.3 identifies the medium-voltage CSI or the medium-voltage VSI type drive topology to drive position and hold type loads. Both these drive topologies need devices capable of handling medium voltages. Commercial medium voltage drives typically operate in the megawatt power level [37].

Table 2.1, Comparison of medium voltage drive topologies

	MV CSI	**MV VSI with Inductor**	**LV VSI with step-up transformer**
Devices	High Voltage	High Voltage	Low Voltage
Dynamics	Simple (Approx First order)	Relatively Simple (Approx Second Order)	Complex
Control	Easy	Easy	Complicated
Zero Speed Operation	Achievable	Achievable	Not Achievable
Passive Component Dynamics	Simple	Medium	Complex

The SEM however requires very low currents in the range of a fraction of an ampere. Figure 2.9 shows the distribution of ratings for power devices available on digikey[5]. Majority of the MOSFET and IGBT devices are concentrated in the 1 kV - 2 kV levels and high current levels. Only SCRs posses the capability to block the 7kV required for the drive. However, the SCRs are rated at a higher current with limited switch frequency which would limit drive performance. This makes the drive design for the SEM challenging and only the low voltage VSI with step-transformers can be realized without the need of high voltage blocking switches.

Additional considerations while designing a drive topology for the SEM are discussed in detail in [5].

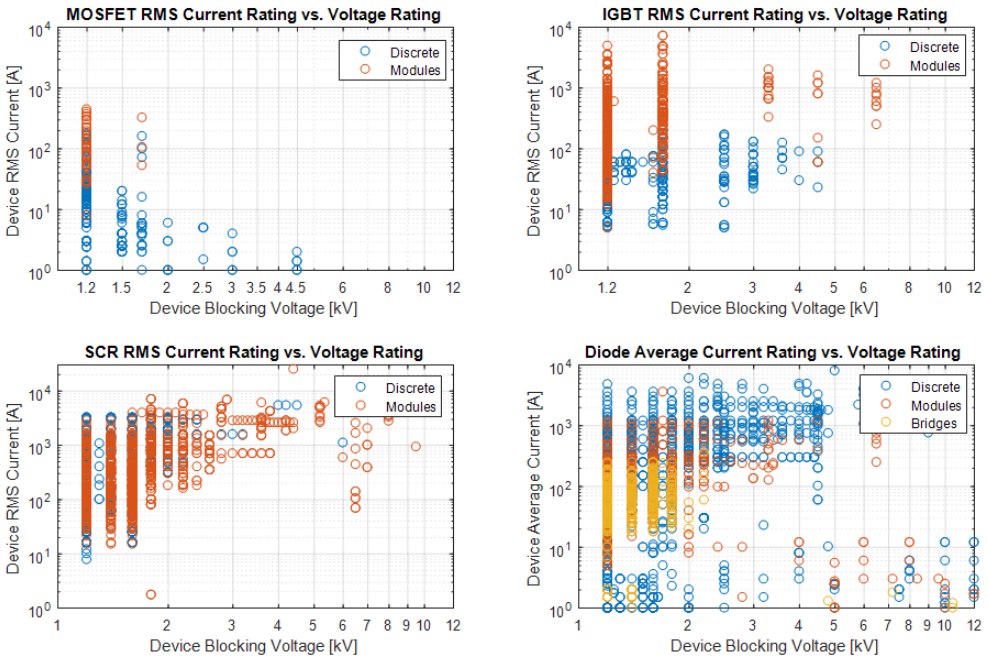

Figure 2.9, Semiconductor device ratings from Digikey [5]

2.5 Steady State Drive Limit Curves

2.5.1 Stator side field weakening

A general idea of the drive ratings and performance can be obtained from the machine steady state performance curves. The DC bus current and voltage breakdown rating of the machine are used as limits for the drive performance. The leakage resistance of the machine is assumed to be negligible for the purpose of the steady state performance at high speeds. Equations (2.1), (2.2) and (2.3) give the relation of the current of the machine and the mechanical torque. The current flowing in the leakage resistance is neglected.

$$I^e_{qs} = w_e C_s V^e_{ds} - w_e C_{md} V_{fd} \tag{2.1}$$

$$I^e_{ds} = -w_e C_s V^e_{qs} \tag{2.2}$$

$$T_e = -{}^3/_2 P C_{md} V_{qs}^e V_{fd} \tag{2.3}$$

The maximum voltage that the machine can handle is the breakdown strength of the machine. The equation for the maximum dq-axis voltage of the machine for a breakdown voltage limit of V_{lim} is seen in (2.4). The DC link current limits the maximum current that can be sourced to the machine. The equation for the current limit for a DC link current I_{bus} is given by (2.6). The dq-axis voltages can be depicted by the torque angle of the machine γ as seen in (2.5).

$$\sqrt{(V_{qs}^e)^2 + (V_{qs}^e)^2} \leq V_{lim} \tag{2.4}$$

$$V_{qs} = V cos(\gamma), V_{ds} = -V sin(\gamma) \tag{2.5}$$

$$\sqrt{(I_{qs}^e)^2 + (I_{ds}^e)^2} \leq I_{bus} \tag{2.6}$$

The maximum torque-per-volt condition for the SEM is achieved by a q-axis voltage ($\gamma = 0$) due to the negligible saliency. The maximum speed ω_{e-max} that can be achieved using a bus current I_{bus} can be obtained by substituting (2.1) and (2.2) in (2.6) with $\gamma = 0$. Beyond this speed given by (2.7), the torque angle of the machine γ can be increased to weaken the machine field which reduces the back-mmf. In this condition the inverter voltage and current limit is satisfied and the angle can be calculated by substituting (2.1) and (2.2) in (2.6) and solving for γ. The angle for weakening the field is given by (2.8).

$$\omega_{e-max} = \frac{I_{bus}}{\sqrt{(C_{md} V_{fd})^2 + (C_s V_{lim}^e)^2}} \tag{2.7}$$

The torque angle for the inverter above the max speed ω_{e-max} is given by (2.8).

$$sin(\gamma) = -\frac{I_{bus}^2 - \omega_e^2 C_s^2 V_{lim}^2 - \omega_e^2 C_{md}^2 V_{fd}^2}{2\omega_e C_{md} C_s V_{fd} V_{lim}} \tag{2.8}$$

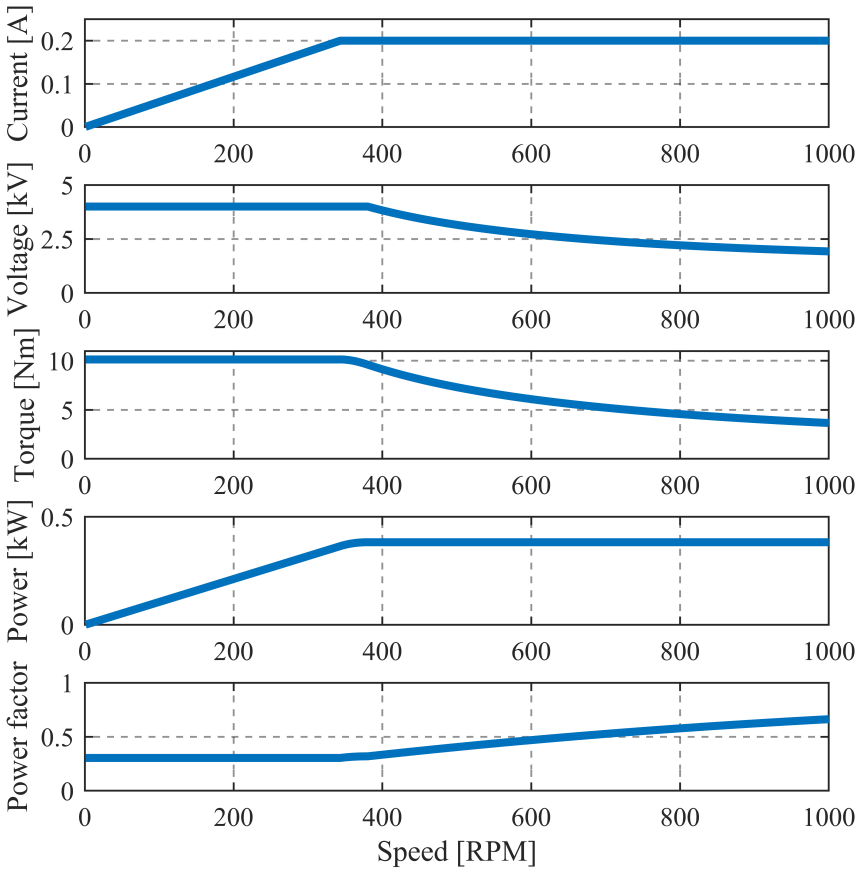

Figure 2.10, Machine currents, voltages,torque, power and power factor limit curves with field weakening at $I_{bus} = 200mA$, $V_{lim} = 4000V$ and $V_{fd} = -8000V$

The maximum speed of the machine is determined by the maximum back-mmf that can be canceled by the field weakening. The maximum field that the machine can cancel is determined by equating (2.10) to zero. If the maximum possible field weakening at $\gamma = 90$ is the exact voltage to cancel the back-mmf, we get (2.9). If $V_{lim}C_s < V_{fd}C_{md}$, then the machine speed will be limited to this point as the torque at $\gamma = 90$ will be zero.

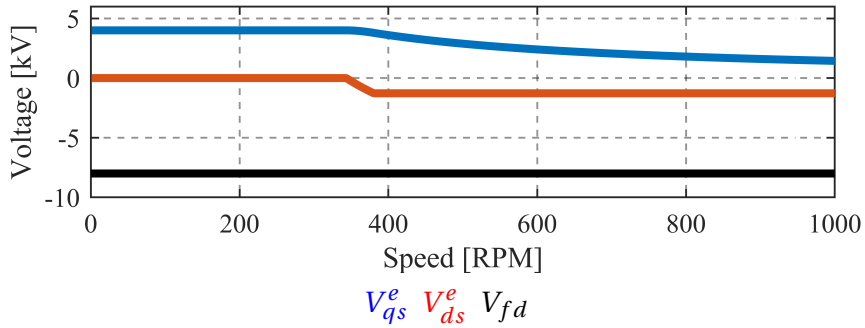

Figure 2.11, Machine dq-axis and field voltage during field weakening with $I_{bus} = 200mA$, $V_{lim} = 4000V$ and $V_{fd} = -8000V$

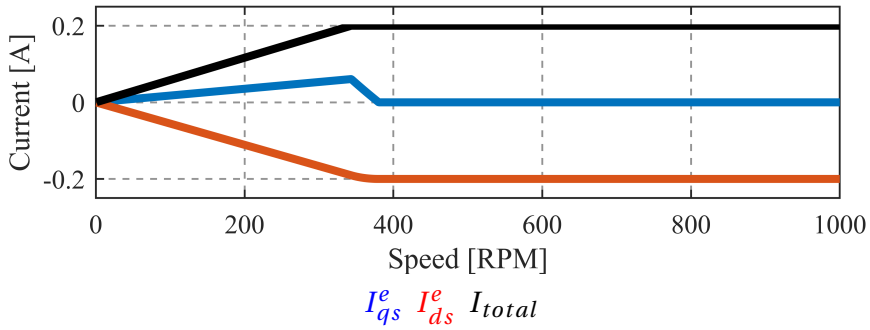

Figure 2.12, Machine dq-axis and total current during field weakening with $I_{bus} = 200mA$, $V_{lim} = 4000V$ and $V_{fd} = -8000V$

$$C_s V_{lim} sin(\gamma) = C_{md} V_{fd} \tag{2.9}$$

If $V_{lim} C_s > V_{fd} C_{md}$ then the back-mmf can be completely canceled at a lower γ. The back-current is completely canceled at the angle given by (2.11) and the d-axis current I_{ds}^e associated with V_{qs}^e can be reduced by scaling the voltage according to speed as given by (2.10) . The machine power factor starts increasing as the terminal voltage is reduced in this region.

$$I_{qs}^e = w_e C_s \frac{C_{md} V_{fd}}{C_s} - w_e C_{md} V_{fd} = 0 \tag{2.10}$$

$$I_{ds}^{e} = -w_e C_s V_{lim} * \frac{I_{bus}}{C_s \omega_e} \tag{2.11}$$

These equations are used to trace the torque, speed, power and power factor curves and shown in Fig. 2.10. The dq-axis voltages and the field voltages are shown in Fig. 2.11. The dq-axis currents and the total current are shown in Fig. 2.12. The field weakening operation on a voltage-limit circle is shown in Fig. 2.13. A constant torque and power factor is obtained when the machine is operating below the current limit. Once the machine hits the current limit, the torque angle γ is changed which results in a reduced torque with a constant power operation. Once the back-mmf is completely canceled, the q-axis voltage is reduced to reduce the leakage current. This results in an improved power factor because of the reduction in voltage for a similar power. The stator side field weakening changes the operating power factor of the machine by changing the dq-axis voltage to allow it to achieve higher speeds with the same DC bus current.

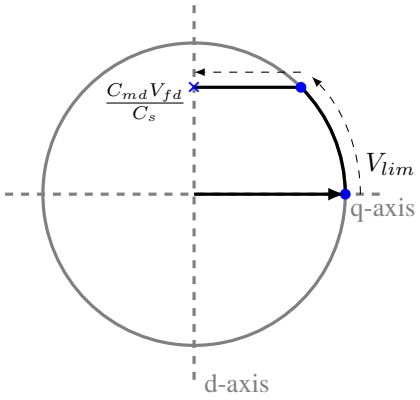

Figure 2.13, Circle diagram for stator side field weakening

2.5.2 Rotor side field weakening

Another method of achieving field weakening is to reduce the rotor field voltage once the DC bus current limit is reached at the maximum speed given in (2.7). The rotor field

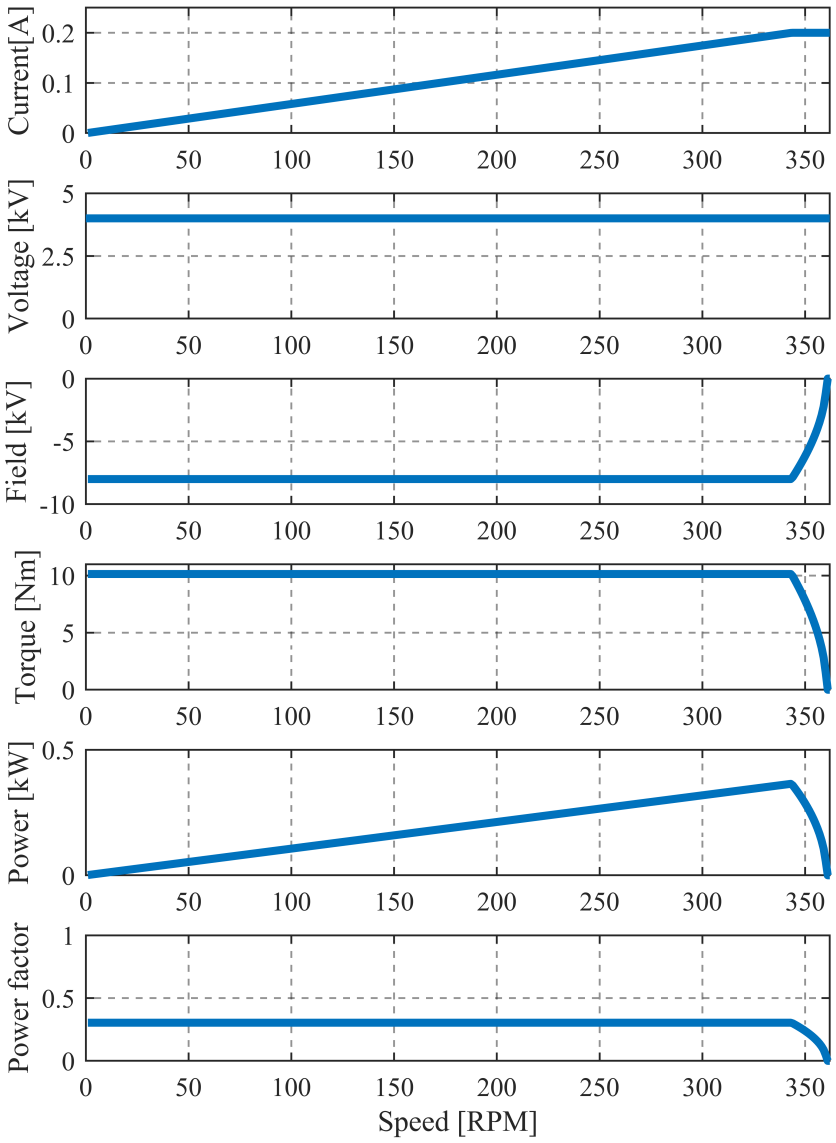

Figure 2.14, Machine currents, voltages,torque, power and power factor limit curves with field weakening implemented by reducing rotor field voltage at $I_{bus} = 200mA$, $V_{lim} = 4000V$ and $V_{fd} = -8000V$

is reduced to operate the machine at the voltage and current limit. The field voltage necessary to keep limit the machine current to the current limit during field weakening

operation is given by (2.12). The steady state torque speed curves for the reduced field voltage is shown in Fig. 2.14. The field weakening operation on a voltage-limit circle is shown in Fig. 2.15. It is evident that the maximum speed that can be achieved with this type of field weakening is significantly lower than the one achieved by the previous method. This is mainly attributed to the fact that the back-current associated with the separate excitation V_{fd} for this machine is approximately 30 % of the total current at rated field and stator voltage due to the high C_s compared to the C_{md}. This method will allow a significant speed increase at higher ratios of C_{md}/C_s. The rotor side field weakening physically reduces the charge available for torque production which inherently reduces the output torque of the machine.

$$V_{fd} = \sqrt{\frac{I_{bus}^2}{C_{md}^2 \omega_e^2} - \frac{C_s^2 V_{lim}^2}{C_{md}^2}} \tag{2.12}$$

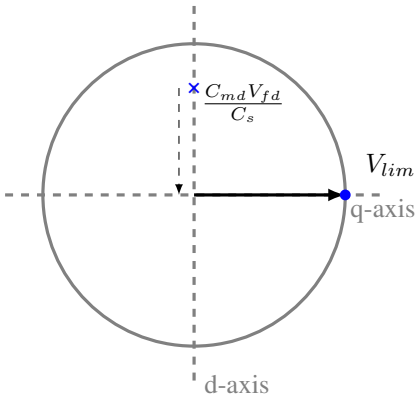

Figure 2.15, Circle diagram for rotor side field weakening

2.6 Summary

This chapter identifies the drive types required for powering electrostatic machines. Multiple drive topologies are compared to understand their advantages and drawbacks

for control of electrostatic machines. Control implementations for the various topologies are presented. The duality between electrostatic machine and electromagnetic machine dynamics is investigated to identify control methods. Steady state machine performance at high speeds with field weakening is analyzed to understand machine performance over a speed range when limited by machine voltage and drive current.

CHAPTER 3

Torque Modulation for SEM

As identified by Chapter 2, a system incorporating charge-oriented control with machine terminal voltage regulation can be implemented to control the torque of the SEM. This chapter investigates the design of high performance voltage regulation to control the machine terminal voltages. A complex vector synchronous frame PI regulator is developed for voltage control. The performance of the controller is experimentally verified. A CSI driven SEM driving a load dyno motor is used for experimental demonstration of torque modulation. The technical content of this chapter has been published in [5, 31, 38].

3.1 A review of the State of the Art

This section summarizes past work in voltage regulation of CSIs. Previous work in high performance current regulation of VSIs is also investigated considering the duality between CSI-VSI systems and the possibility of applying techniques from VSI drives to CSI drives.

3.1.1 Voltage regulation of CSI

VSI based variable speed drives have been the dominant topology for power conversion involving electromagnetic machines. A VSI with current regulation forms the foundation of motor control in high performance torque control applications. CSI systems offer some important advantages over VSI systems with regards to short circuit tolerance. These are especially important while driving large high power loads [37]. CSI based variable speed drives have been used to drive UPS systems and grid connected inverters [39]. The CSI drive requires a capacitor on the output to filter the current before connecting it to an inductive load to avoid voltage ripple and for the switch commutation in SCR based drives. Voltage control across this filter has been investigated in [6, 39, 40] . The dual nature of a CSI and a VSI system is highlighted in [6] . The work proposes application of well studied current control methodologies to voltage control in CSI drives. This is done by mapping VSI modulation methods to the CSI. The paper investigates a synchronous PI and a stationary proportional + resonant controller to control the voltage. This work considers the load on the CSI to be an inductive load and so the VSI system is a first order system while the CSI system is a second order system with the capacitor filter on the output of the CSI. Fig. 3.1 shows a block diagram of the voltage controlled CSI with the VSI to CSI modulation mapping.

Work in [41] investigates an induction machine application for the CSI drive. A new discrete-time stator voltage controller is proposed in this work. The controller is specifically designed to tackle the challenges associated with the resonance due to the filter capacitor and the load inductance. [42] proposes a bang-bang control based modulation and control methodology to improve total harmonic disturbance (THD) of the CSI. The paper uses the synchronous PI regulator as a benchmark to compare the proposed controller. The work also demonstrates that the proposed controller is computationally

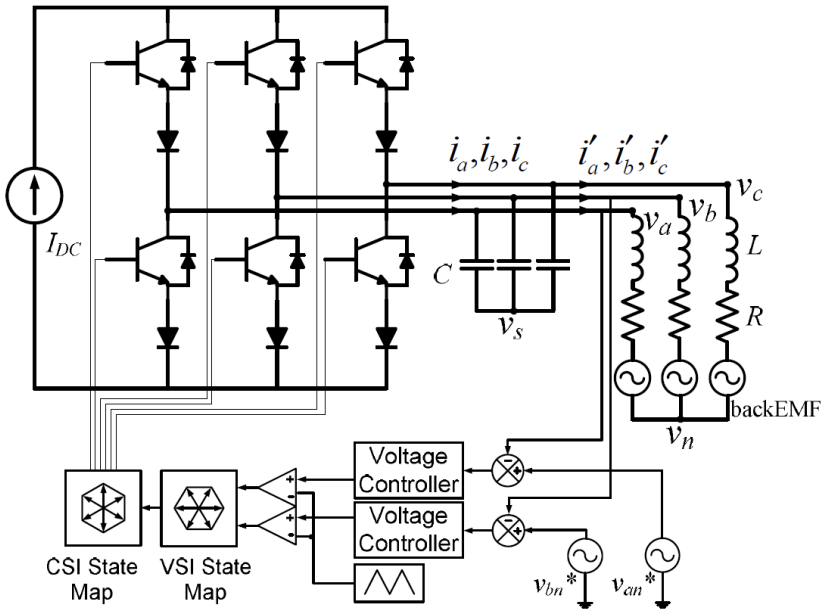

Figure 3.1, Block diagram of a voltage-controlled CSI [6]

lighter compared to the PI voltage regulator.

Work described in [43] proposed an adaptive controller to control the voltage of the CSI. Voltage regulation is experimentally demonstrated. [44] describes a unified approach of the duality in current regulation for voltage source inverters and voltage control in current source inverters.

It is seen that the work undertaken for CSI control is primarily in the areas which consider the resonant effects of the capacitive filter and the machine inductances. These dynamics are however not seen for a CSI based system with a capacitive machine. The capacitive machine in fact, becomes an ideal load for the CSI as the current source can be directly modulated for voltage regulation. Thus from a dynamics perspective this system is closed to a VSI driven inductive machine. The past work undertaken in the field of current regulation for VSI drives is reviewed.

3.1.2 Current Regulation of VSI

Current vector control has been widely investigated for controlling electromagnetic machines [45],[46] and [47]. The work in [46] demonstrates the transition of current regulators from the stationary reference frame to the synchronous reference frame. The stationary frame current regulator has the disadvantage of being load and operating speed dependent. The synchronous frame current regulator exhibits a zero steady state error due to the d and q-axis current becoming DC quantities in the synchronous reference frame. This makes the synchronous frame PI regulator performance independent of the operating frequency at steady state.

The synchronous reference frame transform creates a cross-coupling between the d and q-axis. The degradation of response when operating at low switch frequencies can be compensated using the complex vector model [48]. These effects become significant at high operating speeds which is compensated by the work in [49]. A synchronous frame regulator design is investigated in [50].The synchronous framework in [51] points out the degradation in the transient response of the synchronous frame PI current regulator with increase in the synchronous frequency. This has been attributed to the presence of an asymmetric complex pole due to the synchronous reference frame transform. The study proposes a complex vector synchronous frame PI regulator and a crosscoupling-decoupling based controller to tackle the asymmetric complex pole. The crosscoupling-decoupling based controller is sensitive to parameters. The complex vector current regulator (CVCR) has been shown to provide high performance current regulator while being less sensitive to parameter estimation errors.

3.1.3 Summary of review of the state of the art

While investigations of high performance voltage regulation of CSI drives is documented, studies have focussed towards controlling voltages across a capacitor filter, which along with the machine dynamics exhibits second order properties. The resonant nature of the L-C circuit created by the load and the filter is an important consideration during the controller design. The electrostatic machine from a dynamics perspective is closer to the current controlled VSI. This is based on an assumption of negligible cable inductance from the CSI to the machine. Complex vector current regulation(CVCR) offers a high performance controller design for modulating machine currents. The CVCR exhibits higher performance regulation over a wider speed range due to improved transient performance compared to the synchronous reference frame PI regulator.

3.2 Complex Vector Modeling of SEM

The dq-axis model of a separately excited electrostatic machine and the complex vector voltage regulator framework has been presented in [31]. Equations (3.1)-(3.4) capture the dynamic behavior of the electrostatic machine in the synchronous reference frame. The reference frame transform creates a cross-coupling between the two axes. The block diagram for the electro-mechanical model of the electrostatic machine is shown in Fig. 3.3. The electro-mechanical torque equation is shown in (3.5). The electro-mechanical torque equation includes the torque developed due to the separate excitation and the elastance torque due to rotor saliency. The elastance torque for the machine discussed in this work is negligible due to a non-salient design. The rotor charge of the SEM is aligned with the d-axis. This charge orientation allows independent control of the torque and field by controlling the q-axis and d-axis voltages respectively. Figure 3.2 shows the relation of the complex vector and the stationary and synchronous reference frames.

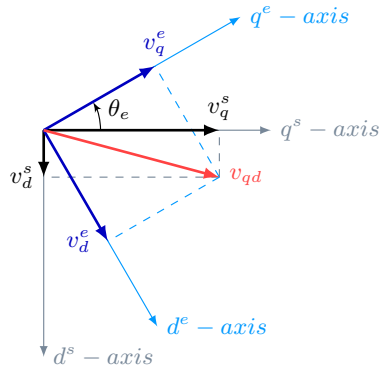

Figure 3.2, Stationary and synchronous reference frames

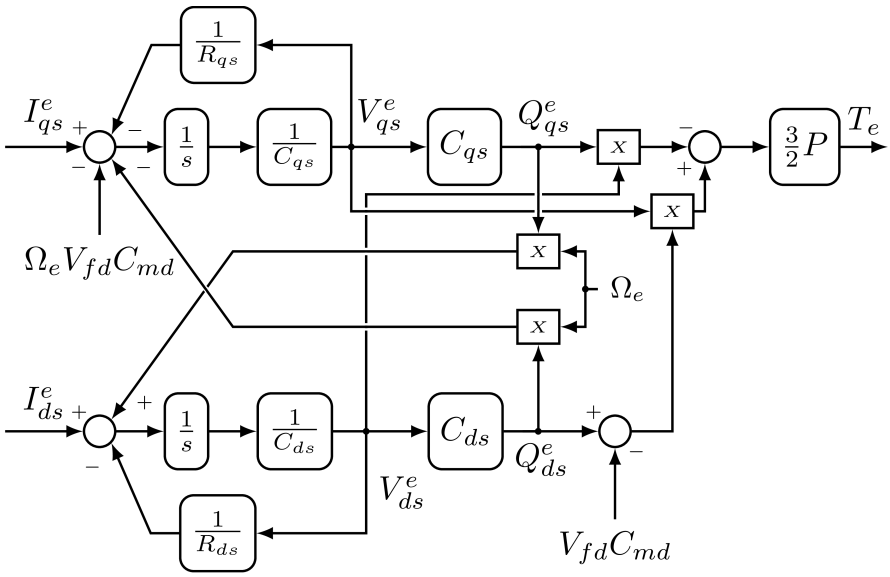

Figure 3.3, Electro-mechanical block diagram of a three phase separately excited synchronous electrostatic machine shown in the synchronous reference frame

The equations also include the back-mmf term $\omega_e v_{fd}$, which is a back-current that arises from the rotating electric field.

$$I^e_{qs} = \frac{1}{R_s} V^e_{qs} + pQ^e_{qs} + \omega_e Q^e_{ds} \tag{3.1}$$

$$I^e_{ds} = \frac{1}{r_s} V^e_{ds} + pQ^e_{ds} - \omega_e Q^e_{qs} \tag{3.2}$$

$$Q^e_{qs} = C_{qs} V^e_{qs} \tag{3.3}$$

$$Q^e_{ds} = C_{ds} V^e_{ds} - C_{md} V_{fd} \tag{3.4}$$

$$T_e = \frac{3P}{2}[(C_{ds} - C_{qs}) V^e_{qs} V^e_{ds} - C_{md} V_{fd} V^e_{qs}] \tag{3.5}$$

The superscript *e* denotes a synchronous reference quantity. The d-axis charge (3.4) shows the rotor charge aligned with the d-axis. This creates the back-mmf orthogonal to the rotor charge seen in the q-axis current (3.1).

A non-salient machine can be represented using complex vectors. The complex vector notation enables the system to be represented in a single-input single-output form. The complex vector to scalar notation mapping is given by (3.6) [45, 51, 52] . The complex vector model for the electrostatic machine is written as (3.7). Figure 3.4 shows the complex vector block diagram of the electrostatic machine in the synchronous reference frame. The model of the SEM in the complex vector form highlights the presence of an asymmetric complex pole at $\frac{1}{R_s C_s}$. This is analogous to the complex pole seen in electromagnetic machines in [51].

$$u_{qds} = u_{qs} - j u_{ds} \tag{3.6}$$

$$I^e_{qds} = \frac{1}{R_s} V^e_{qds} + pQ^e_{qds} - j\omega_e Q^e_{qds} \tag{3.7}$$

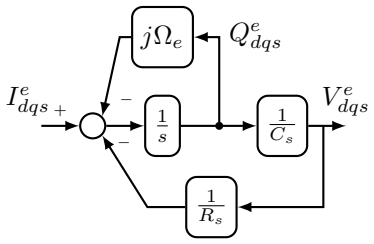

Figure 3.4, Complex vector block diagram of a non-salient synchronous electrostatic machine with the back-mmf decoupled, shown in the synchronous reference frame

3.3 Voltage Regulation for a Capacitive Load

The SEM exhibits dynamics similar to a capacitive load with the additional dynamics of back-mmf. Voltage regulation across an RC load is investigated as the first step towards controlling the voltage across the SEM.

3.3.1 Synchronous reference frame PI voltage regulator

A PI voltage regulator implemented in the synchronous reference frame can provide zero steady state error. Figure 3.5 shows a synchronous reference frame PI regulator for capacitive load.

The complex frequency response function (FRF) of the regulator in the synchronous reference frame is shown by equation 3.8.

$$\frac{V^e_{qds}}{V^{s*}_{qds}} = \frac{k_{vp}s + k_{vi}}{C_s s^2 + (k_{vp} + 1/R_s + \omega_e C_s)s + k_{ip}} \tag{3.8}$$

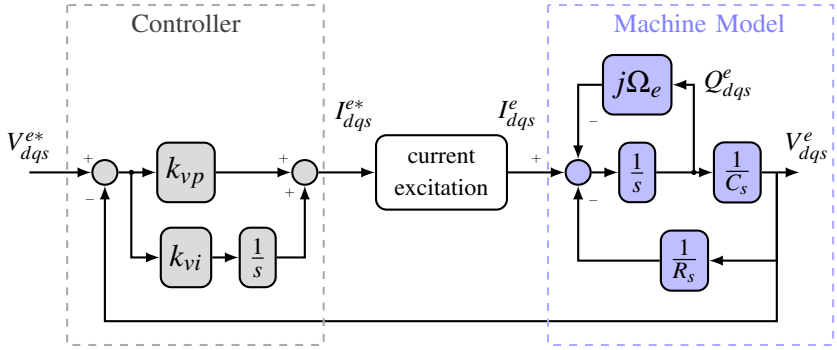

Figure 3.5, Bock diagram of an RC load with a synchronous reference frame PI voltage regulator, shown in the synchronous reference frame

3.3.2 Synchronous reference frame complex vector PI voltage regulator

Similar to electromagnetic machines, electrostatic machines also contain an asymmetric pole created due to the reference transform. The asymmetric pole for the electrostatic machine, which degrades controller performance as the synchronous speed approaches controller bandwidth, lies at $\frac{1}{R_s C_s}$. The complex vector controller is utilized to cancel out this complex pole. Figure 3.6 shows the block diagram of the complex vector voltage PI voltage regulator for an electrostatic machine.

Equation 3.9 gives the complex FRF for the CVVR in the synchronous reference frame.

$$\frac{V^{e}_{qds}}{V^{s*}_{qds}} = \frac{k_{vp}s + k_{vi} + j\omega_e k_{vp}}{C_s s^2 + (k_{vp} + 1/R_s + \omega_e C_s)s + k_{ip} + j\omega_e k_{vp}} \tag{3.9}$$

3.4 Voltage control for SEM

For controlling an SEM, the back-mmf can be decoupled in the controller to obtain dynamics similar to an RC load. Figure 3.7 shows the block diagram of the complex vector voltage regulator with back-mmf decoupling.

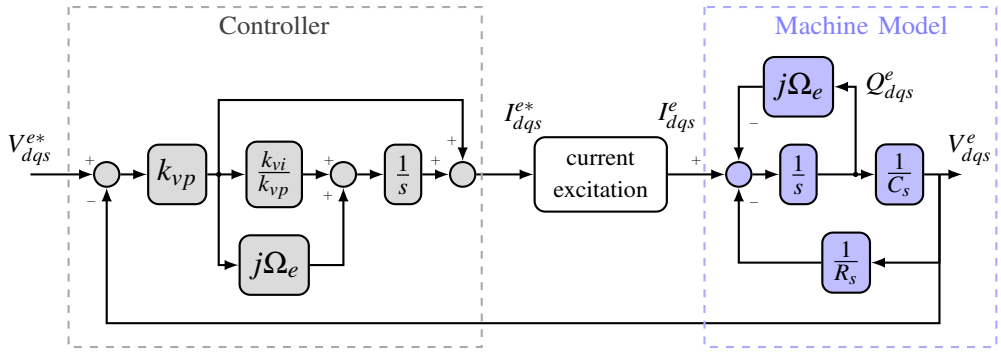

Figure 3.6, Complex Vector Voltage Regulator block diagram for a three-phase RC load, shown in the synchronous reference frame

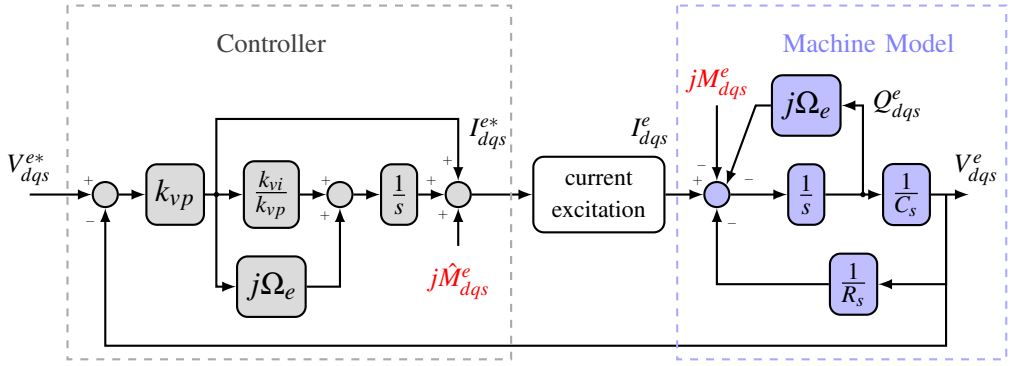

Figure 3.7, Complex Vector Voltage Regulator block diagram the SEM with the back-mmf decoupled, implemented in the synchronous reference frame

With the back-mmf decoupling the FRF will be similar to a the response for an RC load.

The dynamic stiffness for the complex vector voltage regulator is given by (3.10).

$$\frac{I^s_{dist-qds}}{V^s_{qds}} = C_s + \frac{1}{R_s} + k_v p + j\omega_e C_s + \frac{k_{vp}}{s}\left(\frac{1}{R_s C_s} + j\omega_e\right) \tag{3.10}$$

The dynamic stiffness represents the ability of the controller to reject disturbances. For a voltage regulator the dynamic stiffness has the units of $\frac{1}{\omega}$ which represents a conductance to a current disturbance. A higher conductance would result in a lower *voltage disturbance* created due to the corresponding current disturbance.

Figure 3.9 shows a comparison of the frequency response function for a synchronous

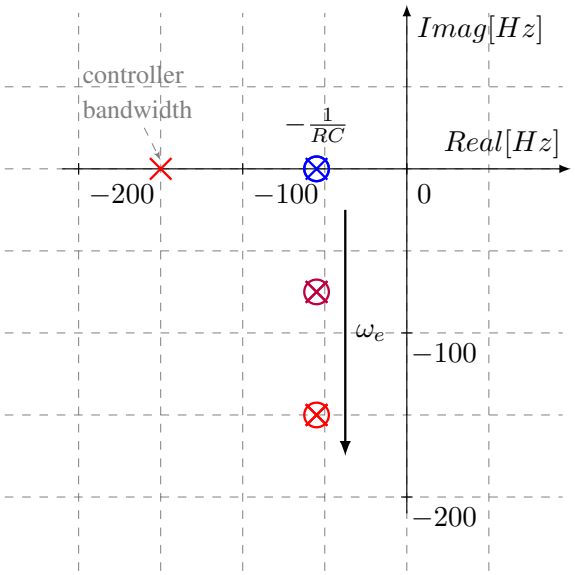

Figure 3.8, Pole migration for CVVR shown in the synchronous reference frame

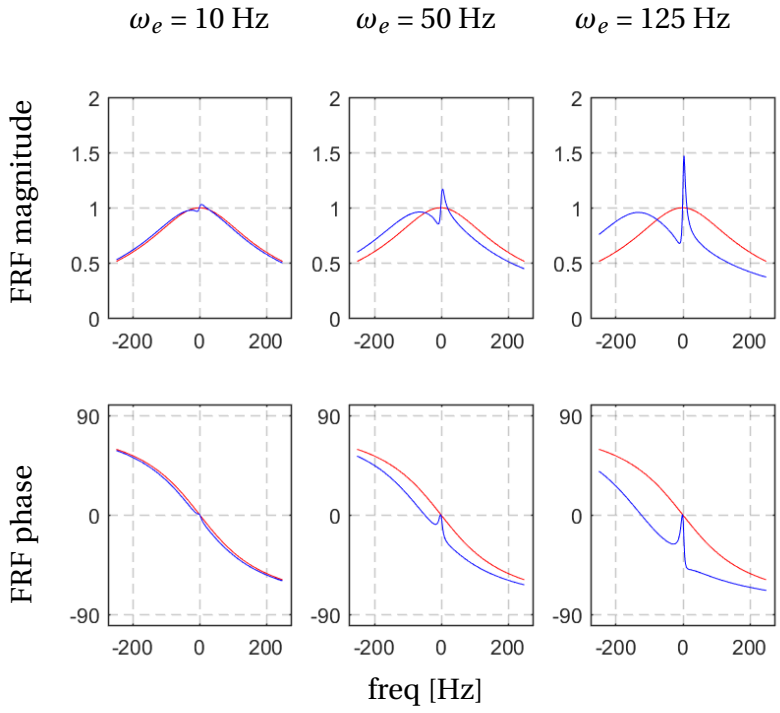

Figure 3.9, Frequency response function magnitude and phase in the synchronous reference frame with varying synchronous frequency. Tuned to a 150 Hz bandwidth

PI regulator and the CVVR in the synchronous reference frame. The controller is tuned to 150 Hz. The controller tuning is shown in (3.11) and (3.12) where f_b represents the desired bandwidth of the controller. At zero synchronous frequency both controllers have similar performance due to the absence of the speed dependent cross-coupling. As the synchronous frequency starts increasing the performance of the synchronous PI regulator starts degrading. It should be noted that the synchronous PI regulator has a unity gain at 0 Hz in all cases which indicates a unity gain at the synchronous speed. However, the degradation in the frequency response will cause the transient response to degrade. The CVVR on the other hand exhibits similar dynamics irrespective of the synchronous frequency.

$$k_{vp} = 2\pi f_b C_s \tag{3.11}$$

$$k_{ip} = \frac{2\pi f_b}{R_s} \tag{3.12}$$

3.5 Complex Vector Voltage Regulation in the Discrete Time Domain

The effects of discrete time implementation of the complex vector regulators have been investigated in detail in [53]. It has been shown that a direct discrete time implementation of the CVVR exhibits an oscillatory behavior for high fundamental to sampling frequency ratios. An implementation of the CVVR which accounts for the delays and dynamics associated with high fundamental to sampling frequencies has been proposed in [53]. A similar compensation model can be used for improving the performance of voltage regulators when implemented in the discrete-time domain.

3.6 Experimental Verification of Torque Modulation

3.6.1 Test Stand

The SEM is mounted on a testbed as shown in Fig. 3.10. Figure 3.11 shows the control block diagram of the test setup. The machine is coupled to a Schneider Electric $BSH1003P11A2A$ PM machine. The specifications of both the machines are provided in Table 3.1 and Table 3.2. The electrostatic machine and the PM machine are of similar torque ratings.

Table 3.1, SEM1 Specifications.

Parameter	Value
Stator Voltage (l-l) [kV]	4.95
Rated Torque [Nm]	9
Poles	96
Max Speed [rpm]	1200
Stator Capacitance [nF]	13.7
Mutual Capacitance [nF]	2.2
Stator Resistance [MΩ]	1.7
Rated Rotor Voltage (diff) [kV]	8

Table 3.2, $BSH1003P11A2A$ Specifications.

Parameter	Value
Rated Current [A]	6.6
Rated Torque [Nm]	8
Poles	4
Rotor Speed [rpm]	4000

The PM machine is controlled in speed mode by a AMC DPEANIU-015S400 variable frequency drive and the SEM is controlled in a torque mode. The drive specifications [54] are provided in Table 3.3. Mechanical torque is measured using a Himmelstein

$MCRT48001V(1-2)NFN15000G$ torque sensor with a 11.29 Nm (100 lb-inch) torque rating.

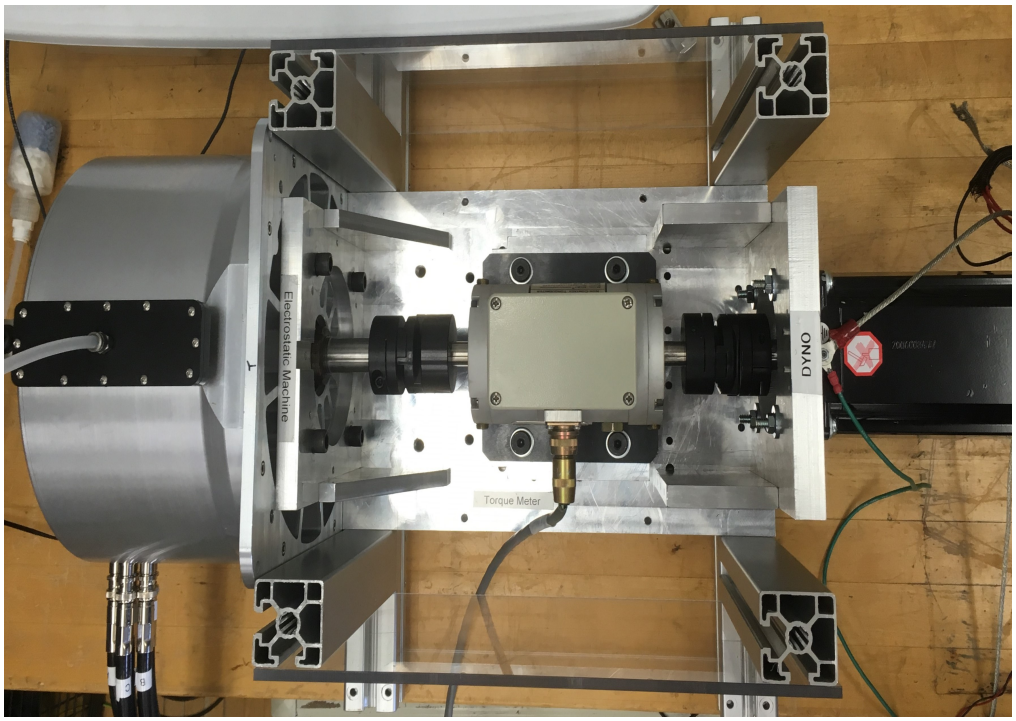

Figure 3.10, Electrostatic machine test setup showing SEM, load motor and torque transducer

Table 3.3, Dyno Drive Specifications.

Parameter	Value
Rated Current [A]	7.5
Rated Voltage [V]	373
Switch Frequency [kHz]	20

3.6.2 Controller Platform

A TI 28379D Dual Core Microcontroller Unit (MCU) is utilized for implementing the control software. The control card shown in Fig. 3.12 runs at a 200 Mhz clock frequency

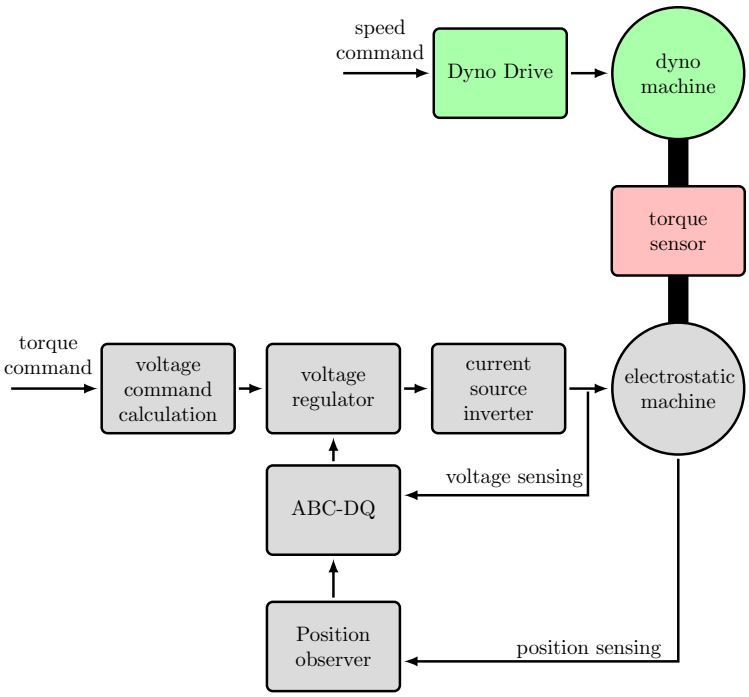

Figure 3.11, Block diagram showing experimental setup comprising of SEM, load motor and torque transducer

and one core of the MCU is utilized for this drive. The following key features make the 28379 control card useful for implementing the CSI-PWM:

- On board 12-bit Analog to Digital Conversion.
- Shadow registers for delayed PWM configuration.
- Dedicated I/O for motor position feedback.

The CSI-PWM requires the PWM configuration to change in every SVM sector. This is typically challenging to achieve without external hardware as most DSPs offer complementary PWM channels which are better suited for VSI implementations. The extra register configuration available in the TI 28379D MCU enables implementation of the CSI without any external hardware along with dead-time. An external digital circuit designed by Peter Killeen offers open circuit protection in the event of an MCU failure.

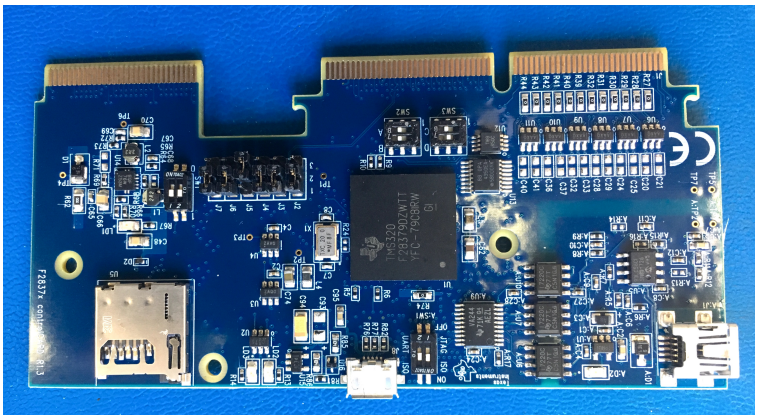

Figure 3.12, TI 28379D Control Card

3.6.3 Space Vector Modulation

The CSI-PWM is modulated with space vector modulation (SVM). The space vector diagram is shown in figure 3.13. The vectors I_1 to I_6 are active states and the state I_0 is a zero state. The active states consists of one switch on for the full state and the switches on the other side in PWM mode to control the current. The other switches on the same side are off in that state. The zero state is a bypass state where both the higher and the lower switch on one leg close to bypass the DC bus.

A center-symmetrical PWM is implemented with sampling at the center of the waveform [37, 55].

3.6.4 CSI based drive

A high voltage CSI as described in Chapter 2 has been developed by Peter Killeen [5] for driving electrostatic machines. The drive utilizes series-stacked switches to achieve the medium voltage levels required by the electrostatic machine. Four 3.7 kV IGBTs are connected in series to provide a maximum voltage blocking rating of 14 kV. Figure 3.15 shows the configuration of the drive. The series-stacked devices shown in Fig. 3.16 have a

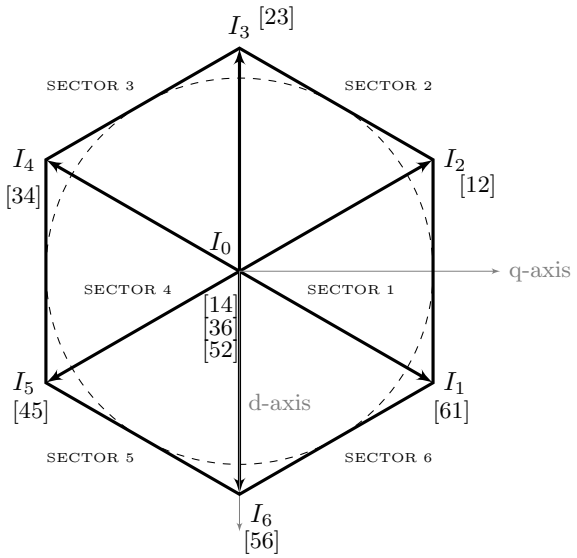

Figure 3.13, SVM hexagon showing the six sectors for CSI-PWM

snubber circuit to allow passive balancing of the voltages across the switches. The drive requires a current supply as the input. An H-Bridge switching at 20 kHZ along with a high frequency transformer and a diode rectifier generates the current source required for the CSI. The CSI requires an inductor on the DC bus for regulating current and reducing the ripple magnitude. This drive utilizes a total of 14 H (less than 1 J stored energy for 100 mA current) inductance divided between the input and return path of the current source front-end. Each inductor is individially 7H and is custom designed for a bus current upto 150 mA. A current loop using measured DC link current is implemented for DC bus current regulation. The control framework for the front-end and the CSI is detailed in Appendix B.

The drive uses the SVM modulation with a switch frequency of 9 kHz. The selected switch frequency has been verified to provide balanced voltages with reasonable voltage imbalances on the individual switches in the the series-stack. Running the system at higher frequencies would require further analysis of voltage stress on switches during switching transients.

The SEM also requires a medium voltage separate excitation. The separate excitation is a ground centered positive and negative voltage. The separate excitation is provided by EMCO high voltage power supplies. Two EMCO $F40$ supplies which are rated to provide an isolated 0 to 4 kV voltage at 2.5 mA current output are used for providing the separate excitation. For purpose of the experiments performed in this chapter, the output of the power supplies is set to a constant value. Figure 3.14 shows a picture of the EMCO power supply.

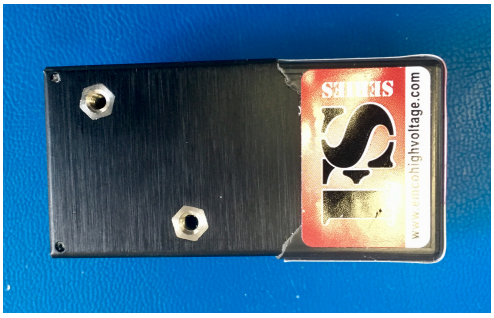

Figure 3.14, EMCO-FS40 High voltage power supply used for rotor excitation

3.6.5 Feedback signals

Torque control of the SEM requires closed loop voltage control. This requires terminal voltages to be measured and feedback to the drive. The terminal voltages are deferentially measured and fed into the ADC of the DSP using a board designed by Peter Killeen. The differential voltage measurement doesn't require a grounding or isolated measurement.

The stator voltage must be controlled according to the rotor position. The machine has a high pole count which requires a high position measurement resolution. An absolute encoder is used for this purpose. The 15-bit SICK AFS60B-BDPA032768 absolute encoder is used for rotor position measurement. The 15-bit resolution provides a resolution of 1.054 electrical degrees per bit.

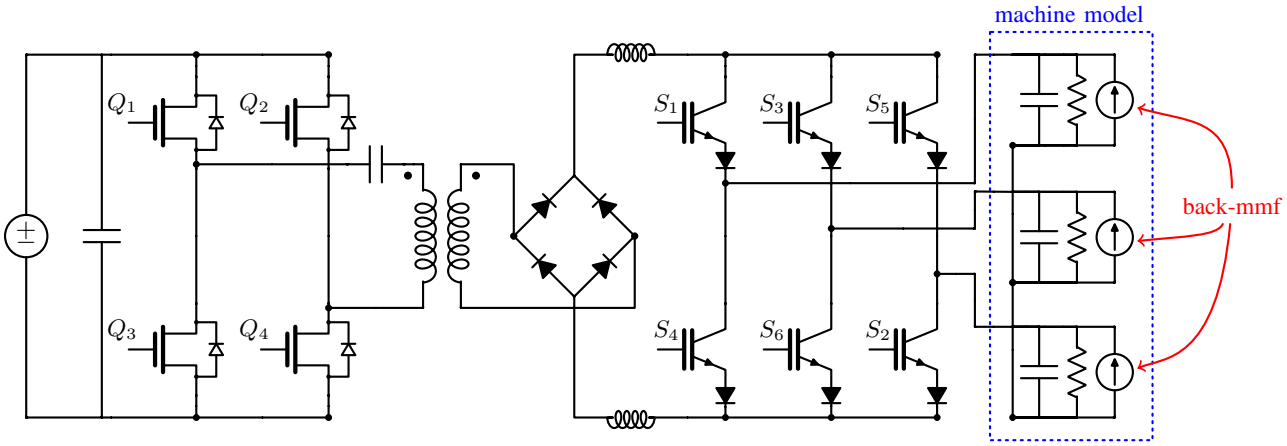

Figure 3.15, CSI Drive hardware configuration for SEM testing showing the front-end with the CSI and the SEM equivalent circuit

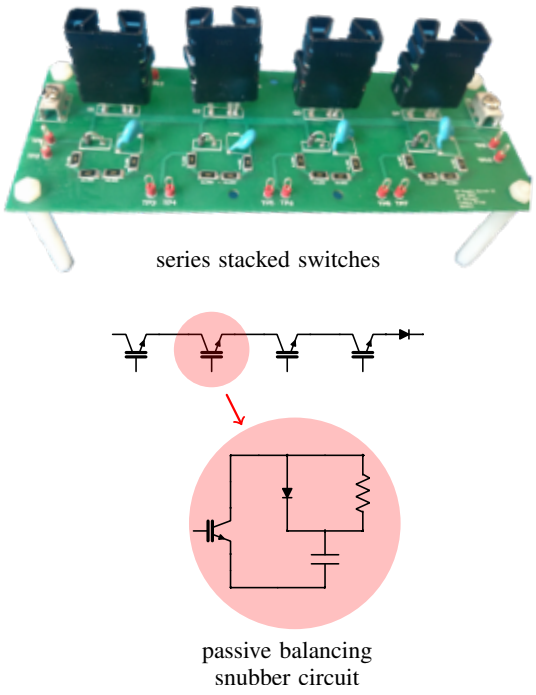

Figure 3.16, Circuit diagram of passive snubber circuit for voltage balancing and hardware realization of the series-stack switch

3.6.6 Position feedback

The machine is mounted with an absolute encoder for position measurement. The encoder communicates with the DSP with an SSI protocol. This provides high speed communication. The position signal is then fed to a Luenberger-style position observer as described in [56]. The position observer reduces the sensor noise and also provides an average estimated velocity signal. The velocity signals are then used for voltage and speed control. The position is measured at the switch frequency (9 kHz) and the speed is computed at 1 Khz.

3.7 Voltage Regulator Performance

Performance of the voltage regulator is evaluated by observing the frequency response and the dynamic stiffness of the voltage regulator.

3.7.1 Frequency response of voltage regulator

The SEM was run at a constant speed by commanding speed on the dyno motor. To measure the frequency response of the voltage regulator a chirp waveform was commanded over a constant voltage command. The dc offset voltage helps to get the operating point out of any non-linearities that might exist in the power supply at lower excitation values. To measure the complex FRF, a complex chirp waveform was injected. The function for the implementation of the chirp signal is given by (3.13). Figure 3.17 shows the rotating chirp signal used for exciting the negative and positive frequency content.

$$f(t) = sin\left(\phi + 2\pi\left(f_o + \frac{kt^2}{2}\right)\right), k = \frac{f_1 - f_0}{2} \tag{3.13}$$

Figure 3.17 shows the dq components of the rotating chirp waveform. The phase of the signals reverses at 0.5$seconds$. This is used for including both the negative and positive frequencies. The complex FRF was then extracted from the commanded and measured voltage signals.

Table 3.4, Controller Gains for FRF evaluation.

Parameter	Symbol	Value
Controller bandwidth [Hz]	f_b	150
Proportional Gain [1/Ω]	k_{vp}	1.22E-5
Integral Gain [s/Ω]	k_{vi}	5.54E-4

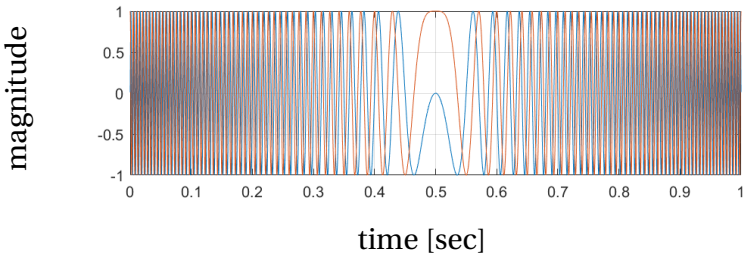

Figure 3.17, Orthogonal components of a linear rotating chirp signal with frequency varying from zero to 100 Hz

Figure 3.18 shows the measured FRF for the controller. The bandwidth of the controller is set to 150 Hz to exaggerate the roll-off of the controller within the frequency range that the inverter can produce. The controller tuning is shown in Table 3.4. Figure 3.18 shows that the measured signals lie within an acceptable value of the simulated waveform. The FRF also shows a drop in magnitude and coherence at the negative synchronous frequency for both the waveforms. This point is around 0 Hz in the stationary reference frame. The drop in coherence is attributed to the fact that the inverter does not require a high enough current while controlling the zero hertz and so the signal might not have a very high coherence. The measurement is not performed at higher voltages to avoid voltage breakdown in the SEM.

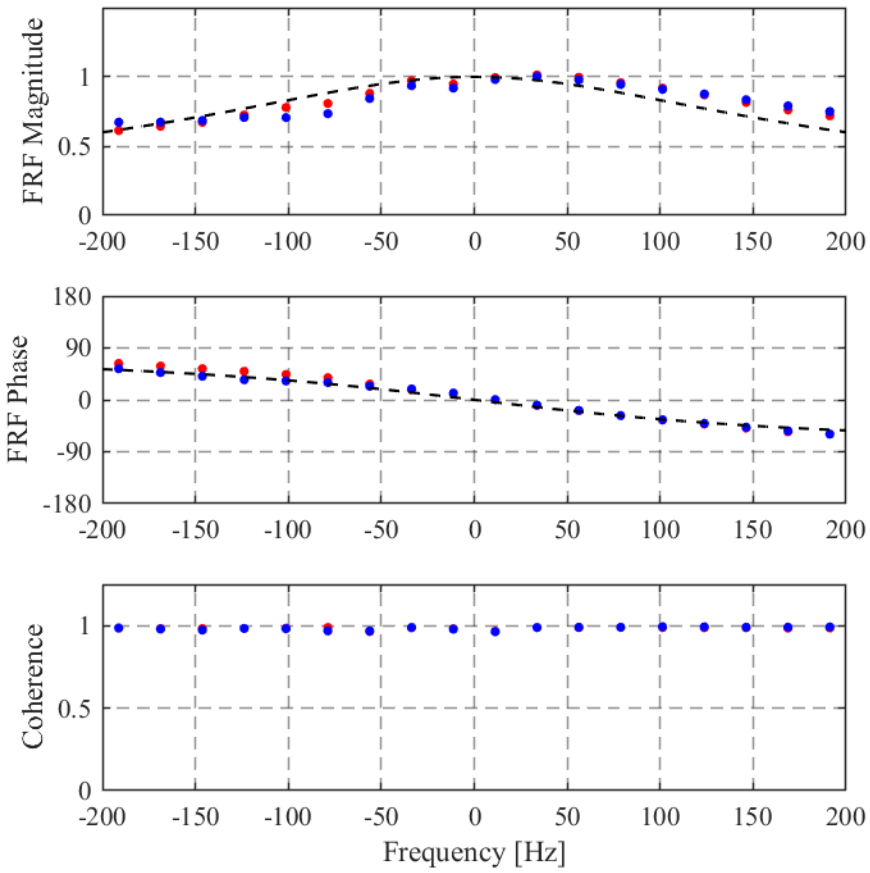

Figure 3.18, Experimental complex vector FRF for a complex vector synchronous frame PI regulator with f_{bw} = 150 Hz for f_e = 30 and 100 Hz

3.7.2 Dynamic Stiffness

Dynamic stiffness of a regulator is the ability of the control to reject disturbances. The dynamic stiffness for the CVVR is evaluated by injecting a disturbance noise on the current sources into the machine. Figure 3.19shows the injected current noise in the system. The voltages disturbance caused by this injected current signal is measured and the dynamic stiffness is computed. The voltage regulator is tuned to 300 Hz with the controller gains shown in Table 3.5.

Table 3.5, Controller Gains for DS evaluation.

Parameter	Symbol	Value
Controller bandwidth [Hz]	f_b	300
Proportional Gain [1/Ω]	k_{vp}	2.4E-5
Integral Gain [s/Ω]	k_{vi}	1.1E-3

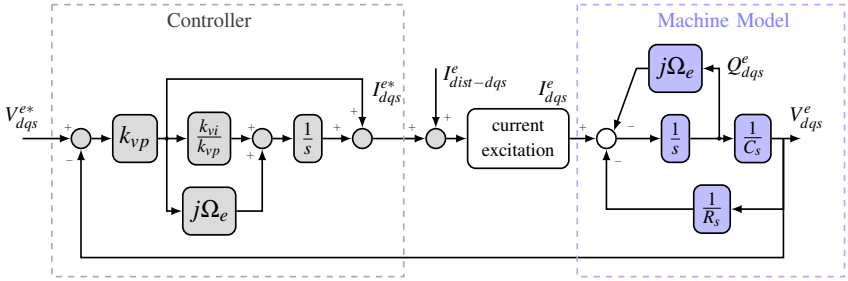

Figure 3.19, Complex vector synchronous frame PI voltage regulator with disturbance current injection for disturbance

Figure 3.20 shows measured dynamic stiffness for the current regulator tuned to 300 Hz. The measurement is performed at two synchronous frequencies. The figure also compares measured waveforms with simulated waveforms. The coherence is low at zero hertz in the synchronous reference frame due to the fact that the CVVR exhibits infinite stiffness at the synchronous frequency.

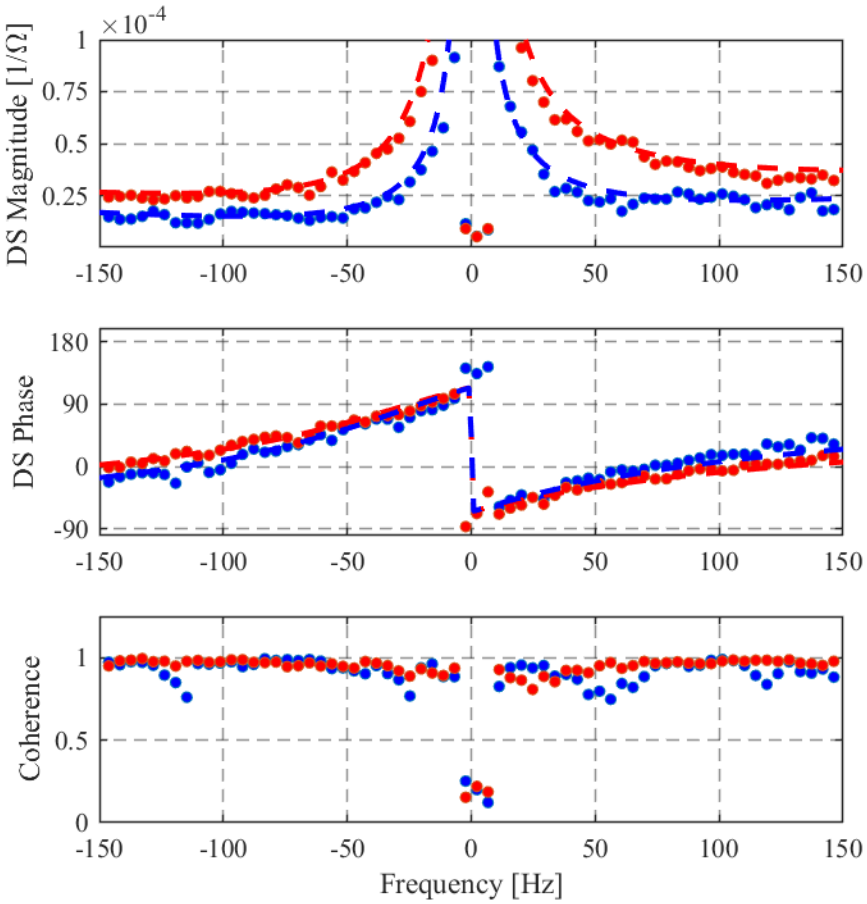

$f_{bw} = 150\ Hz$ $f_{bw} = 300\ Hz$
– simulated ·· measured

Figure 3.20, Experimental complex vector dynamic stiffness for a complex vector synchronous frame PI regulator with f_{bw} = 150 Hz and f_{bw} = 300 Hz for f_e = 30Hz (18.75 rpm)

The physical interpretation of the infinite dynamic stiffness at 0 Hz is that the controller is able to perfectly reject any disturbances such as the back-mmf which occur at the synchronous frequency. The dynamic stiffness plots include both the positive and negative frequencies as the machine can be run in both directions.

3.7.3 Torque Control

The objective of this section is to experimentally demonstrate torque modulation of the SEM in the time-domain. This is done by commanding a q-axis voltage with the field powered. Figure 3.21 shows the voltage command tracking and the torque command tracking at zero speed. The machine rotor is locked and torque is measured using a torque transducer. The voltage command tracking shows the command tracking response of the voltage regulator. The voltage and torque axes in Fig. 3.21 are scaled according to (3.14) so that the voltage command represents an appropriately scaled torque command. The q-axis voltage command and response correlates to the corresponding machine torque given by (3.14). The oscillation on the measured torque waveform is due to the

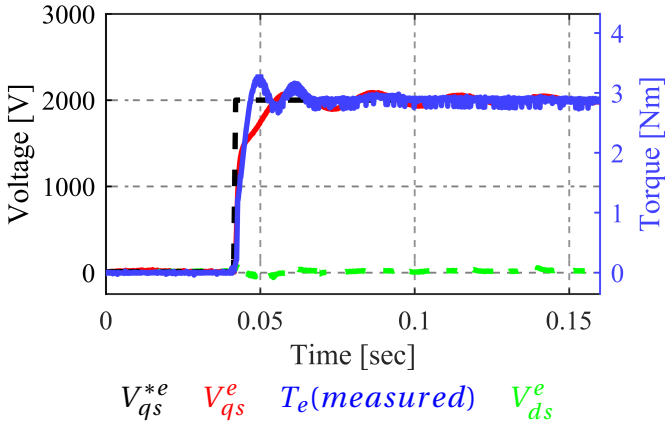

Figure 3.21, Experimental evaluation of torque command tracking response showing scaled q-axis voltage command in the synchronous reference frame and measured shaft torque at stall with V_{fd} = 5 kV

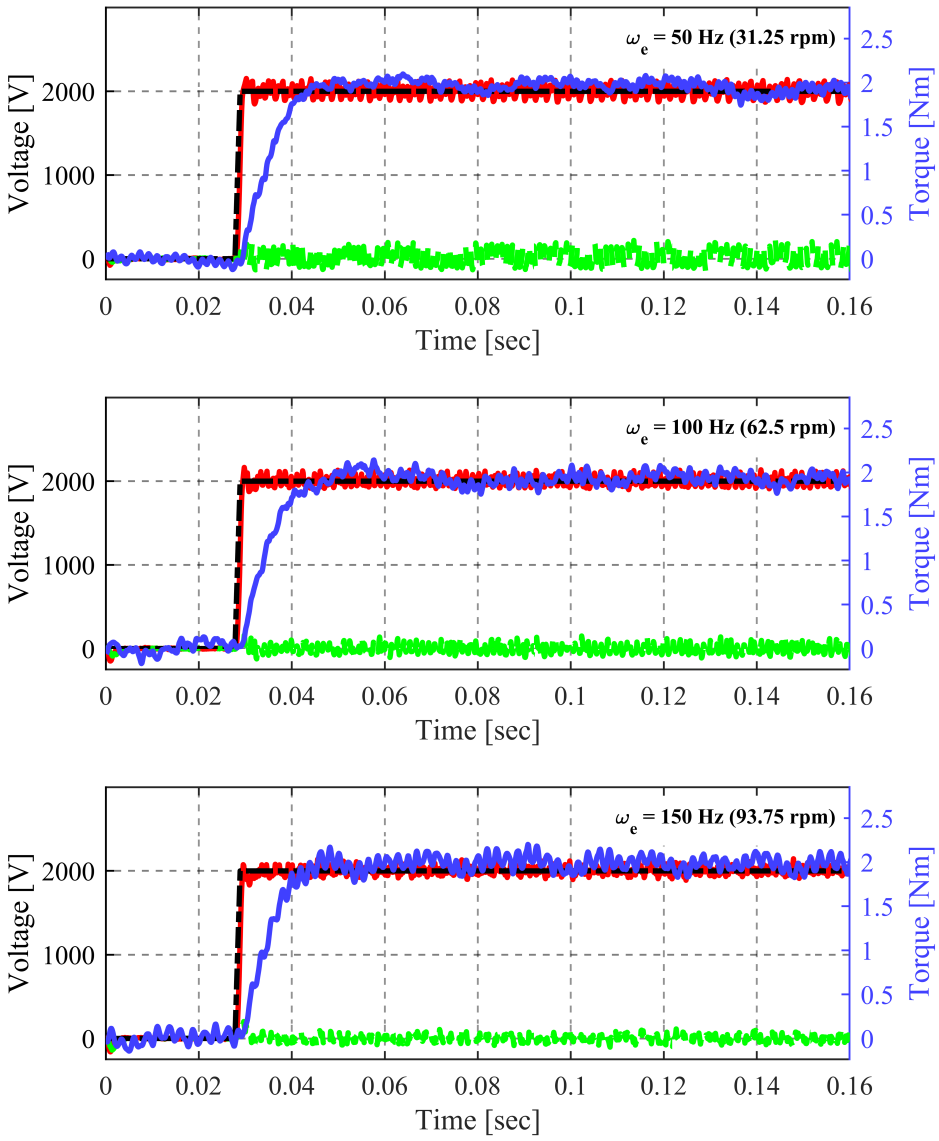

Figure 3.22, Experimental evaluation of torque command tracking response showing scaled q-axis voltage command in the synchronous reference frame and measured shaft torque at f_e = 50 Hz (31.25rpm), 100 Hz (62.5rpm) and 150 Hz (93.75rpm) with V_{fd} = 3 kV

resonant frequency of the shaft coupling between the motor and the torque transducer. The response demonstrates the holding torque capability of the SEM to potentially drive 'position and hold' type applications.

$$k_T = \frac{3P}{2} C_{md} * V_{fd} \quad [^{Nm}/_{V}] \tag{3.14}$$

The SEM rotor is then held at a constant speed with the dyno motor and q-axis voltage steps are commanded to demonstrate toque modulation at speed. Figure 3.22 shows the measured torque and machine voltages for a step q-axis voltage command. The voltage and torque axes are scaled similar to Fig. 3.21. Figure 3.22 demonstrated a torque response independent of the machine speed upto the drive bandwidth. The measured torque response includes the dynamics of the dynamometer speed regulator reacting to the step torque on the SEM leading to a slower rise time compared to the voltage signal.

3.8 Voltage Regulation for Salient Pole Machines

The previous sections address the dynamics and control for a non-salient machine. A salient pole machine will require a scalar representation [57] as shown in Fig. 3.23 for control. A more elegant representation of the complex vector regulation for asymmetric systems is presented in [58].

3.9 Summary

A complex vector model of the SEM is developed for design of high bandwidth terminal voltage regulation for the SEM. Dynamic response of the machine is experimentally verified. Torque modulation of the machine is experimentally verified at varying machine speed by implementing the complex vector voltage regulator on a medium voltage CSI

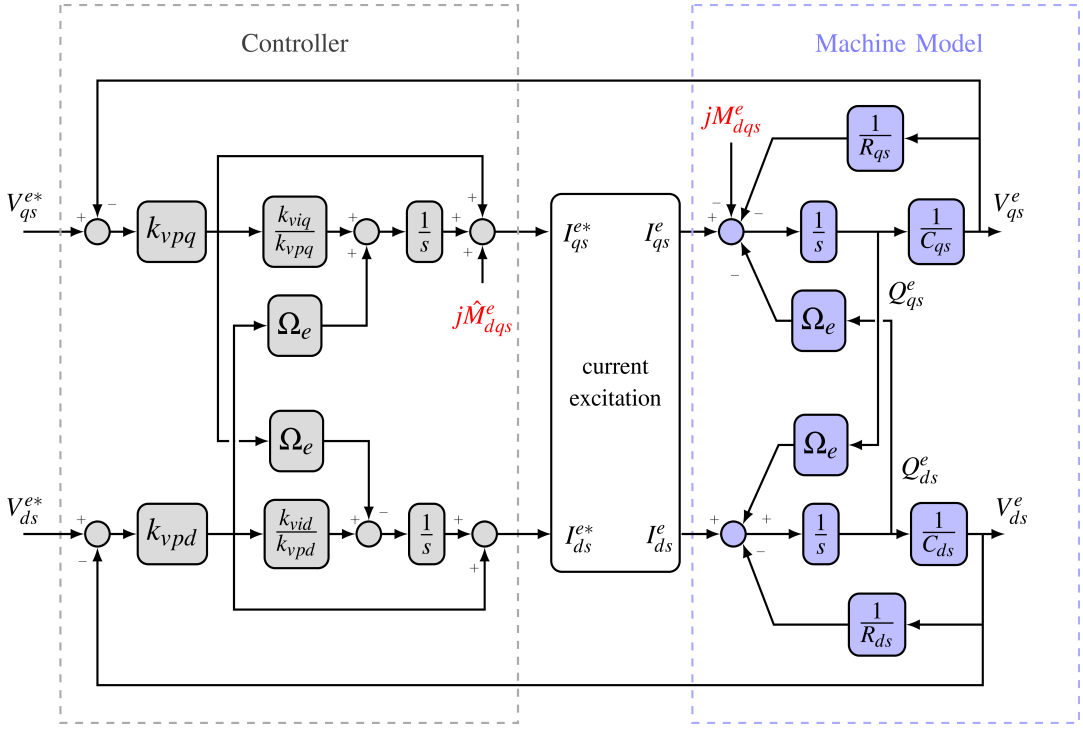

Figure 3.23, Bock diagram of an RC load with a synchronous reference frame PI voltage regulator, shown in the synchronous reference frame

drive. A current source inverter platform built to source ampere-seconds (charge) was used to experimentally verify performance of the CVVR. Torque modulation of the SEM was experimentally demonstrated using terminal voltage resulation with charge-oriented control. Torque steps up to 3Nm and voltage steps of 2kV were achieved with a response time of less than 10 ms at stall and rotating operation.

CHAPTER 4

Rotor Position Self-Sensing

Chapters 2 and 3 detail the development of voltage regulators for the SEM and ultimately achieving motor torque modulation. A primary factor aiding torque control is the ability to align the machine rotor and achieve charge-oriented-control using the rotor position information. This section presents methodologies for self-sensing of the rotor position as alternatives for using encoders. The advantages and limitations of encoders which lead to self-sensing being an attractive alternative are discussed. The technical content of this chapter has been published in [59].

4.1 Introduction

Accurate knowledge of rotor position is crucial for implementing high performance closed-loop control methods. However, position sensors add cost to the system. Along with being a point of failure, they increase the volume and weight of the machine. The SEM which has been designed with a focus on weight and cost is also sensitive to the

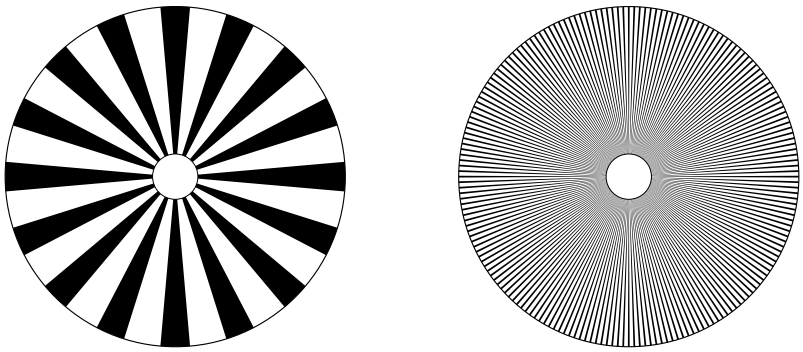

Figure 4.1, Visual representation of a (left) 8-pole rotor and a (right) 96 pole rotor where each black segment is a rotor pole

challenges added by the position sensor. Along with increase in cost, weight and volume, the SEM pole count necessitates a need for self-sensing. The SEM 1 has a relatively high pole count of 96 which is chosen for improved torque production as identified in [2]. A visual representation which illustrates the resolution difference between an 8-pole pair rotor and a 96-pole pair rotor is shown in Fig. 4.1. It is worth noting that from the analysis performed in [2] it is infered that electrostatic machines can have an even higher number of poles for optimized torque production which compels the use of higher resolution position measurement.

One approach to increase the resolution is to use a high count position sensor. However, the cost of the position sensor increases for a higher resolution. Table 4.1 compares the cost of different types of position sensors including the sensor used for the experimental verification of the machine (SICK : AFS60) [60],[61]. The costs shown in the table are the costs of the sensor itself. Actual use of the sensor would require cable and additional measurement circuit cost. The machine currently uses a 15-bit absolute encoder for position information. The resolution of the encoder in electrical degrees is given by (4.1). Even with the 15-bit encoder the electrical angle resolution is approximately 1 degree per bit. Any errors in the machine rotor alignment due to inadequate position accuracy can

cause reduction of machine output torque.

$$resolution = \frac{360 * P}{2^{15}} = 1.054 \, \frac{deg}{bit} \tag{4.1}$$

Table 4.1, Encoder Cost Comparison.

Make	Model	Type	Steps per rev	Cost [$]
SICK	AFS60	Absolute	32768	750
SICK	ARS60	Absolute	4096	671
SICK	SKM36	SinCos	4096	227
SICK	ARS60	Absolute	360	554
Baumer	HS35F	Incremental	5000	480
Baumer	ITD21	Incremental	512	509

The more promising approach to tackle this challenge of position resolution is self-sensing. The use of the machine drive signals to provide rotor position information or 'self-sensing' has been widely investigated for electromagnetic machine rotor position self-sensing [62–68]. Rotor position self-sensing offers an attractive solution for alleviating the challenges associated with using a position encoder at no addition system cost or changes to the machine or drive platform.

4.2 A Review of Self-Sensing Methodologies

The methodologies that have been utilized for self-sensing for rotor position for electromagnetic machines are reviewed. These methodologies are broadly classified into back-emf based and high-frequency signal injection based. The classification arrived from the speed dependency of the back-emf signal which drives the need for an alternate estimation method which relies on injecting high frequecy signals at low speeds.

4.2.1 Back-emf based self-sensing

The rotating magnetic field on the machine rotor generates a back-emf signal with magnitude proportional to the speed of the rotor and phase alligned to rotor position. The back-emf signal has been widely used for extracting rotor position information [63, 68–70]. This methodology is sufficient for spinning the machine without the use of a position sensor when the application primarily demands a continuous medium to high speed. The machine is brought out of standstill position by a variety of methods including a slow rotating current vector commands and once the machine is spinning, the resultant back-emf signal is used to close the speed loop and speed up the machine.

Back-emf sensing methodologies are fundamentally based on the estimation of the back-emf signal from drive signals such as the feedback current and the commanded drive voltage. The back-emf signal itself can be extracted using a variety of methods which include current observers [71], extended Kalman Filters [72, 73] or sliding mode observer based [74]. The rotor position signal is then extracted from the back-emf signal using various methods such as position tracking observers [75, 76] or directly computing the position using an arc-tangent computation [77]. Back-emf self-sensing provides reliable estimates of the rotor position over a medium to high speed operating range. This method is not able to provide position estimates at the zero and low speed range due to the inherent proportionality of the back-emf signal with the machine rotor speed. The back-emf based method starts exhibiting higher estimation errors as the speed decreased due to reduction in signal to noise ratio of the estimated back-emf signal. Work done in [71] aims at extending the low speed operating range of the back-emf sensing algorithm. The study brings up the important observation that the non-linearities associated with the inverter can add significant harmonic content to the estimated back-emf. This is especially important at low speeds as the voltage command for providing the back-emf

signal drops significantly and inverter harmonics become a significant percentage of drive output voltage. A methodology of compensating for the dead-time has been shown to improve low-speed performance. Individually compensating for inverter harmonics has also been investigated in [78]. Along with compensation of machine non-linearities, compensation for parameter changes using online-parameter estimation methods have also been shown to significantly improve the sensing performance [79].

4.2.2 Signal injection based self-sensing

Back-emf self-sensing offers a low cost sensor-replacement solution which is limited to medium and high speed operation. In order to estimate the machine position at standstill and low speeds a high frequency signal is injected in the machine and the resultant signal is used for rotor position estimation [62, 66, 67]. This high frequency signal is chosen so that it does not interfere with the fundamental frequency of the current which is associated with the power transfer. The high frequency signal typically produces a small ripple on top of the fundamental frequency and can be separated by some form of a high pass filter for further processing to extract the position information. The fundamental objective of high frequency signal injection is to identify the machine impedance at the high frequency. This includes the machine saliency arising out of differences in the d-axis and q-axis inductance as used in [62, 80–82]. The high frequency voltage signal generated by a drive causes a high-frequency current to flow which can be sensed by the current sensors. This high frequency current contains two components

- The positive sequence component which is dependent on the machine inductance and resistance and does not contain any position information.
- The negative sequence component which is dependent on the machine saliency, and contains a harmonic of the machine position information.

This negative sequency signal after separation can be processed using demodulator to extract the position signal. [83] discussed compensating for delays due to filters in demodulation. The demodulation depends on the type of injection used. There are two methods of implementing the high frequency injection:

- Rotating injection [84] : In rotating injection a voltage vector $V_{mag}e^{j\omega_c t}$ is injected in the machine stationary reference frame to generate the positive and negative sequence currents mentioned above. This method creates current disturbances in the d and q-axis. This creates torque ripple due the interaction of the high frequency current in the q-axis and the machine rotor flux. For most applications this ripple is at a very high frequency and small enough that it does not create any problems.

- Pulsating Injection or Square Wave injection [85]: In pulsating injection a voltage $V_{mag}cos(\omega_c t)$ is injected in the machine estimated d-axis. This generates corresponding current in the machine q-axis which contains the position information. The error current magnitude is minimized to get an accurate estimate of the reference frame.

A comparative analysis of the performance of pulsating and rotating injection based self-sensing has been performed in [86]. The rotor position information available from the machine saliency is highly dependent on the machine design. The modifications to the machine design which can make self-sensing easier have been discussed in [87]. The position information can contain additional harmonics of the position signal depending on machine properties such as saturation based saliencies[62, 88]. Eddy current based saturation has also been shown to provide position information in surface permanent magnet machine which contains negligible saliency [89].

The low speed and high speed methods are usually combined to provide a wide speed range solution for self-sensing operation. Multiple solutions have been proposed for combining the methods [90–94].

4.2.3 Self-Sensing for Wound Field Machines

The combination of back-emf based methods and injection based methods provide a wide speed range of position and speed estimates. These methods can be used for machine employing permanent magnets as well as wound field machines. Along with the back-emf and injection based methods previously described, wound field machines provide an additional access point to the rotor position information from the machine field winding[95, 96]. The high frequency signal can be injected on the rotor side and the resultant three phase currents induced in the machine stator contain position information based on the spatial alignment between the stator and the rotor. A method of minimizing the hardware complexity of the rotor power supply for such a high frequency based method is to use the current ripple produced from a DC-DC converter used to excite the field winding [97]. The interaction between the rotor and stator windings is very similar to the principle employed in a resolver where the orientation of high frequency excited coil with two other orthogonal coils provides position measurement.

The work in [98] also investigates self-sensing using injection on the rotor. A high frequency sinusoidal signal is injected on the rotor terminals and the resultant signal in the stator winding is demodulated to obtain rotor position.

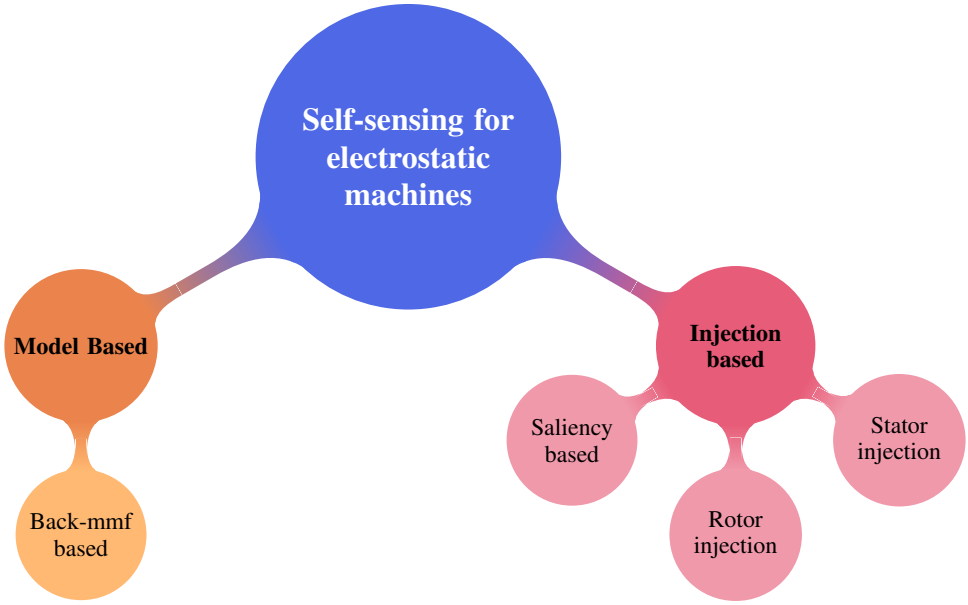

Figure 4.2, Self-sensing methodologies for separately excited electrostatic machines

4.3 Self-Sensing for Separately Excited Electrostatic Machines

Fig. 4.2 illustrates the different methodologies that can be potentially implemented for estimation of rotor position of electrostatic machines.

4.3.1 Back-MMF based position sensing

Similar to back-emf in electromagnetic machines, the SEM rotor charge creates a back-mmf (a back-current) which is dependent on the speed and separate excitation. This speed-dependent back-mmf can provide rotor position information when the machine is rotating. The back-mmf signal properties along with the observer structure need to be investigated for extracting position information from the back-mmf. The back-mmf of the electrostatic machine can be tracked using voltage observers to extract position information. This method is limited to higher speeds because the signal-to-noise ratio of

the position signal is inherently speed dependent.

4.3.2 Signal injection based position sensing

Injection based self-sensing methods are targeted towards the zero and low speed operating regions. The separate excitation in the machine provides multiple methods for estimation of rotor position. Along with the conventional injection based sensing relying on machine saliencies for providing position information, the separate excitation provides two additional methods involving injecting a high frequency signal on either the rotor terminals and measuring the signal on the stator, or injection on the stator terminals and measuring the resultant signal on rotor.

4.3.2.1 Saliency based position sensing

A high frequency signal injected in the stator can be used to excite the machine saliency to provide position information. Injection based methods for electromagnetic machines rely on machine non-linearities for estimating position. The saliency of the SEM is less than 3% which makes extracting the position information from the signal challenging. The saliency based method can be applicable to variable elastance type machines demonstrated in [15, 21] which exhibit a significant saliency.

4.3.2.2 Stator Injection

A signal can be injected on the stator and measured on the rotor. This method requires access to rotor terminal voltage through slip rings. The major advantage of this method is that it does not require any additional hardware for signal measurement. The position information present on the DC field voltage can be separated from the DC content using a high pass filter in the digital controller.

4.3.2.3 Rotor Injection

A high frequency signal can be injected on rotor terminals via the rotor excitation controller. This signal directly couples with the stator and can be demodulated like a resolver signal to provide position information. The signal injection on the rotor can be achieved by a DC-DC converter with the ripple content on the DC converter acting as the injected signal.

4.4 Back-MMF Based Self-Sensing

The back-mmf or 'back-current', which is the result of the motion of the charge on the machine rotor. The back-mmf signal is speed dependent and has been extensively studied in electromagnetic machines for providing a position estimate for closed loop control at medium to high speeds. This section evaluates the SEM for back-mmf based parameter estimation.

The machine model for a non-salient SEM in the stationary reference frame is given in 4.2. The dq-axis stationary reference frame back-mmf is shown in eq. 4.2 and 4.3. The stationary reference frame is chosen to avoid any frame dependent cross-coupling arising out of a reference frame transform. The back-mmf M given in (4.4)-(4.5) and is speed and field voltage dependent. The back-mmf signal can be extracted by implementing a voltage observer with a commanded current feedforward. This observer shown in Fig. 4.3 estimates the back-mmf within its bandwidth and acts as a back-mmf state filter. The observer tuning is based on the maximum frequency that the system will be operated at to avoid undesirable lags. This method is limited to medium and high speeds as the back-mmf is proportional to the speed and will not give a very accurate estimate at low speeds. Figure 4.5 shows the block diagram of the controller implementation for back-mmf based self-sensing. The tuning for the voltage observer is given in (4.6) and

(4.7) where f_p and f_i are the proportional and the integral frequencies for the observer. The voltage observer performance is directly dependent on the accuracy of the machine parameters. The back-mmf extracted from the observer can be significantly inaccurate due to parameter estimation errors. A basic signal injection type method is used for understanding the effect of inverter non-linearities for tuning the back-mmf observer parameters. The details of the effect of inverter non-linearities on the parameters is detailed in Appendix A.

$$i^s_{qs} = \frac{V^s_{qs}}{R_s} + sV^e_{qs}C_s - \omega_e C_m V_{fd} cos(\theta_e) \tag{4.2}$$

$$i^s_{ds} = \frac{V^s_{ds}}{R_s} + sV^e_{ds}C_s + \omega_e C_m V_{fd} sin(\theta_e) \tag{4.3}$$

$$M^s_{qs} = -\omega_e C_m V_{fd} cos(\theta_e) \tag{4.4}$$

$$M^s_{ds} = \omega_e C_m V_{fd} sin(\theta_e) \tag{4.5}$$

$$k_{po} = 2\pi f_p \hat{C}_s \tag{4.6}$$

$$k_{io} = 2\pi f_i k_{po} \tag{4.7}$$

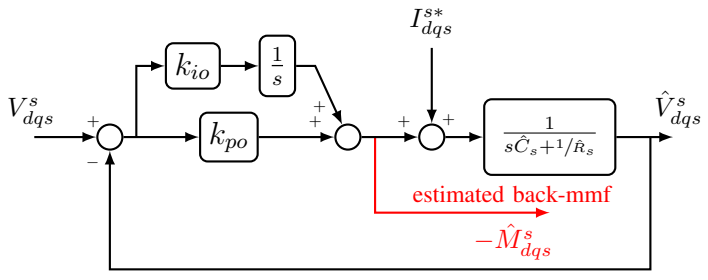

Figure 4.3, Back-mmf state filter shown in the stationary reference frame

The arc-tangent of the estimated back-mmf signal provides the position estimate. This method is sensitive to noise on the input signals. The back-mmf signal after normalization can be coupled with a back-mmf tracking observer as shown in Fig. 4.4 for estimating the position and rotor speed [71]. The observer with the torque feedforward provides a zero-lag estimate of the position signal.

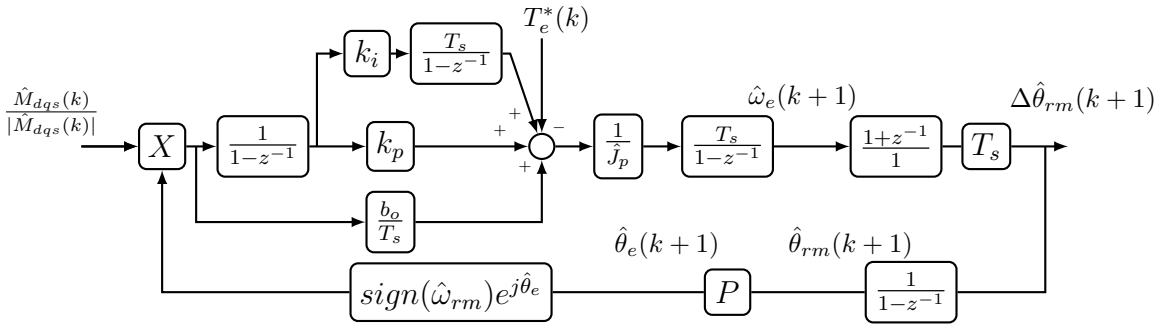

Figure 4.4, Position tracking observer shown in discrete time for extraction of position signal using back-mmf signals

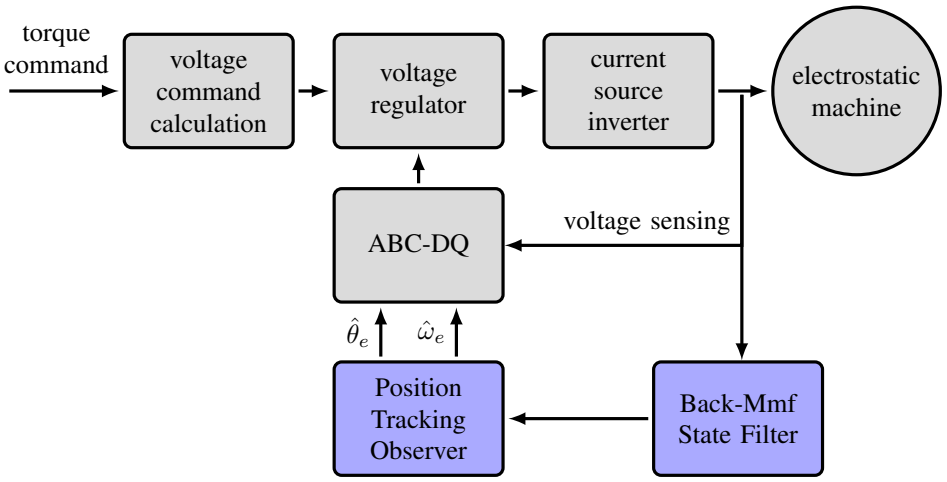

Figure 4.5, Block diagram of position estimation using back-mmf self-sensing

4.4.1 Experimental Verification

Back-mmf based self-sensing is implemented on the SEM dyno test stand. The machine is held at a constant speed by the dyno motor and the back-mmf is estimated with an applied field of 2.5 kV. Fig. 4.6 shows the estimated dq-axis back-mmf in the stationary reference frame at two different speeds. The magnitude of the back-mmf signal matches the expected magnitude shown in (4.4)-(4.5).

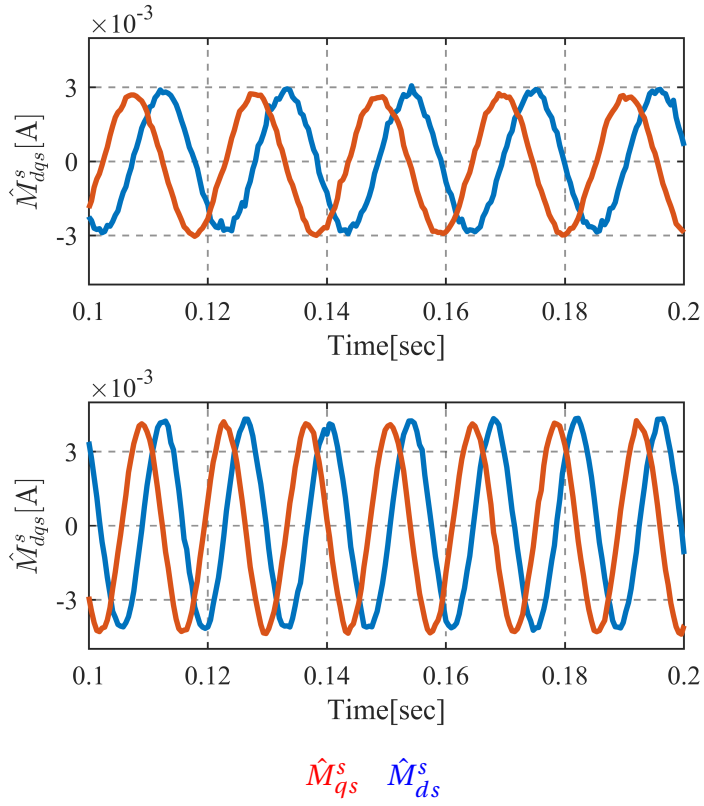

Figure 4.6, Estimated back-mmf using back-mmf state filter at V^e_{qs} =0 V, I_{bus} =100 mA, V_{fd} = 2.5kV, with machine held at constant speed of (top) 60 rpm (96 Hz) and (bottom) 90 rpm (144 Hz)

Using the back-mmf signals seen in Fig. 4.6, the position is estimated using the position tracking observer shown in Fig. 4.4. The estimated position tracks the measured position as seen in Fig. 4.7. The estimation error which is proportional to the speed of

the rotor is the phase delay in the position estimate due to the bandwidth of the back-mmf state filter which with a 500 Hz tuning, is still relatively close to the fundamental frequency of 150 Hz.

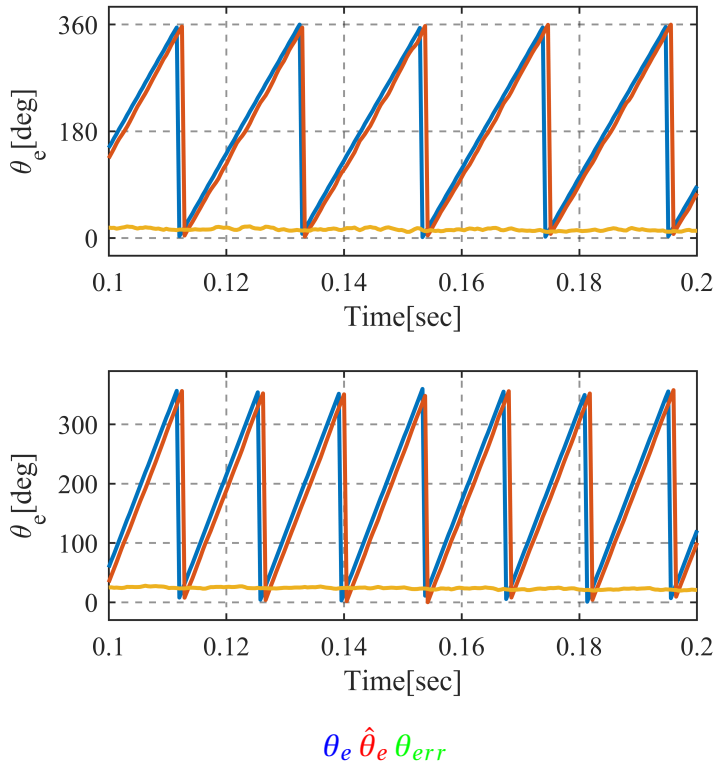

Figure 4.7, Measured and estimated speed using using back-mmf based self-sensing at V_{qs}^{e} =0 V, I_{bus} =100 mA, V_{fd} = 2.5kV, with machine held at constant speed of (top) 60 rpm (96 Hz) and (bottom) 90 rpm (144 Hz)

The back-mmf signals seen in Fig. 4.6 are less than 5% of the dc bus current. It is therefore necessary to understand the effect of inverter harmonics on the back-mmf estimation which are not seen in Fig. 4.6 and Fig. 4.7 due to a zero voltage command. To investigate the effects of the inverter which would arise in a torque control operation of the machine, varying q-axis voltage commands of 0, 250 V and 500 V are provided to the voltage regulator and the estimated back-mmf is observed as seen in Fig. 4.8. The rotor excitation is held at 2.5 kV for these tests. The measured and estimated position is

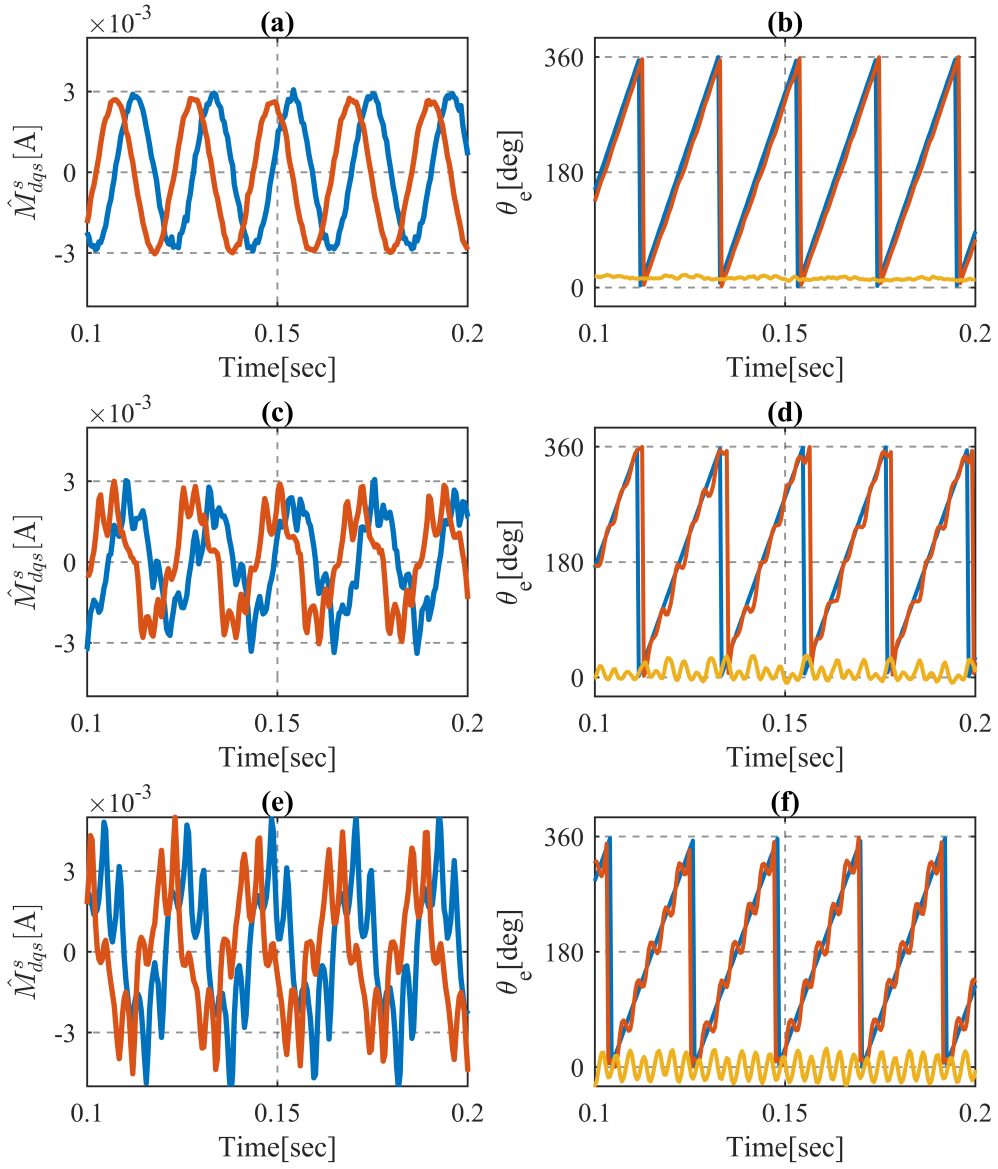

Figure 4.8, Effect of inverter harmonics on back-mmf based position estimation showing estimated q-axis back-mmf with the machine held at a constant speed of 60 rpm (96 Hz) and rotor voltage V_{fd} = 2.5 kV at inverter voltage top: V^e_{qs} =0 V, center: V^e_{qs} =250 V, bottom: V^e_{qs} =500 V

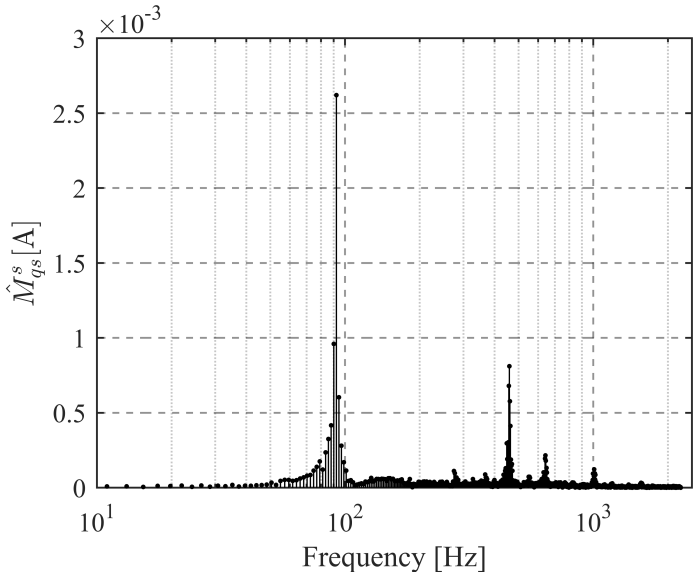

Figure 4.9, Harmonic spectrum of estimated back-mmf with V^e_{qs} =500 V, I_{bus} =100 mA, V_{fd} = 2.5kV, with machine held at constant speed of 60 rpm (96 Hz)

also observed. It is clear from the signals that the inverter injects a significant amount of harmonic content due to switch non-liniearities. An fft of the back-mmf signal when the 500 V command is provided is seen in Fig. 4.9.

4.4.1.1 Closed loop torque modulation

The back-mmf based position signals are used for the dq-transformation and used to modulate machine terminal voltage. Fig. 4.10 shows the measured torque with the machine rotated at a constant speed and a q-axis voltage of 500 V and 1 kV which corresponds to a 0.4 Nm and 0.85 Nm torque at a rotor voltage of 2.5 kV. The scale of the measured torque is chosen such that it corresponds to the equivalent q-axis voltage signal. The measured torque is seen to match the commanded and measured voltage signals.

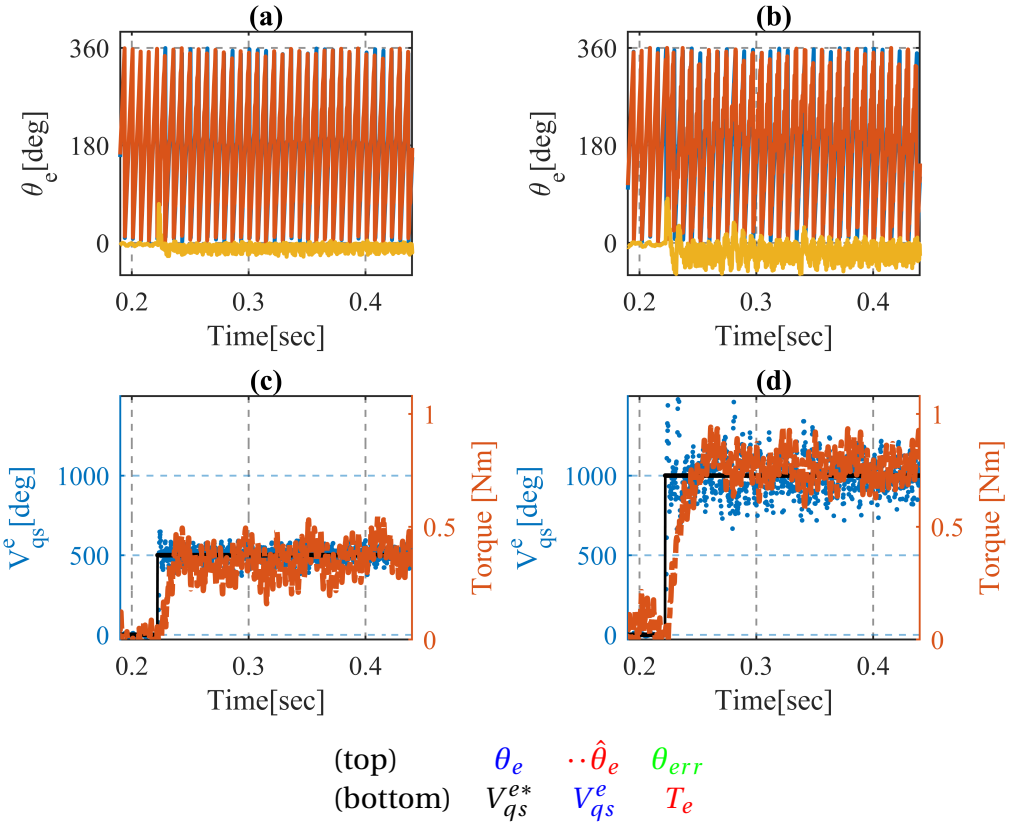

Figure 4.10, Closed loop torque control using back-mmf based self-sensing showing (top) the measured, estimated position and the position estimation error and (bottom) the q-axis voltage command, response and measured torque with the machine rotating at a constant speed of 60rpm (96Hz) and a field voltage of 2.5 kV

4.4.2 Back-MMF sensing limitations for SEM

4.4.3 Inverter Harmonics

As seen in Fig. 4.8 and Fig. 4.10 there is a significant presence of an undesirable harmonic content on the estimated position signal. This content cannot be filtered out completely due to limitations on the observer bandwidth. There can be several approaches to reducing the effect of the inverter non-liinearities on the estimated signal:

- A lower bus current can be used for driving the CSI. The lower bus when running

at a relatively high modulation ratio would be able to provide a better estimate of the back-mmf signal with reduced harmonic content. However this approach comes with a challenge of reduced stored energy in the dc bus which can place limitation on dynamic performance of the machine. Along with reduced stored energy, it becomes challenging to implement a closed loop current source which can measure milliamperes of current and provide a high bandwidth regulation.

- Another approach would be to implement harmonics filters to decouple the drive harmonic content from the back-mmf estimate for a cleaner signal.

4.4.4 SEM Leakage Capacitance

Most permanent magnet machines have a relatively low voltage drop across the leakage inductance when compared with the back-emf when running at high speeds. The SEM however has synchronous capacitance of 13.8 nF which is more than 6 times higher than the mutual capacitance C_{md} of 2 nF. When excited with the same voltage on the stator and the rotor, the resultant back-mmf signal is 6 times lower than the leakage current flowing through the leakage capacitance. This leakage current also restricts the least amount of DC bus current that can be used for the drive for improved back-mmf signals as discussed in Section 4.4.3. This also points to a potentially favourable operating region where the rotor voltage is significantly higher than the stator voltage. Such an operation region which is basically a higher speed, low torque operation of the machine would still provide a reasonably noise-free estimation of the rotor position. Higher torque values requiring higher stator currents would potentially require methodologies to reduce harmonic content as discussed in Section 4.4.3. This also makes the back-mmf self-sensing more suitable at a higher speed.

4.5 High Frequency Signal Injection Based Self-Sensing for SEM

As discussed in Section 4.3, the high frequency injection based sensing for SEM can be approached by injecting either on the stator or on the rotor. The block diagram for the injection on the rotor is shown in Fig. 4.11. A block diagram for the injection on the stator is shown in Fig. 4.12. The SEM includes slip rings on the rotor for providing the rotor excitation. The slip ring voltage is available for measurement. This work takes the approach of injecting a high frequency signal on the stator. The DC excitation can then be provided by DC-DC converters without the need to develop additional hardware with the capability to inject high frequency signals on the rotor side.

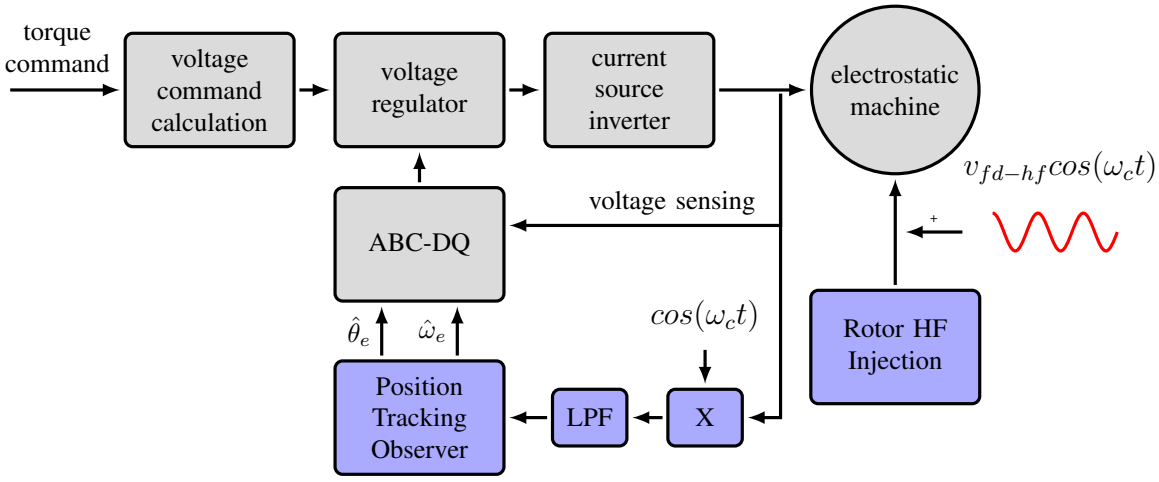

Figure 4.11, Block diagram of injection based self-sensing with high frequency signal injected on the rotor and resulting signal measured on the stator

4.5.1 Electrostatic Motor Model

The dq-axis equivalent circuit diagram shown in the synchronous reference frame is repeated over here for convenience in Fig. 4.13.

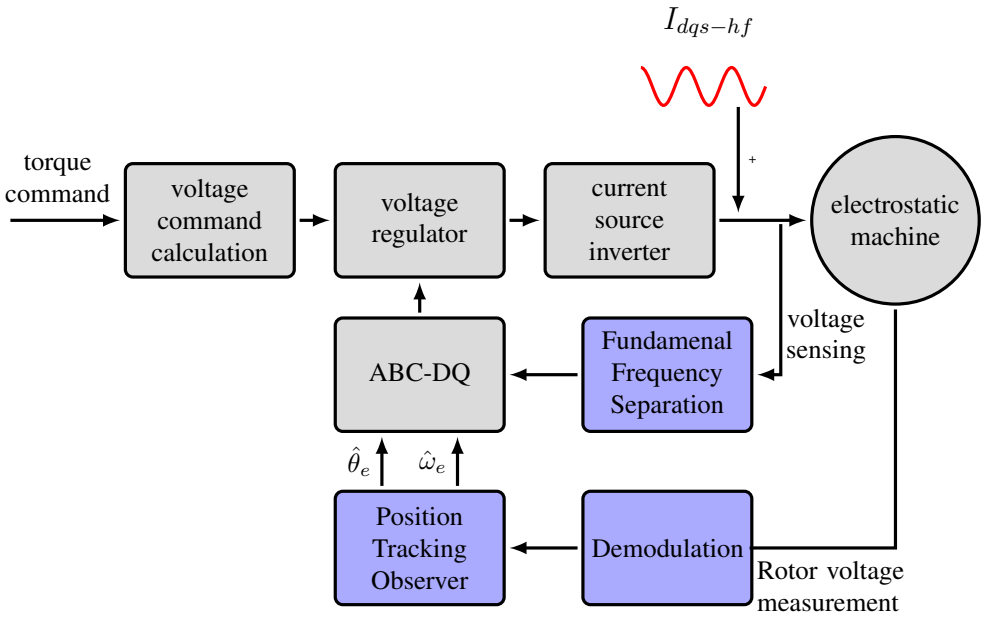

Figure 4.12, Block diagram of injection based self-sensing with high frequency signal injected on the stator and resulting signal measured on the rotor

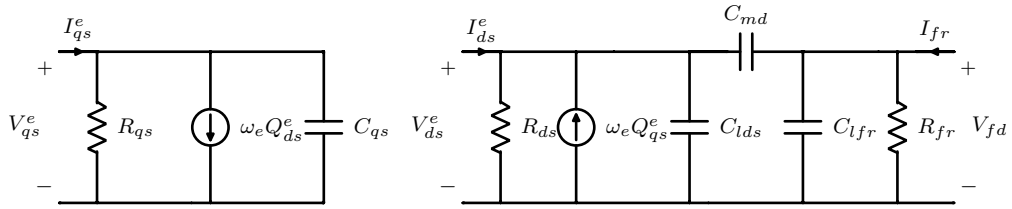

Figure 4.13, Equivalent circuit model of the SEM showing machine q-axis (top) and d-axis (bottom), shown in the synchronous reference frame

It is necessary to investigate the high frequency dynamics of the SEM to develop injection based self-sensing methods for the SEM. The high frequency model of the SEM along with the dynamics of the rotor field in the synchronous reference frame are shown in (4.8). The high frequency model neglects the effect of resistances since the high frequency machine dynamics are dominated by the reactance.

$$\begin{bmatrix} I^e_{qs} \\ I^e_{ds} \\ I_{fd} \end{bmatrix} = \begin{bmatrix} sC_q & 0 & 0 \\ 0 & sC_d & sC_{md} \\ 0 & (3/2)sC_{md} & sC_{fd} \end{bmatrix} \begin{bmatrix} V^e_{qs} \\ V^e_{ds} \\ V_{fd} \end{bmatrix} \tag{4.8}$$

where C_{fd} is the field capacitance given by $C_{md} + C_{lfr}$ shown in Fig. 4.13. Equation 4.8 can be written as (4.9) to show the effect of injected currents in the dq-axis and the rotor field.

$$\begin{bmatrix} sV^e_{qs} \\ sV^e_{ds} \\ sV_{fd} \end{bmatrix} = \begin{bmatrix} \frac{1}{C_q} & 0 & 0 \\ 0 & \frac{C_{fd}}{C_d C_{fd} - {}^2/_3 C^2_{md}} & -\frac{{}^2/_3 C_{md}}{{}^2/_3 C_d C_{fr} - C^2_{md}} \\ 0 & -\frac{C_{md}}{{}^2/_3 C_d C_{fd} - C^2_{md}} & \frac{C_d}{C_d C_{fd} - {}^2/_3 C^2_{md}} \end{bmatrix} \begin{bmatrix} I^e_{qs} \\ I^e_{ds} \\ I_{fd} \end{bmatrix} \tag{4.9}$$

Isolating the effect of current injection in the d and q-axis from (4.9) on the field, we get (4.10). Equation 4.10 can also be expressed in the stationary reference frame as (4.11).

$$\begin{bmatrix} sV_{fd} \end{bmatrix} = \begin{bmatrix} 0 & -\frac{C_{md}}{{}^2/_3 C_s C_{fd} - C^2_{md}} \end{bmatrix} \begin{bmatrix} I^e_{qs} \\ I^e_{ds} \end{bmatrix} \tag{4.10}$$

$$\begin{bmatrix} sV_{fd} \end{bmatrix} = -\frac{1}{C_{fd-s-hf}} \begin{bmatrix} -sin(\theta_e) & -cos(\theta_e) \end{bmatrix} \begin{bmatrix} I^s_{qs} \\ I^s_{ds} \end{bmatrix} \tag{4.11}$$

where $C_{fd-s-hf} = \frac{C_{md}}{{}^2/_3 C_s C_{fd} - C^2_{md}}$.

For a field voltage measurement (4.11) can be integrated to obtain (4.12).

$$\begin{bmatrix} V_{fd} \end{bmatrix} = -\frac{1}{\omega_e C_{fd-s-hf}} \begin{bmatrix} cos(\theta_e) & -sin(\theta_e) \end{bmatrix} \begin{bmatrix} I^s_{qs} \\ I^s_{ds} \end{bmatrix} \tag{4.12}$$

4.5.2 Rotor position self-sensing

The high frequency machine model identifying the effect of injected currents on the field voltage as given in (4.12) can be used for developing rotor position self-sensing. The

type of carrier signal chosen for the signal injection determines the method of signal demodulation and position estimation. The self-sensing can be achieved by rotating or pulsating injection methods. For this work, a rotating injection based sensing is utilized. The development of the high frequency machine model along with the rotating injection and the subsequent demodulation technique for estimation of the position and speed is detailed below.

A rotating current vector given by (4.13) is injected into the stationary reference frame. The resultant voltage on the rotor can be measured either as a change in the field voltage (4.11) or as the measured field voltage (4.12) for extracting position information. Substituting the injected current vector in the high frequency stationary reference frame model of the SEM, we get (4.14).

$$I^s_{qds} = I_c e^{j\omega_c t} = I_c cos(\omega_c t) + I_c sin(\omega_c t) \tag{4.13}$$

$$V_{fd} = V_{inj}[sin(\theta_e)cos(\theta_r) + cos(\theta_e)sin(\theta_r)] \tag{4.14}$$

where $V_{inj} = -\frac{I_c}{(\omega_e+\omega_c)C_{fd-s-hf}}$.

Equation 4.14 can be further simplified to (4.15).

$$V_{fd} = V_{inj}cos((\omega_c + \omega_e)t) \tag{4.15}$$

An experiment to verify the high frequency model is conducted by injecting a high frequency signal in the machine stator with the rotor held at a constant speed using a dyno motor. Figure 4.14 shows the spectrum of the rotor voltage with high frequency current at a frequency f_c = 750 Hz injected in the machine rotating at 20 rpm (f_e = 32 Hz). The field voltage contains the position information at $\omega_c + \omega_e$ at a frequency of 782 Hz which matches the expected frequency in (4.15). It is important to note that the equation

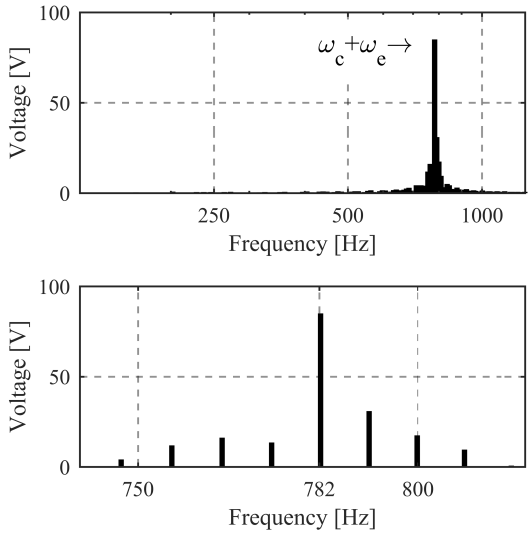

Figure 4.14, Measured spectrum of the voltage signal measured at the rotor terminals showing the (top) full spectrum and (bottom) zoomed in spectrum at ω_e = 32 Hz (20 rpm) and 20 mA carrier current at f_c = 750 Hz under no load and a 3.5 kV DC field voltage removed using high-pass filer placed at 100 Hz

seen in (4.15) describes only the high frequency content of the rotor voltage. In practice, a high pass filter needs to be implemented for removing the DC field excitation from the rotor voltage measurement.

This high frequency signal can then be demodulated to provide the estimated position signal. The signal in (4.15) is multiplied by the sine and cosine of the injection signal angle to obtain the sine and cosine of the position signal along with the second harmonic of the injection frequency as given by (4.16),(4.17). These signals are then filtered to obtain the sine and cosine of the rotor position which along with a position tracking observer provides a zero-lag position estimate. The process of signal demodulation and position extraction is detailed in Fig. 4.15.

$$V_{fd}sin((\omega_c)t) = V_{inj}(sin((2\omega_c+\omega_e)t) - sin((\omega_e)t) \tag{4.16}$$

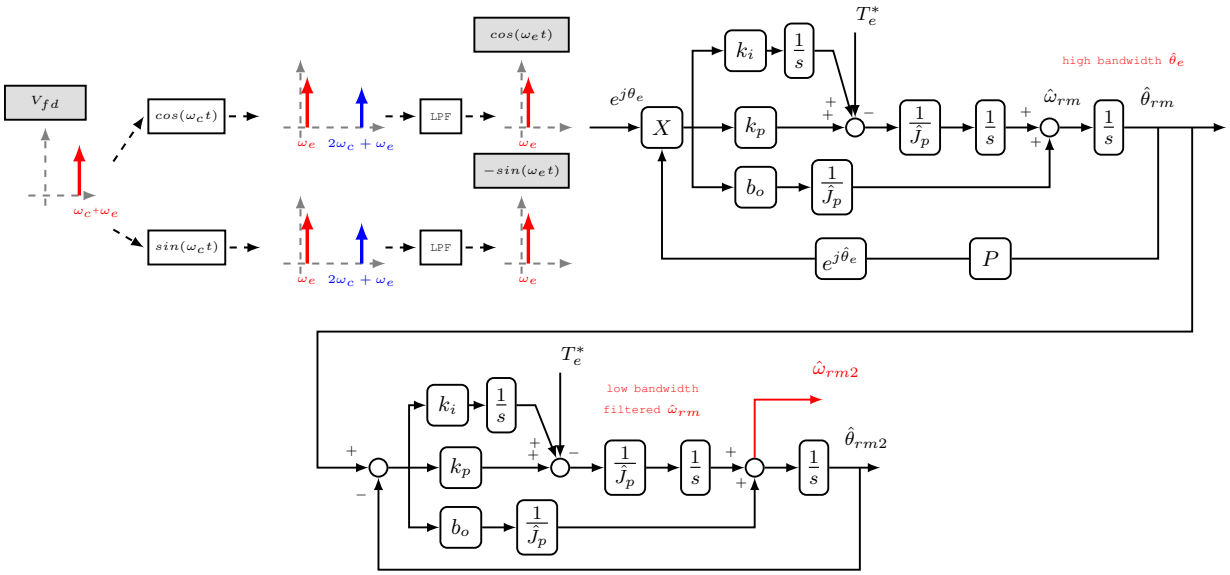

Figure 4.15, Signal demodulation and position tracking observer for extracting rotor position and speed using injection signal based self-sensing.

$$V_{fd}cos((\omega_c)t) = V_{inj}(cos((2\omega_c+\omega_e)t) + cos((\omega_e)t) \tag{4.17}$$

The resulting cosine and sine terms are demodulated using a position tracking observer (PTO) as shown in Fig. 4.15 which provides a zero lag position estimate.

4.5.3 Filter selection for implementing injection based position sensing

As shown in Fig. 4.15, the self-sensing methodology incorporates multiple filters for the signal conditioning. The knowledge of filter placement is essential for understanding and designing the dynamic performance to be achieved from the self-sensing system.

- A high pass filter is required for extracting the injection vector projection on the rotor voltage signal from the DC component. The filter needs to have a high DC rejection as any DC signal content on the high frequency signal will introduce errors

in the position estimation. Another requirement of the filter is to have a low delay at the injection frequency. This is achieved by using a second-order low pass filter. Another method of extracting the signal is to implement an adaptive bandpass filter which moves the pass-band according to the estimated velocity from the position tracking observer.

- Removal of the second harmonic content of the injected signal from the signals to be demodulated requires low pass filters. The main challenge in implementing these filters is to have the low pass filter bandwidth as low as possible to remove any high frequency content but at the same time have minimal delays on the fundamental frequency signal.

4.5.4 Fundamental Voltage Separation

The injected signal creates a high frequency disturbance voltage. Even though the frequency of the injection is much higher than the bandwidth of the voltage regulator, the voltage regulator still responds to the injected current as a disturbance. The carrier signal is separated from the fundamental voltage signal using a synchronous reference frame band-stop filter. The dynamic analysis of methods for removing high frequency content from fundamental frequency control signals is presented in [80, 82].

4.5.5 Experimental verification of injection based self-sensing for SEM

The experimental implementation of the injection based self-sensing is shown in Fig. 4.16. The system is implemented on the SEM dyno previously described in Chapter 3. The system implementation includes a speed regulator which can use the estimation position signal for controlling machine rotor speed. The estimation position from the self-sensing

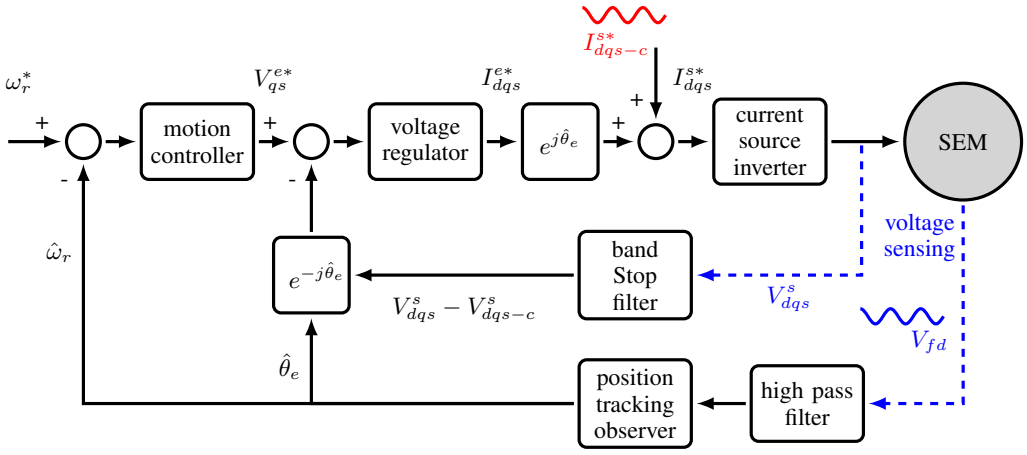

Figure 4.16, Block diagram of system implementation of closed loop speed control of SEM using injection based self-sensing

Table 4.2, Motion controller and position tracking observer eigen values, and filter bandwidths

Controller/Observer	EVs [Hz]
Motion Controller	6, 0.5, 0.1
PTO	12.5, 1, 0.1
Speed Estimation PTO	8, 0.75, 0.5
Filter	ω_b [Hz]
LPF	150
HPF	100

algorithm is used for the dq-transform and achieving charge-oriented control. The high frequency signal is a rotating current command which is added to the inverter reference current command.

4.5.6 Steady state signal injection based self-sensing

Figure 4.17 and Fig. 4.19 show the estimated and measured position with the machine held at a constant speed of 20 rpm by the dyno drive operating in speed control. Figure

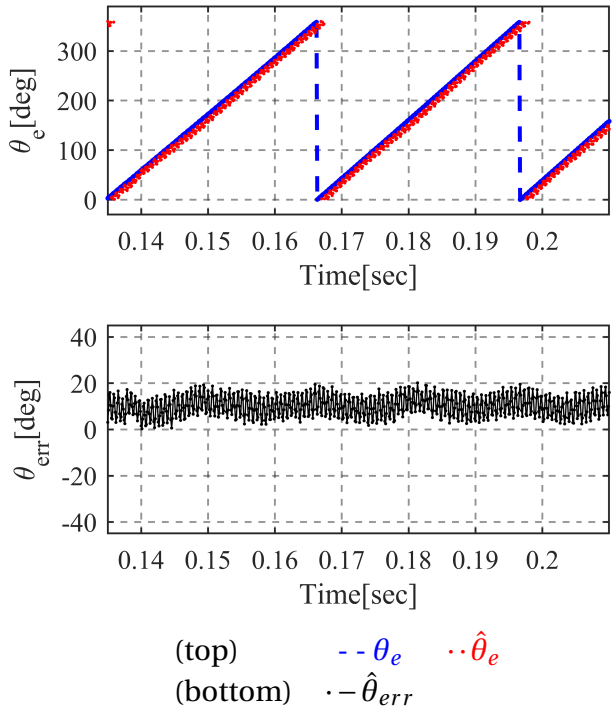

Figure 4.17, Measured and estimated electrical position with V_{qs}^{e} = 0 V with machine rotating at 20 rpm (32 Hz) with an injected signal of 30 mA

4.17 shows that the position tracking observer tracks the position with very low estimation error ($\theta_e - \hat{\theta}_e$). Figure 4.19 shows the position tracking with a commanded voltage V_{qs}^{e} = 500 V . The additional voltage at the fundamental frequency increases the signal content on the rotor field which increases rotor position estimation error.

The mechanical angle estimate and position estimation error for the experiment shown in Fig. 4.17 is shown in Fig. 4.18.

The mechanical angle estimate and position estimation error for the experiment shown in Fig. 4.19 is shown in Fig. 4.20. Figure 4.18 and Fig. 4.20 both demonstrate an estimated mechanical error in the order of 0.25 degrees which highlights the very high position estimation accuracy that can be achieved by the high pole count of the SEM.

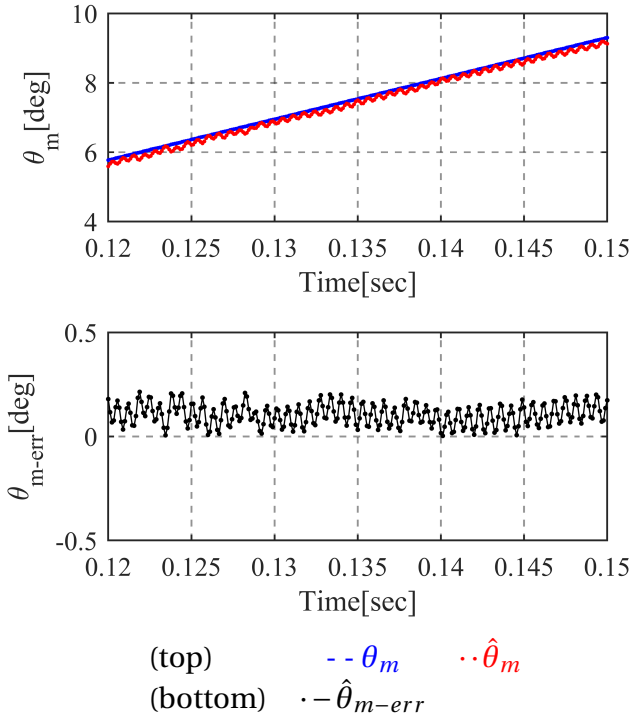

Figure 4.18, Measured and estimated mechanical position with V_{qs}^{e} = 0 V with machine rotating at 20 rpm (32 Hz) with an injected signal of 30 mA

4.5.7 Closed Loop Speed Control

The position information extracted from the injected signal is used for controlling the machine torque angle. Along with providing position information, the PTO in Fig. 4.15 provides a mechanical speed estimate. This speed estimate is noisy due to the high observer bandwidth required for tracking the position signal. The position signal obtained from the PTO is cascaded with a lower bandwidth position observer as shown in Fig. 4.15 [94] for obtaining a filtered estimate of the position signal and used for closing a speed loop on the rotor speed using a motion controller. The motion controller gains are given in Table 4.2. Figure 4.21 shows the machine following a speed profile which has a triangle command of 15 rpm on a offset command of 25 rpm. The response of the controller using the measured position and speed signal 4.21a) is comparable with the controller using

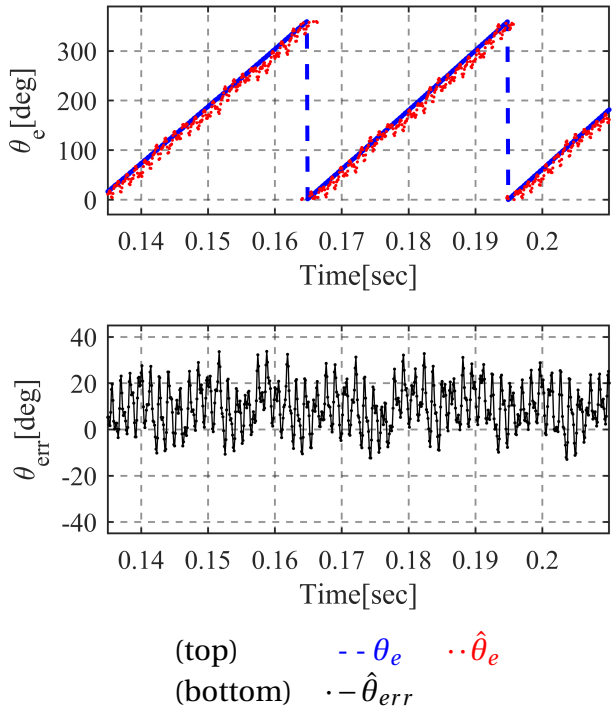

Figure 4.19, Measured and estimated electrical position with V_{qs}^{e} = 500 V with machine rotating at 20 rpm (32 Hz) with an injected signal of 30 mA

the estimated position and speed signal Fig. 4.21b). The speed estimation error $(\omega_r - \hat{\omega}_r)$ over the speed profile is very low.

The bandwidth of the motion controller in both the tests is kept the same for a performance comparison. The bandwidth of the motion controller is limited by the bandwidth of the observer for estimating rotor speed. This bandwidth is lower compared to bandwidths achieved using encoder feedback. This causes a reduction in the dynamic response of the motion controller. The noise content on the speed estimate can be reduced by decoupling system non-linearities such as inverter harmonics and enhanced filtering which can allow higher bandwidths on the speed estimate.

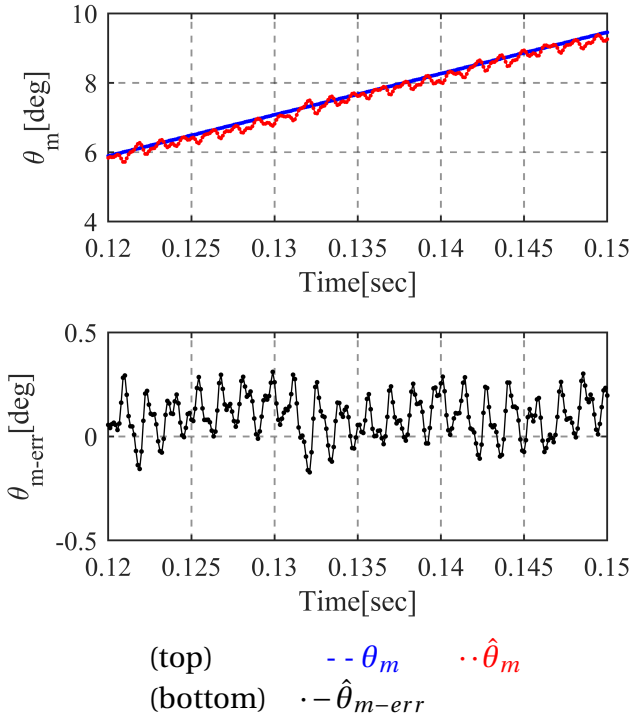

Figure 4.20, Measured and estimated mechanical position with V_{qs}^{e} = 500 V with machine rotating at 20 rpm (32 Hz) with an injected signal of 30 mA.

4.5.8 Filter frequency separation

High frequency based self-sensing for electromagnetic machines typically allows a significantly high separation between the injection frequency and the fundamental electrical frequency allowing the placement of low pass filters for demodulation to be relatively easy. A rotor speed of 60 rpm for an 8 pole machine is 8 Hz which is significantly lower than typical injection frequencies of 500-1000 Hz achieved with inverters below a 10 kHz switch frequency. The SEM on the other hand has a pole count of 96 which poses some challenges in placing the low pass filter bandwidth. A rotor speed of 60 rpm translates to a fundamental frequency of 96 Hz electrical. Such a high frequency when passed through a low pass filter to remove the high frequency content at $2f_c$ with f_c =750 Hz creates a significant phase delay. The phase delay needs to be compensated for improving the

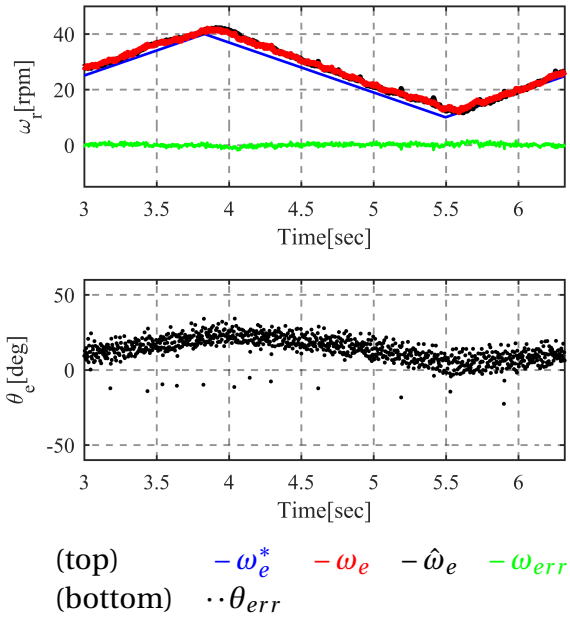

(a)

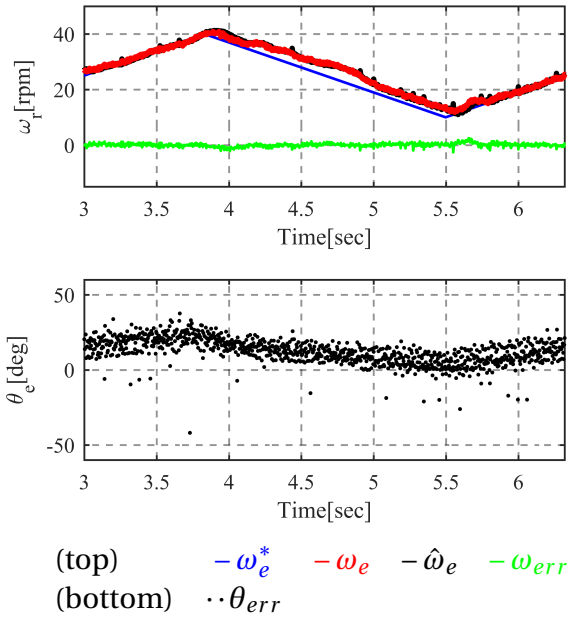

(b)

Figure 4.21, Closed loop speed control using a) encoder feedback and b) Estimated position with an injected signal of 30 mA with V_{fd} = 2.5 kV

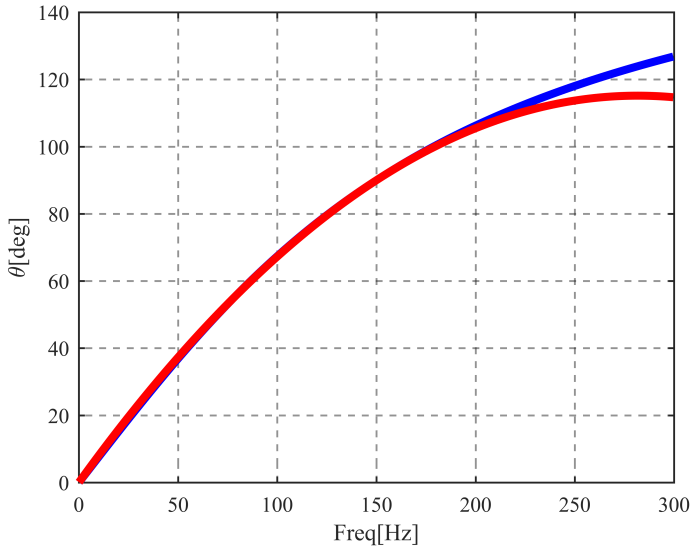

–actual delay, –computed delay

Figure 4.22, Actual and computed delay using 4.19

phase delay observed at higher rotor speeds. The phase delay can be reduced by compensating for the phase delay based on the estimated rotor speed. The delay can also be removed by implementing a variable frequency band-pass filter based on the rotor speed. However this is more sensitive to the estimation accuracy and the bandwidth of the speed estimation observer.

$$\theta_{delay} = tan^{-1}(\frac{\omega_e}{\omega_{filter}}) \tag{4.18}$$

$$tan^{-1}(x) = \frac{\pi}{4}x + 0.273x(1-|x|) \tag{4.19}$$

where $-1 < x < 1$

The low pass filter for the signal demodulation adds the most significant delay due to the low filter frequency . The delay added due to two cascaded first order low pass filters is given by (4.18) where ω_{filter} is the bandwidth of the filter. An approximation of the inverse tangent function shown in (4.19) [99] is used for computing the delay

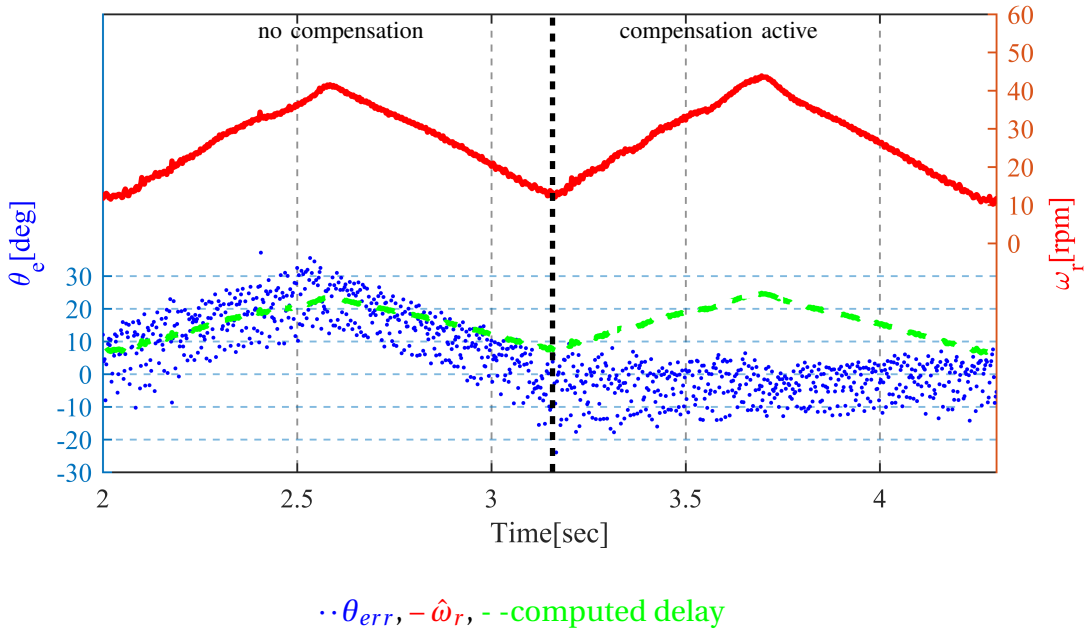

Figure 4.23, Filter phase delay compensation showing improvement in estimated position error with rotor voltage $V_{fd} = 2.5\ kV$

added by the two cascaded filters. The machine is accelerated from zero to 50 rpm with a speed loop using estimated position and speed signal. The position estimation error is measured with and without the phase delay compensation as shown in 4.23. The delay compensation exhibits a significant reduction in position estimation delay. The 10^o(elect) position estimation error obtained by utilizing the compensation technique translates to a mechanical estimation error of 0.1^o(mech), demonstrating the high resolution in the position estimate achievable due to the high pole count of the SEM.

4.6 Saliency based self-sensing

The SEM studied in this research has a saliency of about 3% . This is not sufficient for any appreciable torque production compared to the field torque. However, the saleincy can be tracked to get an estimate of the rotor position. The saliency of the machine capacitance

results in a negative sequence component using an injected signal.

A high frequency current vector is injected in the machine. The resulting voltage is composed of two parts: the positive sequence component which is based on the average capacitance of the machine and the negative sequence which contains the secondary harmonic of the machine.

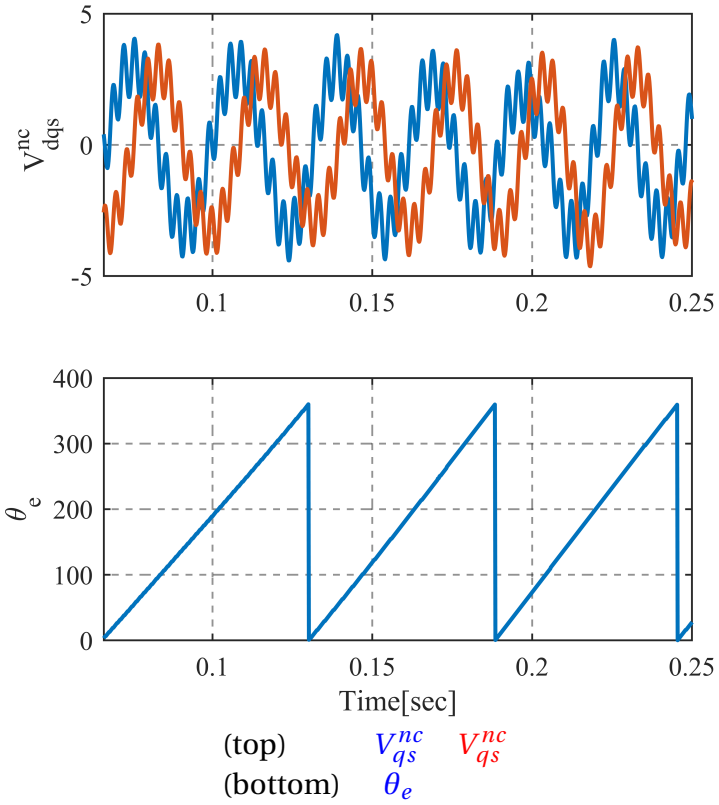

Figure 4.24, Negative sequency component of the injection frequency voltage (top) and measured electrical position(bottom) with the machine held a constant speed of 12rpm (19.2 Hz) with an injected signal of 10 mA at a frequency of 450 Hz

Fig. 4.24 shows the negative sequence component of the voltage signal due to the injected signal with and without load. It can be seen that a considerable amount of current needs to be injected to generate significant voltage which can be tracked. The rotor position signal is tracked from the negative sequence voltage using the observer

shown in Fig. 4.25.

The SEM in this work exhibits a very low saliency (<3%). This poses a challenge when extracting the negative sequence signal which contains the position information. The major challenge lies in the limited resolution of voltage sensors. With a resolution of approximately 2%bit, even a 5-10V signal provides only a few bits of position information. There has been prior work on extracting position information from low-saliency machines [89]. This however, requires a significantly high injection signal for getting a significant second harmonic signal.

A major use of the saliency seen in the SEM can be for using the SEM with a low resolution position sensor. The saliency based estimate can provide the required calibration signal for aligning the machine at standstill. The objective of this section is to identify the viability of saliency based self-sensing in electrostatic machines. The almost negligible saturation for the SEM demonstrated in [2] can prove to be a significant advantage for saliency based self-sensing if future machine designs incorporate a salient pole design.

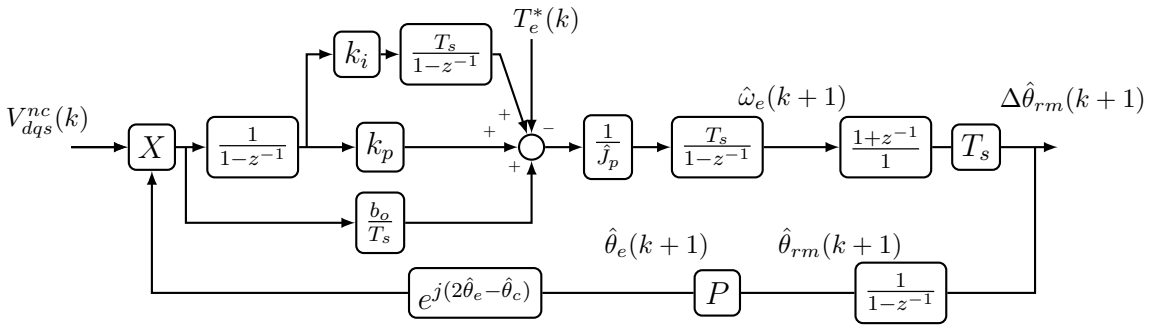

Figure 4.25, Saliency tracking observer to estimate position based on saliency based self-sensing

4.7 Wide Operating Range Self-Sensing

The zero to low speed injection based self-sensing and the medium to high speed back-mmf based self-sensing are combined in this section to provide a continuous self-sensing operation of the SEM. The two methods are combined using a switch which changes the input of the position tracking observer. Figure 4.26 shows a block diagram of the two methods with a switch for method selection. The back-mmf state filter is enabled when the estimated speed reaches 90% of the transition speed. This helps the estimator converge to a speed value before the algorithms is switched. The challenge of a 'bumpless' transfer between the two methods is approached by analyzing the estimation phase difference. The signal phase for the injection based method and back-mmf sensing based method is selected such that the phase lag is the same at the point the algorithms transition. This reduces the transient during the change in two methods.

Figure 4.27 shows the measured position and speed when the sensing algorithm transitions from injection based self-sensing to back-mmf bsaed self-sensing at a speed

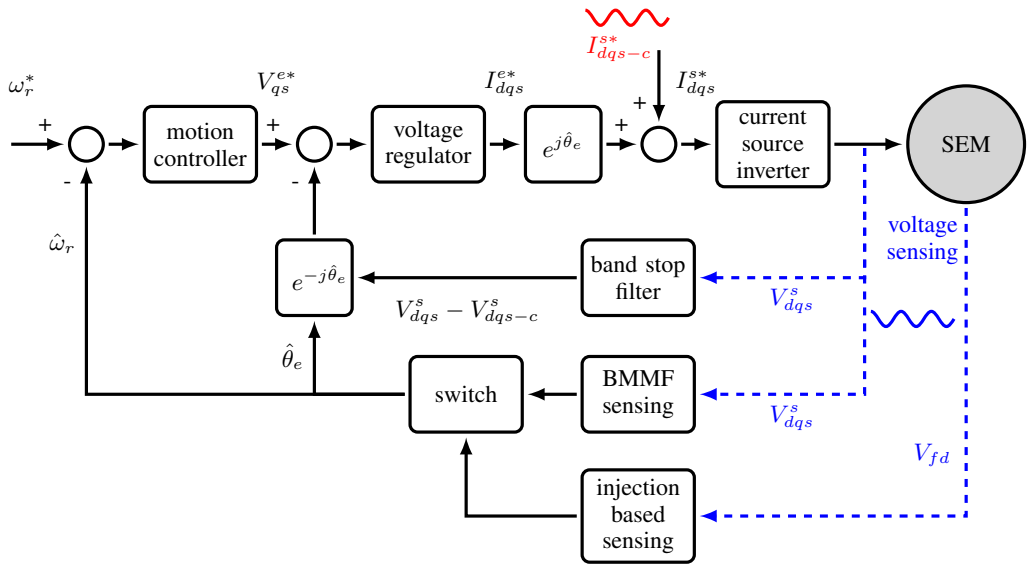

Figure 4.26, Block diagram of system implementation of wide operating range self-sensing

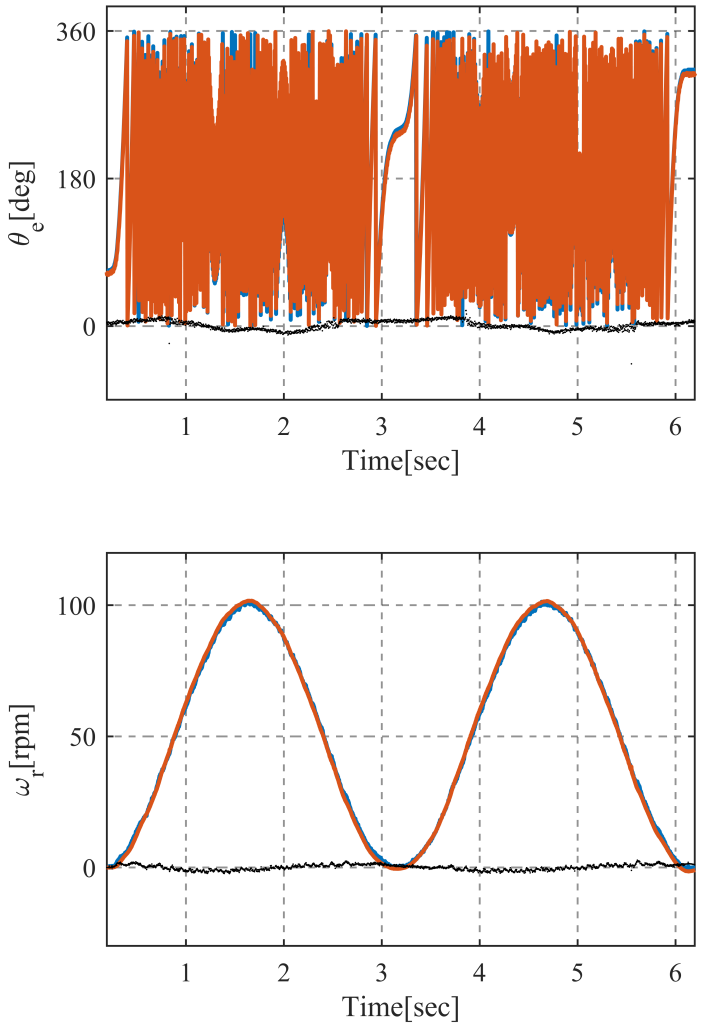

(top)θ_e, $\hat{\theta}_e$, $\hat{\theta}_{err}$, (bottom) ω_r, $\hat{\omega}_r$, $\hat{\omega}_{r-err}$

Figure 4.27, Rotor position estimation over a wide speed range using injection based self-sensing below 45 rpm and using back-mmf based self-sensing at high speed with an injection current of 20mA at f_c = 750 Hz

of 50 rpm (80 Hz). The system provides a smooth transition between the low speed and high speed self-sensing. The phase lag for both methods at the transition frequency is set to the same value which makes the transition between the two methods smooth.

4.8 Self-Sensing Implementation Challenges

4.8.1 Voltage sensor resolution

The closed loop voltage control needs the analog-to-digital converter to be scaled according to the maximum possible voltage signals with overhead. For a 7 kV line - line peak voltage while using the on-chip 12-bit ADC on the MCU used for the drive implementation, we get approximately $2^{V}/_{bit}$ resolution. While this is acceptable for closing the loop on the voltage, the resolution limits the performance of the self-sensing due to the few bits of measured voltage at the carrier frequency. The sensing resolution is improved by increasing the injected signal magnitude. Self-sensing operation at lower injected currents can be improved by using higher resolution ADCs or implementing a fundamental current observer as shown in [82].

4.8.2 Inverter Harmonic Content

The effect of inverter harmonics was very obvious on the position accuracy for both the back-emf based sensing and injection based methods. A detailed analysis of the inverter non-linearities is required for pushing the bandwidths of the self-sensing system higher.

4.9 Summary

This chapter investigates rotor position self-sensing for the SEM. Back-mmf and signal injection based self-sensing is experimentally demonstrated using the SEM and a CSI based drive. An estimation error of 0.25 mechanical radians is demonstrated for the signal injection based self-sensing. A methodology to compensate for the phase lags arrising out of high-pole counts is demonstrated to significantly improve self-sensing performance. A wide-speed range self-sensing algorithm which combines back-mmf and signal injection self-sensing is implemented to provide an accurate position and speed estimation over a zero to 100rpm speed range. Limitations of each self-sensing methodology specific to the SEM design are discussed.

CHAPTER 5

Conclusions, Contributions and Recommended Future Work

The aim of this work is to firmly establish the fundamental drive control techniques of synchronous electrostatic machines spanning a) Drive topology selection from a control perspective, b) Torque modulation using complex vector voltage regulation and c) Self-sensing techniques for position sensor replacement. Contributions towards these thrusts are presented and recommended future work is identified.

5.1 Conclusions

5.1.1 Drive Development and Voltage Control of CSI

- A Current Source Inverter is the ideal drive topology for controlling an electrostatic machine.
- Ampere-seconds (charge) sourced by a CSI can be used to control terminal voltage

of an electrostatic machine similar to volt-seconds sourced by a VSI to control current through an electromagnetic machine.

- A voltage regulator implemented with a CSI connected to a capacitive load exhibits the same approximately first-order dynamics seen in a current regulated VSI with an inductive load.
- A complex vector synchronous frame PI voltage regulator implemented with a CSI provides high-bandwidth output voltage regulation.
- Different power electronics topologies with a stiff current source can be used for powering a capacitive machine.

5.1.2 Electrostatic Machine Control

- The duality between electromagnetic and electrostatic machine dynamics can be used for developing drive systems and control methods.
- Charge oriented control can be used to independently control the torque and field in an electrostatic machine.
- The high pole count of the machine can cause position feedback delays which need to be compensated for achieving accurate reference frame transform.

5.1.3 Self-Sensing

The SEM presents some unique challenges for self-sensing due to the significantly high pole count which is an order of magnitude higher than typical 2-8 pole machines. The high leakage exhibited by the machine also creates challenges particularly for back-mmf based self-sensing due to the significantly low back-mmf signal to leakage current ratio.

- Rotor position self-sensing is of particular importance for an SEM based system due to the high pole count.
- Back-mmf based self-sensing is significantly dependent on field voltage level and machine speed due to the high leakage of the machine.
- A separately excited machine offers the field terminals as an additional access point for providing signals which contain rotor position information.
- Injection based self-sensing can be implemented to achieve a high precision position estimate at zero and low speeds.
- Frequency separation for observer tuning and injection signal determination are particularly important for the SEM due to the significantly high pole count.
- Feedback sensor resolution is important when looking at injection based sensing.
- A salient SEM which exhibits negligible saturation can potentially be an attractive candidate for saliency based position self-sensing.

5.2 Contributions

This work is the first demonstration of torque modulation of macro-scale synchronous electrostatic machines using closed loop voltage control. The work establishes a general controller framework which includes torque modulation and rotor position self-sensing along with an investigation of effect of inverter characteristics on the control performance. The contributions in the different aspects of drive development and machine control are summarized as follows.

5.2.1 Drive Development

The details of the drive development are presented in Chapter 2 and [31].

- The duality between electromagnetic and electrostatic systems was explored from the perspective of developing a drive system.
- Control algorithms and drive topology options for an electrostatic machine drive were identified.
- Different power electronics topologies for driving an electrostatic machine were identified.
- Drive topologies were evaluated based on parameters such as availability of hardware, complexity of control and regions of operation.

5.2.2 Voltage Regulation

The details of the complex vector model development along with the voltage regulator design are presented in Chapter 3 and [5, 31, 38].

- Development of a complex vector model of a separately excited synchronous electrostatic machine which can be used for developing control methods.
- Voltage regulation methods for different current-stiff power electronics topologies were proposed.
- The performance of each topology was evaluated and the advantages and limitations of each method were identified.
- A complex vector synchronous frame PI voltage regulator with back-mmf decoupling was proposed for controlling terminal voltage of the SEM.

- Performance metrics comprising of frequency response and dynamic stiffness of the regulator were experimentally verified using a high voltage CSI and the SEM.

5.2.3 Experimental Verification of Voltage Regulation and Torque Response

The CVVR was implemented on a CSI platform for evaluation of the machine torque modulation. The details of the platform and the firmware are presented in Chapter 2, Appendix B and in [5, 38].

- A test stand for evaluating SEM torque modulation was built.
- Drive firmware platform comprising of a medium voltage CSI based on space vector modulation and a high performance current source front-end with closed loop DC current control was developed on a single microcontroller to evaluate the control performance.
- Dynamic stiffness and Frequency Response Function of the CVVR with the SEM was experimentally verified using a CSI drive platform.
- Torque modulation of SEM using the proposed charge-oriented controller and voltage vector regulator was experimentally verified.
- Step torque commands at stall and speed were achieved using the voltage regulation with a response time less than 10 ms.

5.2.4 Electrostatic Machine Self-Sensing

The SEM with its 98 pole rotor, makes the case for self-sensing very strong. A self-sensing framework was developed to allow the complete elimination or use of cheaper encoders.

The work detailing with self-sensing methods is presented in Chapter 4 and [59].

- Self-Sensing methodologies for rotor position estimation from zero to high speeds were evaluated.
- Back-mmf based rotor position self-sensing has been demonstrated for medium and high speeds.
- Injection based self-sensing using rotor voltage measurement at zero and low speeds was experimental demonstrated.
- The high pole count of the SEM was leveraged for demonstrating a mechanical position estimation error of less than 0.25 mechanical degrees.
- Full closed loop voltage and speed control using the estimated position and speed was experimentally demonstrated.
- A compensation method for improving estimate phase lag due to low injection frequency separation was experimentally evaluated.
- A wide speed range algorithm swithching from injection based self-sensing to back-mmf based sensing was demonstrated to provide a continuous position estimate.

5.3 Recomended Future Work

5.3.1 Drive Development

The series-stack based drive used for experimental verification was sufficient for controlling the drive at the expense of high inverter non-linearities and a complex drive structure. The JFET super-cascode based drive [100] promises faster performance. Volt-

age regulation and self-sensing can significantly improve when operated at the higher switch frequency allowed by the JFET based drive.

5.3.2 Drive Integration

There is no framework present for sizing a drive system for the SEM. The energy storage in the DC bus is significantly low when compared with conventional servo drives for electromagnetic machines. This problem is currently circumvented by communication between the front-end and CSI for higher dynamic performance. A broader understanding of the drive design which incorporates the effects of feasible inductor designs, passive component and device losses and machine requirements is required.

5.3.3 Self-Sensing Frequency Separation Investigation

Chapter 4 demonstrated the challenges associated with selecting an injection signal frequency for self-sensing and also highlighted the delays associated with a high fundamental frequency. Further investigations on the choice of injection frequency and its effects on the bandwidth selection and dynamics of filters and observers in the self-sensing system as well as the speed and position loop system needs to be investigated. Further improvements in drive design which allow a higher injection frequency will potentially allow a higher injection frequency to be used.

5.3.4 Feedback System Design

Experiments involving measurement of small voltages for self-sensing and parameter estimation has highlighted the importance of voltage sensor resolution and its effect on control performance. Different methods of implementing the feedback system which can

offer the full range for voltage control and a high-resolution signal for position estimation needs to be investigated.

5.3.5 System Non-Linearity Compensation

A detailed model of non-linearities associated with the inverter switches particularly due to overlap and non-linear switching would significantly aid in improving parameter estimates as well as other observer and feedforward controller systems. The effect of the non-liniearities is particularly important for back-mmf based self-sensing where the estimated position signals were highly influenced by high frequency harmonic content from the inverter.

Bibliography

[1] UN Environment; Global Environment Facility; United for Efficiency (U4E), "Accelerating the Global Adoption of Energy-Efficient Electric Motors and Motor Systems," 2017. [Online]. Available: https://united4efficiency.org/wp-content/uploads/2017/09/U4E-MotorGuide-201709-Final.pdf

[2] B. Ge, "The Modeling, Design and Demonstration of Electrostatic Synchronous Machines," Ph.D. dissertation, University of Wisconsin-Madison, 2018.

[3] S. F. Nagle, C. Livermore, L. G. Frechette, R. Ghodssi, and J. H. Lang, "An electric induction micromotor," *Journal of Microelectromechanical Systems*, vol. 14, no. 5, pp. 1127–1143, 2005.

[4] F. Kimura, A. Yamamoto, and T. Higuchi, "Fpga implementation of a signal synthesizer for driving a high-power electrostatic motor," in *2011 IEEE International Symposium on Industrial Electronics*, June 2011, pp. 1295–1300.

[5] A. N. Ghule, P. Killeen, and D. C. Ludois, "Electrostatic machine drive using complex vector voltage regulation with a current source inverter platform," in *2018 IEEE Energy Conversion Congress and Exposition (ECCE)*, Portland, OR, Sep. 2018, pp. 4570–4576.

[6] S. A. S. Grogan, D. G. Holmes, and B. P. McGrath, "High-Performance Voltage Regulation of Current Source Inverters," *IEEE Transactions on Power Electronics*, vol. 26, no. 9, pp. 2439–2448, 2011.

[7] P. Waide and C. U. Brunner, "Energy-Efficiency Policy Opportunities for Electric Motor-Driven Systems," p. 132, 2011. [Online]. Available: https://www.bbc.com/news/magazine-26687605

[8] "Copper Prices." [Online]. Available: http://www.infomine.com/investment/metal-prices/copper/all/

[9] J. Rowlatt, "Rare earths: neither rare, nor earths," 2014. [Online]. Available: http://www.bbc.com/news/magazine-26687605

[10] C. Bontron, "Rare-earth mining in China comes at a heavy cost for local villages," pp. 5–7, 2012.

[11] J. D. Mcfarland, "On the design of rare-earth-free and reduced rare-earth permanent magnet machines for high-performance traction applications," Ph.D. dissertation, University of Wisconsin-Madison, 2015.

[12] K. Atallah, S. Calverley, R. Clark, J. Rens, and D. Howe, "A New PM Machine Topology for Low-Speed, High-Torque Drives," in *18th International Conference on Electrical Machines*, Vilamoura, 2008, pp. 1–4.

[13] M. Liu, "Cooling design and thermal analysis for dual-stator 6-slot 4-pole flux-switching permanent magnet machine," Master's thesis, University of Wisconsin-Madison, 2017.

[14] "Schnieder Electric, BSH Servo Manual," 2010.

[15] B. Ge, A. N. Ghule, and D. C. Ludois, "Three-Dimensional Printed Fluid-Filled Electrostatic Rotating Machine Designed with Conformal Mapping Methods," *IEEE Transactions on Industry Applications*, vol. 53, no. 5, pp. 4348–4359, 2017.

[16] O. D. Jefimenko, *Electrostatic motors; their history, types, and principles of operation*. Electret Scientific Co., 1973.

[17] P. Krein, "Nonideal Effects in Electrostatic Induction Motors," Ph.D. dissertation, University of Illinois Urbana-Champaign, 1982.

[18] S. F. Bart, T. A. Lober, R. T. Howe, J. H. Lang, and M. F. Schlecht, "Design considerations for micromachined electric actuators," *Sensors and Actuators*, vol. 14, no. 3, pp. 269–292, 1988.

[19] B. Ge and D. C. Ludois, "Design Concepts for a Fluid-Filled Three-Phase Axial-Peg-Style Electrostatic Rotating Machine Utilizing Variable Elastance," *IEEE Transactions on Industry Applications*, vol. 52, no. 3, pp. 2156–2166, 2016.

[20] B. Ge, D. C. Ludois, and A. N. Ghule, "A 3D printed fluid filled variable elastance electrostatic machine optimized with conformal mapping," in *2016 IEEE Energy Conversion Congress and Exposition (ECCE)*, Milwaukee, WI, Sep. 2016, pp. 1–8.

[21] G. Reitz, B. Butrymowicz, J. Reed, B. Ge, and D. C. Ludois, "A switched elastance electrostatic machine constructed from sustainable elements for rotational actuators," in *2017 IEEE Energy Conversion Congress and Exposition (ECCE)*, Cincinnati, OH, Oct 2017, pp. 2389–2395.

[22] P. L. Chapman and P. T. Krein, "Micromotor technology: electric drive designer's perspective," in *Conference Record of the 2001 IEEE Industry Applications Conference. 36th IAS Annual Meeting (Cat. No.01CH37248)*, vol. 3, Sep. 2001, pp. 1978–1983 vol.3.

[23] S. F. Nagle, "Analysis, Design, and Fabrication of an Electric Induction Micromotor for a Micro Gas-Turbine Generator," Ph.D. dissertation, Massachusetts Institute of Technology, 2000.

[24] L. S. Fan, Y. C. Tai, and R. S. Muller, "IC-processed electrostatic micro-motors," in *Technical Digest., International Electron Devices Meeting*, San Francisco, 1988, pp. 666–669.

[25] B. Bollee, "Electrostatic Motors," *Philips Technical Review*, vol. 30(6/7), pp. 179–194, 1969.

[26] N. Yamashita, A. Yamamoto, M. Gondo, and T. Higuchi, "Evaluation of an electrostatic film motor driven by two-four-phase AC voltage and electrostatic induction," *Proceedings - IEEE International Conference on Robotics and Automation*, no. April, pp. 1572–1577, 2007.

[27] J. G. Trump, "Vacuum electrostatic engineering," Ph.D. dissertation, Massachusetts Institute of Technology, 1933.

[28] N. J. Felici, "Ten years of research on electrostatics at the University of Grenoble 1942-1952," *British Journal of Applied Physics*, vol. 4, no. S2, 1953.

[29] "Shinsei high power electrostatic motor," 2007. [Online]. Available: http://www.shinsei-motor.com/English/techno/

[30] T. Niino, T. Higuchi, and S. Egawa, "Dual excitation multiphase electrostatic drive," in *IAS '95. Conference Record of the 1995 IEEE Industry Applications Conference Thirtieth IAS Annual Meeting*, vol. 2, Orlando, FL, 1995, pp. 1318–1325.

[31] B. Ge, A. N. Ghule, and D. C. Ludois, "A dq-axis framework for electrostatic synchronous machines and charge oriented control," in *2017 IEEE Energy Conversion Congress and Exposition (ECCE)*, Cincinnati, OH, Oct 2017, pp. 2396–2403.

[32] B. Ge, A. Ghule, and D. C. Ludois, "High Torque Density Macro-Scale Electrostatic Rotating Machines: Electrical Design, Generalized d-q Framework & Demonstration," *IEEE Transactions on Industry Applications*, vol. 55, no. 2, pp. 1225–1238, 2018.

[33] B. Ge and D. C. Ludois, "Dielectric liquids for enhanced field force in macro scale direct drive electrostatic actuators and rotating machinery," *IEEE Transactions on Dielectrics and Electrical Insulation*, vol. 23, no. 4, pp. 1924–1934, 2016.

[34] D. C. Ludois and M. J. Erickson, "Self-conforming plates for capacitive machines such as electrostatic motors and generators," 2016.

[35] D. C. Ludois, "Varying capacitance rotating electrical machine," U.S. Patent US 20130106317 A1 , May 2013.

[36] T. C. Neugebauer, D. J. Perreault, J. H. Lang, and C. Livermore, "A Six-Phase Multilevel Inverter for MEMS Electrostatic Induction Micromotors," *IEEE Transactions on Circuits and Systems II: Express Briefs*, vol. 51, no. 2, pp. 49–56, 2004.

[37] B. Wu and M. Narimano, *High-Power Converters and AC Drives*, 2nd ed. New Jersey: John Wiley & Sons, Inc, 2017, ch. Introduction.

[38] A. N. Ghule, P. Killeen, and D. C. Ludois, "Synchronous Electrostatic Machine Torque Modulation via Complex Vector Voltage Control with a Current Source Inverter," *Journal of Emerging and Selected Topics in Power Electronics*, 2020.

[39] M. J. Ryan, R. W. D. Doncker, and R. D. Lorenz, "Decoupled Control of a 4-Leg Inverter via New 4x4 trasformation matrix," *Power Electronics Specialists Conference (PESC)*, vol. 16, no. 5, pp. 187–192, 1999.

[40] D. N. Zmood, D. G. Holmes, C. S. Engineering, and W. Road, "Improved Voltage Regulation For Current Source Inverters," *IEEE Transactions on Industry Applications*, vol. 37, no. 4, pp. 2353–2360, 2000.

[41] S. Rees and U. Ammann, "New stator voltage controller for high speed induction machines fed by current-source inverters," in *IEEE 35th Annual Power Electronics Specialists Conference*, vol. 1, Aachen, Germany, 2004, pp. 541–547.

[42] V. D. Colli, P. Cancelliere, F. Marignetti, and R. D. Stefano, "Voltage control of current source inverters," *IEEE Transactions on Energy Conversion*, vol. 21, no. 2, pp. 451–458, 2006.

[43] J. Espinoza, G. Joos, and P. Ziogas, "Voltage controlled current source inverters," in *Proceedings of the 1992 International Conference on Industrial Electronics, Control, Instrumentation, and Automation*, San Diego, CA, 1992, pp. 512–517 vol. 1.

[44] J. R. Espinoza, G. Joos, J. Guzman, L. Moran, and R. P. Burgos, "Selective harmonic elimination and current/voltage control in current/voltage source topologies: A unified approach," in *IECON'99. Conference Proceedings. 25th Annual Conference of the IEEE Industrial Electronics Society*, vol. 1, San Jose, CA, 1999, pp. 318–323.

[45] D. Novotny and T. A. Lipo, *Vector Control and Dynamics of AC Drives*. Oxford University Press, USA, 1996.

[46] T. M. Rowan and R. J. Kerkman, "A New Synchronous Current Regulator and an Analysis of Current-Regulated PWM Inverters," *IEEE Transactions on Industry Applications*, vol. IA-22, no. 4, pp. 678–690, jul 1986.

[47] M. P. Kazmierkowski and L. Malesani, "Current control techniques for three-phase voltage-source pwm converters: A survey," *IEEE Transactions on Industrial Electronics*, vol. 45, no. 5, pp. 691–703, 1998.

[48] J. Holtz, J. Quan, G. Schmittt, J. Pontt, J. Rodriguez, P. Newman, and H. Miranda, "Design of fast and robust current regulators for high power drives based on complex state variables," *38th IAS Annual Meeting on Conference Record of the Industry Applications Conference, 2003.*, vol. 3, no. 5, pp. 1388–1397, 2003.

[49] Jinhwan Jung and Kwanghee Nam, "A dynamic decoupling control scheme for high-speed operation of induction motors," *IEEE Transactions on Industrial Electronics*, vol. 46, no. 1, pp. 100–110, 1999.

[50] L. Harnefors and H. P. Nee, "Model-based current control of ac machines using the internal model control method," *IEEE Transactions on Industry Applications*, vol. 34, no. 1, pp. 133–141, 1998.

[51] F. Briz del Blanco, M. W. Degner, and R. D. Lorenz, "Analysis and design of current regulators using complex vectors," *IEEE Transactions on Industry Applications*, vol. 36, no. 3, pp. 817–825, 2000.

[52] D. W. Novotny and J. H. Wouterse, "Induction machine transfer functions and dynamic response by means of complex time variables," *IEEE Transactions on Power Apparatus and Systems*, vol. 95, no. 4, pp. 1325–1335, 1976.

[53] H. Kim, M. W. Degner, J. M. Guerrero, F. Briz del Blanco, and R. D. Lorenz, "Discrete-time current regulator design for AC machine drives," *IEEE Transactions on Industry Applications*, vol. 46, no. 4, pp. 1425–1435, jul 2010.

[54] "Advanced Motion Controls DPEANIU-015S400 Datasheet," 2018.

[55] Q. Wei, L. Xing, D. Xu, B. Wu, and N. R. Zargari, "Modulation Schemes for Medium-Voltage PWM Current Source Converter-Based Drives : An Overview," *IEEE Journal of Emerging and Selected Topics in Power Electronics*, vol. 7, no. 2, pp. 1152–1161, 2019.

[56] R. D. Lorenz and K. Van Patten, "High-Resolution Velocity Estimation for All-Digital, ac Servo Drives," *IEEE Transactions on Industry Applications*, vol. 27, no. 4, pp. 701–705, 1991.

[57] H. Kim and R. D. Lorenz, "A virtual translation technique to improve current regulator for salient-pole AC machines," in *IEEE 35th Annual Power Electronics Specialist Conference*, Aachen, Germany, 2004, pp. 487–493.

[58] M. W. Degner and C. M. Wolf, "Transient analysis of asymmetric ac systems using complex vectors," in *2017 IEEE International Electric Machines and Drives Conference (IEMDC)*, Miami, FL, May 2017, pp. 1–8.

[59] A. N. Ghule, P. Killeen, and D. C. Ludois, "High frequency injection based rotor position self-sensing for synchronous electrostatic machines," in *2019 IEEE Energy Conversion Congress and Exposition (ECCE)*, Baltimore, MD, Sep. 2019, pp. 804–811.

[60] "https://www.doigcorp.com."

[61] "https://www.sick.com."

[62] P. L. Jansen and R. D. Lorenz, "Transducerless Position and Velocity Estimation in Induction and Salient AC Machines," *IEEE Transactions on Industry Applications*, vol. 31, no. 2, pp. 240–247, 1995.

[63] R. Wu and G. R. Slemon, "A Permanent Magnet Motor Drive without a Shaft Sensor," *IEEE Transactions on Industry Applications*, vol. 27, no. 5, pp. 1005–1011, 1991.

[64] Joohn-Sheok Kim and Seung-Ki Sul, "New Approach for High-Performance PMSM Drives without Rotational Position Sensors," *IEEE Transactions on Power Electronics*, vol. 12, no. 5, pp. 904–911, 1997.

[65] Y. Xu, C. Morito, and R. D. Lorenz, "Extending high-speed operating range of induction machine drives using deadbeat-direct torque and flux control with precise flux weakening," *IEEE Transactions on Industry Applications*, vol. 55, no. 4, pp. 3770–3780, July 2019.

[66] S. Kim and S. K. Sul, "Sensorless control of AC motor - Where are we now?" *2011 International Conference on Electrical Machines and Systems, ICEMS 2011*, pp. 1–6, 2011.

[67] R. D. Lorenz, "Self-sensing as an integration focus for motor drives and power devices," in *2007 International Conference on Electrical Machines and Systems (ICEMS)*, Seoul, Oct 2007, pp. 386–391.

[68] N. Matsui, "Sensorless operation of brushless DC motor drives," in *Proceedings of IECON '93 - 19th Annual Conference of IEEE Industrial Electronics*, no. 2, Maui, HI, 1993, pp. 739–744.

[69] T. Ohtani, N. Takada, and K. Tanaka, "Vector control of induction motor without shaft encoder," in *Conference Record of the IEEE Industry Applications Society Annual Meeting,*, San Diego, CA, Oct 1989, pp. 500–507 vol.1.

[70] A. B. Kulkarni and M. Ehsani, "A novel position sensor elimination technique for the interior permanent-magnet synchronous motor drive," *IEEE Transactions on Industry Applications*, vol. 28, no. 1, pp. 144–150, Jan 1992.

[71] R. W. Hejny and R. D. Lorenz, "Evaluating the practical low-speed limits for back-EMF tracking-based sensorless speed control using drive stiffness as a key metric," *IEEE Transactions on Industry Applications*, vol. 47, no. 3, pp. 1337–1343, May 2011.

[72] Yoon-Ho Kim and Yoon-Sang Kook, "High performance ipmsm drives without rotational position sensors using reduced-order ekf," *IEEE Transactions on Energy Conversion*, vol. 14, no. 4, pp. 868–873, Dec 1999.

[73] S. Bolognani, R. Oboe, and M. Zigliotto, "Sensorless full-digital pmsm drive with ekf estimation of speed and rotor position," *IEEE Transactions on Industrial Electronics*, vol. 46, no. 1, pp. 184–191, Feb 1999.

[74] Y. Zhao, W. Qiao, and L. Wu, "Improved rotor position and speed estimators for sensorless control of interior permanent-magnet synchronous machines," *IEEE Journal of Emerging and Selected Topics in Power Electronics*, vol. 2, no. 3, pp. 627–639, Sep. 2014.

[75] M. J. Corley and R. D. Lorenz, "Rotor position and velocity estimation for a salient-pole permanent magnet synchronous machine at standstill and high speeds," *IEEE Transactions on Industry Applications*, vol. 34, no. 4, pp. 784–789, July 1998.

[76] Hyunbae Kim, M. C. Harke, and R. D. Lorenz, "Sensorless control of interior permanent-magnet machine drives with zero-phase lag position estimation," *IEEE Transactions on Industry Applications*, vol. 39, no. 6, pp. 1726–1733, Nov 2003.

[77] S. Morimoto, K. Kawamoto, M. Sanada, and Y. Takeda, "Sensorless control strategy for salient-pole pmsm based on extended emf in rotating reference frame," *IEEE Transactions on Industry Applications*, vol. 38, no. 4, pp. 1054–1061, July 2002.

[78] Hejny, Robert W., "Degradation of Dynamic Stiffness at Low Speeds When Using Back-emf Tracking for Closed Loop Speed Control," Master's thesis, University of Wisconsin-Madison, Department of Electrical and Computer Engineering, 2009.

[79] K. Wang, R. D. Lorenz, and N. A. Baloch, "Improvement of back-emf self-sensing for induction machines when using deadbeat-direct torque and flux control," *IEEE Transactions on Industry Applications*, vol. 53, no. 5, pp. 4569–4578, Sep. 2017.

[80] Hyunbae Kim and R. D. Lorenz, "Carrier signal injection based sensorless control methods for ipm synchronous machine drives," in *Conference Record of the 2004 IEEE Industry Applications Conference, 2004. 39th IAS Annual Meeting.*, vol. 2, Seattle, WA, Oct 2004, pp. 977–984 vol.2.

[81] F. Briz, M. W. Degner, J. M. Guerrero, A. Zamarron, and R. D. Lorenz, "Implementation issues affecting the performance of carrier signal injection based sensorless controlled ac drives," in *Conference Record of the 2001 IEEE Industry Applications Conference. 36th IAS Annual Meeting (Cat. No.01CH37248)*, vol. 4, Chicago, IL, Sep. 2001, pp. 2645–2652 vol.4.

[82] F. Briz, A. Diez, and M. W. Degner, "Dynamic operation of carrier-signal-injection-based sensorless direct field-oriented ac drives," *IEEE Transactions on Industry Applications*, vol. 36, no. 5, pp. 1360–1368, Sep. 2000.

[83] F. Cupertino, A. Guagnano, A. Altomare, and G. Pellegrino, "Position estimation delays in signal injection-based sensorless pmsm drives," in *3rd IEEE International*

Symposium on Sensorless Control for Electrical Drives (SLED 2012), Milwaukee, WI, Sep. 2012, pp. 1–6.

[84] P. L. Jansen and R. D. Lorenz, "A physically insightful approach to the design and accuracy assessment of flux observers for field oriented induction machine drives," *IEEE Transactions on Industry Applications*, vol. 30, no. 1, pp. 101–110, Jan 1994.

[85] Y. Yoon, S. Sul, S. Morimoto, and K. Ide, "High-bandwidth sensorless algorithm for ac machines based on square-wave-type voltage injection," *IEEE Transactions on Industry Applications*, vol. 47, no. 3, pp. 1361–1370, May 2011.

[86] D. Raca, P. Garcia, D. Reigosa, F. Briz, and R. D. Lorenz, "A comparative analysis of pulsating vs. rotating vector carrier signal injection-based sensorless control," in *2008 Twenty-Third Annual IEEE Applied Power Electronics Conference and Exposition*, Austin, TX, Feb 2008, pp. 879–885.

[87] A. Athavale, H. Flieh, B. S. Gagas, T. S. Slininger, and R. D. Lorenz, "Machine design for self-sensing," in *2016 IEEE Symposium on Sensorless Control for Electrical Drives (SLED)*, June 2016, pp. 1–10.

[88] F. Briz, M. W. Degner, A. Diez, and R. D. Lorenz, "Static and dynamic behavior of saturation-induced saliencies and their effect on carrier-signal-based sensorless ac drives," *IEEE Transactions on Industry Applications*, vol. 38, no. 3, pp. 670–678, May 2002.

[89] S. Yang and R. D. Lorenz, "Surface permanent magnet synchronous machine position estimation at low speed using eddy-current-reflected asymmetric resistance," *IEEE Transactions on Power Electronics*, vol. 27, no. 5, pp. 2595–2604, May 2012.

[90] E. de M. Fernandes, A. C. Oliveira, A. M. N. Lima, C. B. Jacobina, and W. R. N. Santos, "Self-sensing control of pmsm motor for wide-speed range operation," in *2013 Brazilian Power Electronics Conference*, Gramado, Oct 2013, pp. 814–820.

[91] G. Andreescu, C. I. Pitic, F. Blaabjerg, and I. Boldea, "Combined flux observer with signal injection enhancement for wide speed range sensorless direct torque control of ipmsm drives," *IEEE Transactions on Energy Conversion*, vol. 23, no. 2, pp. 393–402, June 2008.

[92] M. Schrodl, M. Hofer, and W. Staffler, "Sensorless control of pm synchronous motors in the whole speed range including standstill using a combined inform/emf model," in *2006 12th International Power Electronics and Motion Control Conference*, Portoroz, Aug 2006, pp. 1943–1949.

[93] G. Wang, R. Yang, and D. Xu, "Dsp-based control of sensorless ipmsm drives for wide-speed-range operation," *IEEE Transactions on Industrial Electronics*, vol. 60, no. 2, pp. 720–727, Feb 2013.

[94] H. Flieh, T. Slininger, R. D. Lorenz, and E. Totoki, "Self-sensing via flux injection with servo dynamics including a smooth transition to back-emf tracking," in *2018 IEEE Energy Conversion Congress and Exposition (ECCE)*, Portland, OR, Sep. 2018, pp. 1762–1769.

[95] A. Griffo, D. Drury, T. Sawata, and P. H. Mellor, "Sensorless starting of a wound-field synchronous starter/generator for aerospace applications," *IEEE Transactions on Industrial Electronics*, vol. 59, no. 9, pp. 3579–3587, Sep. 2012.

[96] H.-Q. Nguyen and S.-M. Yang, "Comparison of High Frequency Voltage Injection Methods for Shaft Sensorless Control of Wound-Field Flux Switching Machine," in *2018 International Power Electronics Conference (IPEC-Niigata 2018 -ECCE Asia)*. IEEE, may 2018, pp. 3426–3430.

[97] A. Rambetius and B. Piepenbreier, "Sensorless control of wound rotor synchronous machines using the switching of the rotor chopper as a carrier signal," in *2013 IEEE International Symposium on Sensorless Control for Electrical Drives and Predictive Control of Electrical Drives and Power Electronics (SLED/PRECEDE)*, Munich, Oct 2013, pp. 1–8.

[98] Jongwon Choi, Ilsu Jeong, Kwanghee Nam, and Sungyoon Jung, "Sensorless control for electrically energized synchronous motor based on signal injection to field winding," in *IECON 2013 - 39th Annual Conference of the IEEE Industrial Electronics Society*, Vienna, Nov 2013, pp. 3120–3129.

[99] S. Rajan, S. Wang, and R. Inkol, "Efficient approximations for the four-quadrant arctangent function," *Canadian Conference on Electrical and Computer Engineering*, no. May, pp. 1043–1046, 2007.

[100] P. Killeen, A. N. Ghule, and D. C. Ludois, "Silicon carbide jfet super-cascodes for normally-on current source inverter switches in medium voltage variable speed electrostatic drives," in *2019 IEEE Energy Conversion Congress and Exposition (ECCE)*, Baltimore, MD, Sep. 2019, pp. 4004–4011.

[101] D. E. Borgard, "Physical Parameter Estimation for a Field Oriented Induction Machine," Master's thesis, University Of Wisconsin-Madison, 1994.

[102] D. E. Borgard, G. Olsson, and R. D. Lorenz, "Accuracy issues for parameter estimation of field oriented induction machine drives," *IEEE Transactions on Industry Applications*, vol. 31, no. 4, pp. 795–801, July 1995.

[103] A. N. Ghule, "Online Parameter Estimation for Surface Permanent Magnet Machines," Master's thesis, University of Wisconsin-Madison, 2013.

[104] W. Karsten, "Positionsgeberloser Betrieb von permanentmagneterregten Synchronmaschinen (Positionless operation of permanent magnet synchronous machines)," Ph.D. dissertation, University of Hanover, 2012.

[105] K. Wiedmann and A. Mertens, "Self-sensing control of PM synchronous machines including online system identification based on a novel MRAS approach," *3rd IEEE International Symposium on Sensorless Control for Electrical Drives, SLED 2012*, pp. 1–8, 2012.

[106] K. Hyunbae, "On-line Parameter Estimation, Current Reglation and Self Sensing for IPM Synchronous," Ph.D. dissertation, University of Wisconsin-Madison, 2004.

[107] K. Wang, "Investigation of Parameter Estimation Methodologies for Deadbeat-Direct Torque and Flux Control of IMs using Back-EMF Tracking for Motion Self-Sensing by," Ph.D. dissertation, University of Wisconsin - Madison, 2018.

[108] Peiyuan Li, Jianwen Zhang, Jiacheng Wang, and Xu Cai, "A new design method for the dc inductance in current source converters," in *IECON 2016 - 42nd Annual Conference of the IEEE Industrial Electronics Society*, Florence, Oct 2016, pp. 3160–3165.

[109] Texas Instruments, "ControlSUITE^{TM} Software Suite: Software and Development Tools for C2000^{TM} Microcontrollers." [Online]. Available: http://www.ti.com/tool/CONTROLSUITE

APPENDIX A

Parameter Estimation for Electrostatic Machines

The dynamic performance of the controller is directly related to the accuracy of machine parameters used for the controller tuning. The performance of these controllers can be improved by increasing the accuracy of machine parameters. Continuous online estimation of parameters can aid in increasing the operating range of the machine. Along with improving controller performance, methods of parameter estimation also provide an insight into machine state-of-health. Parameter estimates can be used for diagnostic purposes for understanding degradation in machine state. This section provides a basic insight into the machine parameters as seen by the machine drive. The machine capacitance and resistance which form the basis of tuning the voltage regulator and the primary parameters building the voltage observe used for back-mmf state estimation.

A.1 A review of the State of the Art

Online and offline parameter estimation are a crucial aspect of VFD commissioning and operation. High performance VFD's rely on some sort of parameter estimation to obtain machine properties which allows configuring the bandwidths of controllers without causing unstable operation. Diagnostic parameter estimation algorithms are also implemented which monitor the state of health of the machine and allow for safe shut if there is a possibility of a failure.

Parameter estimation methods in machines range from machine estimates obtained

before commissioning a drive for design verification to continuous online estimation. Multiple methods investigating parameter estimation using time series methods have been investigated in literature [101–103]. Use of model reference adaptive control (MRAC) based methods for estimation of machine parameters is shown in[103–105]. The MRAC methods are implemented with observers for converging on online estimates or parameters by driving the error associated with the estimated state variable to zero.

Along with MRAC methods, [106] has developed machine model based methods for estimation of machine parameters. [107] details the use of MRAC based parameter estimation methods for improving machine parameter estimates. These parameters are used for improving self-sensing performance.

A.2 Steady State Parameter Estimation for SEM

The parameters of the SEM can be estimated from the machine model used with the measured voltages and the steady state terms removed. The steady state models of the machine for estimation of machine capacitances using a machine voltage observer in the synchronous reference frame are shown below.

A.2.1 Steady state machine model

The steady state model of an SEM is shown in (A.1) ,(A.2).

$$I^e_{qs} = \frac{V^e_{qs}}{\hat{R}_s} + \omega_e \hat{C}_d V^e_{ds} - \omega_e \hat{C}_{md} V_{fd} \tag{A.1}$$

$$I^e_{ds} = \frac{V^e_{ds}}{\hat{R}_s} - \omega_e \hat{C}_q V^e_{qs} \tag{A.2}$$

A.2.2 Machine resistance estimation

A variable resistance load bank is used to investigate the effect of drive non-linearities on resistance estimation. A 10 Hz, 10 mA current is injected in the RC load bank with a constant capacitance of 10 nF and resistances varying from 100kΩ to 500kΩ and the normalized resistance estimate is shown in Fig. A.1. It can be seen that the resistance estimate at 500kΩ is only 20% of the actual value. This is attributed to the fact that the DC bus is at 100mA and only 8 mA current will be flowing through the resistance. Any errors

in the actual value of the resistance will be reflected as errors in parameter estimation. The state-of-health of the liquid can be monitored by estimating the machine resistance using the injection method.

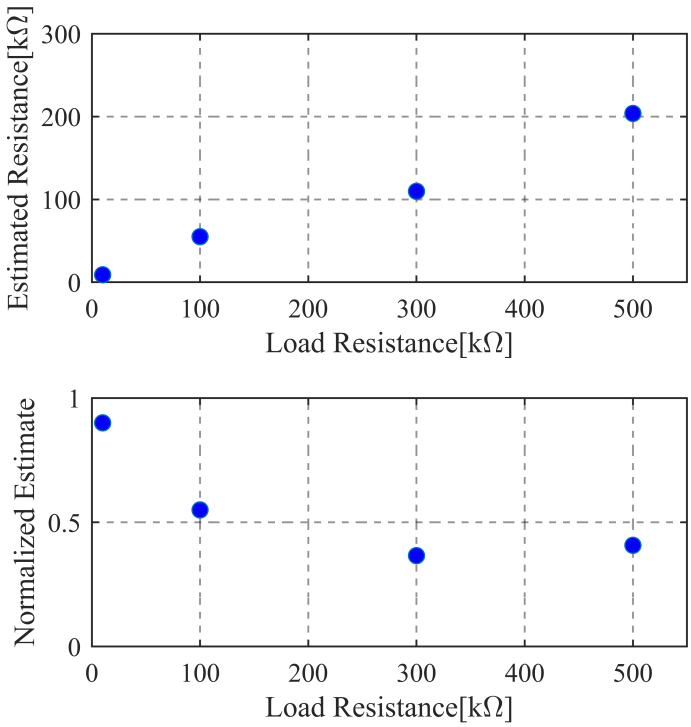

Figure A.1, Normalized resistance estimates at different load resistances using an injected current of 10 mA at 10 Hz in the q-axis

A.2.3 Machine capacitance estimation

The machine capacitance is estimated by injecting a high frequency signal in the machine measuresing the resultant voltage waveforms. A 10mA 200 Hz sine wave signal is injected in the machine and the resulting voltage is measured. The capacitance value is extracted using the machine steady state model in (A.1)-(A.1). The estimated capacitance vs the actual capacitance used in the RC load is shown in Fig. A.2. The values of the estimated capacitance are higher than the actual values. This is possible due to the additional parallel parasitic capacitance across the CSI due to :

- The CSI is connected with the RC load using coaxial cables which introduce an addition line capacitance in the order of 30pF per foot of coaxial cable.
- The CSI switches have parasitic capacitance which is used for balancing the series-stack voltages.

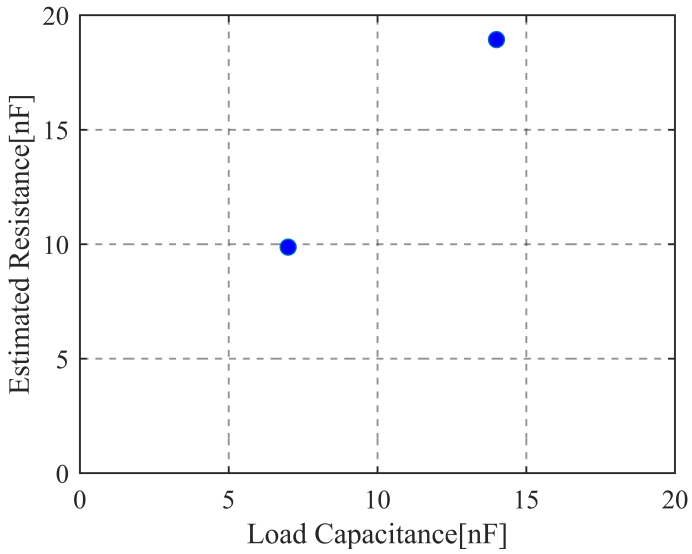

Figure A.2, Normalized resistance estimates at different load resistances using an injected current of 10 mA at 10 Hz in the q-axis

A.2.4 Fluid heath estimate monitoring using field voltage power

The SEM uses a high voltage DC-DC supply to provide the separate excitation. The DC supply steps up a 0-12V input to a 0-4kV excitation. The dielectric fluid used for the machine becomes resistive due to impurities. The increase in resistivity is reflected in the form of additional power required to support the same field voltage with the DC supply. A measurement of the current required by the DC supply can provide an insight about the state-of-health of the fluid in the machine.

A.3 Summary

The capacitance and resistance of the machine are estimated and the effect of the drive harmonics is highlighted at the relatively high resistance values.

APPENDIX B

Firmware Development for SEM Control Platform

This section details the software development for the complete hardware control setup including the front-end current source and the current source inverter platform for controlling the electrostatic machine.

B.1 Space Vector Modulation Configuration for CSI

The space vector modulation for the CSI was implemented on the DSP platform without any additional hardware. This was achieved using varying PWM configuration modes for the PWM in every sector.

Table B.1, Sector Changes

Sector	SW A	SW B	SW0
1	6	2	4
2	1	3	5
3	2	4	6
4	3	5	1
5	4	6	2
6	5	7	3

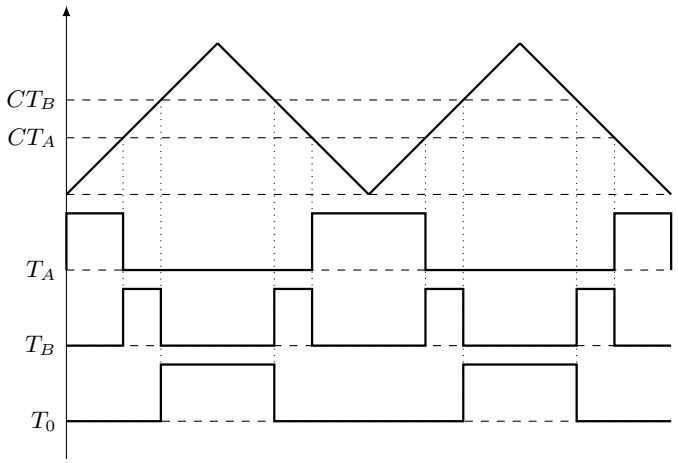

Figure B.1, Switching states for CSI modulation in a switching period

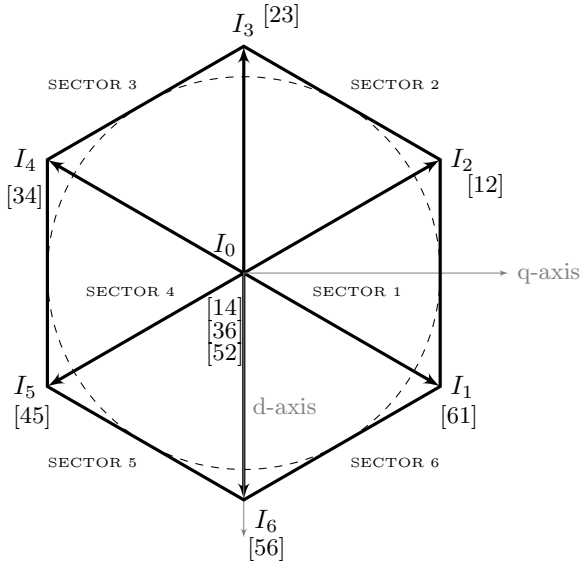

Figure B.2, Space vector modulation for CSI

There are multiple configurations which can be selected for setting the sequence of A, B and zero states in every switch period. Figure B.1 shows the sequence of switches for achieving a symmetric PWM. A comprehensive evaluation of ripple content due to the different modulation sequences is presented in [108].

The CSI requires a different switch to perform the TA and TB switch times in each sector. To achieve this, the PWM configuration of the CSI platform is changed in every sector. The TI28379MCU offers shadow registers to delay the configuration update at the end of the sector and align with the next PWM time instant. The configuration of the PWM channels for the higher switches and the lower switches is different to take advantage of the internal deadband generator for generating overlap time for the CSI. The configuration of the switches for each sector configuration is given in B.1. The variable definitions are imported from the header file 'F2837xD_GlobalVariableDefs.c' [109].

DSP and MATLAB Code B.1, PWM configuration setup

```
void PWM_allch_deadtime(int16 n, int16 dtA){
    (*ePWM[n]).DBCTL.bit.IN_MODE = DBA_RED_DBB_FED;
    (*ePWM[n]).DBCTL.bit.OUT_MODE = DB_FULL_ENABLE;
    (*ePWM[n]).DBRED = dtA;
    (*ePWM[n]).DBFED = dtA;
    (*ePWM[n]).DBCTL.bit.POLSEL = DB_ACTV_LOC ;
}
void PWM_oddch_T0_CNF(int16 n){
   (*ePWM[n]).AQCTLA.bit.ZRO = AQ_CLEAR;
   (*ePWM[n]).AQCTLA.bit.PRD = AQ_CLEAR;
    (*ePWM[n]).AQCTLA.bit.CBU = AQ_NO_ACTION ;
    (*ePWM[n]).AQCTLA.bit.CBD = AQ_NO_ACTION ;
    (*ePWM[n]).AQCTLA.bit.CAU = AQ_NO_ACTION ;
    (*ePWM[n]).AQCTLA.bit.CAD = AQ_NO_ACTION ;
    (*ePWM[n]).AQCTLB.bit.ZRO = AQ_CLEAR;

    (*ePWM[n]).AQCTLB.bit.CBU = AQ_SET; //T0
    (*ePWM[n]).AQCTLB.bit.CBD = AQ_CLEAR; //T0
    (*ePWM[n]).AQCTLB.bit.CAU = AQ_NO_ACTION ; //T0
    (*ePWM[n]).AQCTLB.bit.CAD = AQ_NO_ACTION ; //T0
}
void PWM_oddch_TA_CNF(int16 n){
```

```
    (*ePWM[n]).AQCTLA.bit.ZRO = AQ_SET;
    (*ePWM[n]).AQCTLA.bit.PRD = AQ_SET;
    (*ePWM[n]).AQCTLA.bit.CBU = AQ_NO_ACTION ;
    (*ePWM[n]).AQCTLA.bit.CBD = AQ_NO_ACTION ;
    (*ePWM[n]).AQCTLA.bit.CAU = AQ_NO_ACTION ;
    (*ePWM[n]).AQCTLA.bit.CAD = AQ_NO_ACTION ;
    (*ePWM[n]).AQCTLB.bit.ZRO = AQ_SET;
    (*ePWM[n]).AQCTLB.bit.CBU = AQ_CLEAR; //TA
    (*ePWM[n]).AQCTLB.bit.CAD = AQ_SET; //TA
    (*ePWM[n]).AQCTLB.bit.CAU = AQ_NO_ACTION ; //TA
    (*ePWM[n]).AQCTLB.bit.CBD = AQ_NO_ACTION ; //TA
}
void PWM_oddch_TB_CNF(int16 n ){
    (*ePWM[n]).AQCTLA.bit.ZRO = AQ_SET;
    (*ePWM[n]).AQCTLA.bit.PRD = AQ_SET;
    (*ePWM[n]).AQCTLA.bit.CBU = AQ_NO_ACTION ;
    (*ePWM[n]).AQCTLA.bit.CBD = AQ_NO_ACTION ;
    (*ePWM[n]).AQCTLA.bit.CAU = AQ_NO_ACTION ;
    (*ePWM[n]).AQCTLA.bit.CAD = AQ_NO_ACTION ;
    (*ePWM[n]).AQCTLB.bit.ZRO = AQ_CLEAR;
    (*ePWM[n]).AQCTLB.bit.CAU = AQ_SET;
    (*ePWM[n]).AQCTLB.bit.CBU = AQ_CLEAR;
    (*ePWM[n]).AQCTLB.bit.CBD = AQ_SET;
    (*ePWM[n]).AQCTLB.bit.CAD = AQ_CLEAR;
}
void PWM_evench_T0_CNF(int16 n){
    (*ePWM[n]).AQCTLA.bit.ZRO = AQ_SET;
    (*ePWM[n]).AQCTLA.bit.CBU = AQ_CLEAR; //T0
    (*ePWM[n]).AQCTLA.bit.CBD = AQ_SET; //T0
    (*ePWM[n]).AQCTLA.bit.PRD = AQ_CLEAR; //T0
    (*ePWM[n]).AQCTLA.bit.CAU = AQ_NO_ACTION ; //T0
    (*ePWM[n]).AQCTLA.bit.CAD = AQ_NO_ACTION ; //T0
    (*ePWM[n]).AQCTLB.bit.CBU = AQ_NO_ACTION ;
    (*ePWM[n]).AQCTLB.bit.CBD = AQ_NO_ACTION ;
    (*ePWM[n]).AQCTLB.bit.CAU = AQ_NO_ACTION ;
    (*ePWM[n]).AQCTLB.bit.CAD = AQ_NO_ACTION ;
```

```
    (*ePWM[n]).AQCTLB.bit.ZRO = AQ_SET;
}
void PWM_evench_TA_CNF(int16 n){
    (*ePWM[n]).AQCTLA.bit.ZRO = AQ_CLEAR; //TA
    (*ePWM[n]).AQCTLA.bit.CBU = AQ_SET; //TA
    (*ePWM[n]).AQCTLA.bit.CAD = AQ_CLEAR;//TA
    (*ePWM[n]).AQCTLA.bit.PRD = AQ_SET;//TA
    (*ePWM[n]).AQCTLA.bit.CAU = AQ_NO_ACTION ; //TA
    (*ePWM[n]).AQCTLA.bit.CBD = AQ_NO_ACTION ; //TA
    (*ePWM[n]).AQCTLB.bit.ZRO = AQ_CLEAR;
    (*ePWM[n]).AQCTLB.bit.CBU = AQ_NO_ACTION ;
    (*ePWM[n]).AQCTLB.bit.CBD = AQ_NO_ACTION ;
    (*ePWM[n]).AQCTLB.bit.CAU = AQ_NO_ACTION ;
    (*ePWM[n]).AQCTLB.bit.CAD = AQ_NO_ACTION ;
}
void PWM_evench_TB_CNF(int16 n ){
    (*ePWM[n]).AQCTLA.bit.PRD = AQ_SET;
    (*ePWM[n]).AQCTLA.bit.ZRO = AQ_SET;
    (*ePWM[n]).AQCTLA.bit.CAU = AQ_CLEAR; //TB
    (*ePWM[n]).AQCTLA.bit.CBU = AQ_SET; //TB
    (*ePWM[n]).AQCTLA.bit.CBD = AQ_CLEAR; //TB
    (*ePWM[n]).AQCTLA.bit.CAD = AQ_SET; //TB
    (*ePWM[n]).AQCTLB.bit.ZRO = AQ_CLEAR;
    (*ePWM[n]).AQCTLB.bit.CBU = AQ_NO_ACTION ;
    (*ePWM[n]).AQCTLB.bit.CBD = AQ_NO_ACTION ;
    (*ePWM[n]).AQCTLB.bit.CAU = AQ_NO_ACTION ;
    (*ePWM[n]).AQCTLB.bit.CAD = AQ_NO_ACTION ;
}
```

DSP and MATLAB Code B.2, PWM compare value updates

```
//Compare update functions
void PWM_oddch_T0_CMP(int16 n, Uint16 T0){
    (*ePWM[n]).CMPB.bit.CMPB = T0;
}

void PWM_oddch_TA_CMP(int16 n, Uint16 TA){
```

```
    (*ePWM[n]).CMPA.bit.CMPA = TA;
    (*ePWM[n]).CMPB.bit.CMPB = TA;
}

void PWM_oddch_TB_CMP(int16 n, Uint16 TA , Uint16 TB ){
    (*ePWM[n]).CMPA.bit.CMPA = TA;
    (*ePWM[n]).CMPB.bit.CMPB = TB;
}

void PWM_evench_T0_CMP(int16 n, Uint16 T0){
    (*ePWM[n]).CMPB.bit.CMPB = T0;
}

void PWM_evench_TA_CMP(int16 n, Uint16 TA){
    (*ePWM[n]).CMPA.bit.CMPA = TA;
    (*ePWM[n]).CMPB.bit.CMPB = TA;
}

void PWM_evench_TB_CMP(int16 n, Uint16 TA , Uint16 TB ){
    (*ePWM[n]).CMPA.bit.CMPA = TA;
    (*ePWM[n]).CMPB.bit.CMPB = TB;
}
```

B.2 Front-End PWM Configuration

The CSI setup requires a DC current source rated for the high voltage required for the CSI. The front-end consists of a DC voltage supply connected to a high frequency H-Bridge inverter. The inverter voltage is stepped up using a high frequency transformer which is then fed into a diode rectifier to provide the DC current required for the CSI. The DC link inductors provide filtering to smooth the rectified current. The front-end hardware along with the CSI is shown in Fig. B.3.

The diodes used for rectifying the DC current allow a unidirectional operation of the front end. Active switches can be used for a bidirectional operation. The PWM configuration used for controlling the DC link current is shown in Fig. B.4 where switch 6A and 7A use the SW_A pulse and 6B and 7B use the SW_B pulse. The DC link current is sensed to

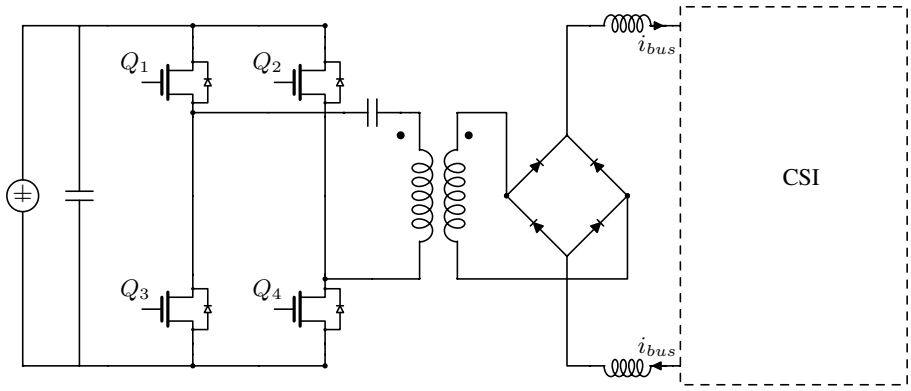

Figure B.3, Front-end circuit diagram showing H-Bridge, high frequency transformer and rectifier

close a loop on the rectified current. The switch configuration for the front-end PWM is shown in Fig. B.4.

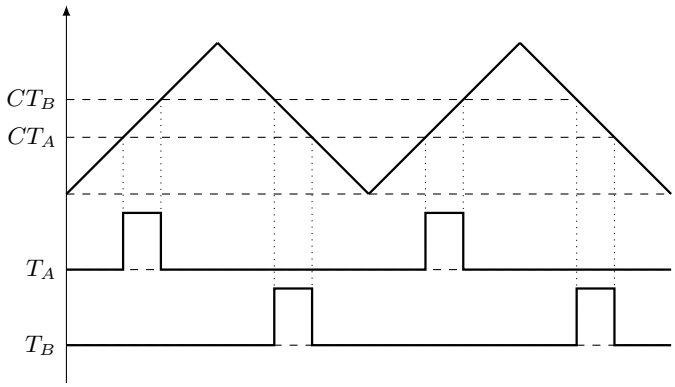

Figure B.4, Switching states of H-Bridge for DC current source front end

The DC current converter is operated at 20 kHz with the sensing and computations running on a separate interrupt at 20 kHz. The DC link inductors carry the burden of providing a stiff current source which allows a low bandwidth of 5 Hz to be chosen for the closed loop current control. A feedforward command from the CSI is fed to the front-end. This allows a reduced DC link current disturbance for dynamic changes in CSI load along with allowing a reasonable bandwidth for the current regulator. A block diagram of the front-end controller is shown in Fig. B.5 where k_p and k_i are gains of the PI regulator and k_{ffw} is the feedforward gain.

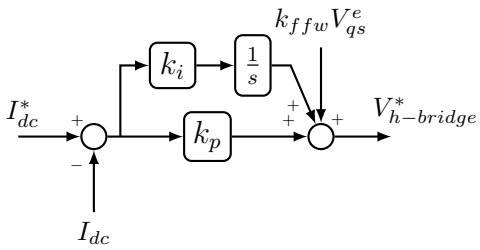

Figure B.5, Block diagram of DC bus current regulator showing inverter command feed-forward

B.3 Voltage Regulator

The DSP implementation for the complex vector d and q-axis synchronous reference frame voltage regulator is given in B.3.

DSP and MATLAB Code B.3, Complex Vector Voltage Regulator

```
// Structure for voltage regulator
struct cvv { float32 star ,fbk , kp , ki , err , acc_err , out , temp; };
struct cvv vq = { 0 , 0 ,0 ,0 , 0 , 0 , 0 , 0};
struct cvv vd = { 0 , 0 ,0 ,0 , 0 , 0, 0 , 0};

if(motor_on ==1)
{
        vq.fbk = v_e.q;
        vq.err = vq.star − vq.fbk;
        vq.acc_err += vq.err ;
        vd.fbk = v_e.d;
        vd.err = id.star − vd.fbk;
        vd.acc_err += vd.err ;

        vq.out = vq.err ∗ vq.kp + vq.ki ∗ vq.acc_err∗T + we_fbk ∗ vd.kp ∗ vd.acc_err ∗T ; //Q−axis
            ↪ Current Command
        vd.out = vd.err ∗ vd.kp + vd.ki ∗ vd.acc_err∗T − we_fbk ∗ vq.kp ∗ vq.acc_err ∗T; //D−axis
            ↪ Current Command
}
```

B.4 Self-Sensing

This section includes code for implementation of DSP code for rotor position self-sensing for the SEM.

B.4.1 Back-MMF based self-sensing

The DSP implementation of a stationary reference frame voltage observer which acts as a back-mmf state filter is shown in B.4. The voltage observer provides an estimate of the dq-axis back-mmf. The output of the voltage observer is then used with a position observer to extract position information.

DSP and MATLAB Code B.4, Voltage Observer

```
//Structure for Observer
struct obs {float hat, fbk, err, acc_err, kp, ki , V_pi, V_total,V_command;};
struct obs iq_obs = { 0, 0, 0, 0, 0, 0 , 0, 0, 0};//ki, kp values to be initialized depending on Lp_hat.
struct obs id_obs = { 0, 0, 0, 0, 0, 0 , 0, 0,0};

if(current_obs_en ==1)
{
        vq_obs.fbk = v_s.q;    //Input stationary frame voltage
        vq_obs.err = vq_obs.hat − vq_obs.fbk;
        vq_obs.acc_err += vq_obs.err;
        vq_obs.V_pi = vq_obs.err∗iq_obs.kp + iq_obs.acc_err∗iq_obs.ki∗T; //Back Emf Estimation
        vq_obs.V_total = iq_obs.V_pi + iq_obs.V_command; //Voltage command feedforward,
            ↪ connect V_command to VSI command

        id_obs.fbk = i_s.d;    //Input stationary frame current
        id_obs.err = id_obs.hat − id_obs.fbk;
        id_obs.acc_err += id_obs.err;
        id_obs.V_pi = id_obs.err∗iq_obs.kp + id_obs.acc_err∗id_obs.ki∗T; //Back Emf estimation
        id_obs.V_total = id_obs.V_pi + id_obs.V_command; //Voltage command feedforward,
            ↪ connect V_command to VSI command

        iq_obs.hat += (iq_obs.V_total − iq_obs.hat∗Rp_hat)∗Lp_hat_inv; //Machine Model
        id_obs.hat += (id_obs.V_total − id_obs.hat∗Rp_hat)∗Lp_hat_inv; //Machine Model
}
```

APPENDIX C

Steady State Performance Curves for SEM

C.1 Stator Side Field Weakening

In this simulation, the field is weakened by increasing d-axis voltage to reduce back-mmf. The field voltage is selected as -8kV to generate a positive torque for a positive q-axis voltage.

DSP and MATLAB Code C.1, Stator Side Field Weakening

```
clear all
close all
Vq = 4000;Vd = 0;
Vs_lim = 4000;
Vfd = −8000;
Cmd = 2.2e−9; Cs = 13.8e−9;
RPM = 0:1:1000;
wr = 2∗pi∗RPM/60;
P = 96;
we = P∗wr;
%Computation of field weakening speed based on available voltage and bus current
Ibus = 0.2;
w_max =(Ibus)∗sqrt(1/((−Cmd∗Vfd)^2+(Cs∗Vs_lim)^2));
w_max2 = (Ibus)./sqrt((Cs∗Vs_lim)^2 −(Cmd∗Vfd)^2 );
```

```
    sin_angle = 0.*(we<=w_max)...
                    + (we<w_max2).*(we>w_max).*((Ibus^2 - we.*we*(Vs_lim*Vs_lim*Cs*Cs +
                        ↪ Cmd*Cmd*Vfd*Vfd))./(-2*we.^2*Cmd*Cs*Vfd*Vs_lim))...
                    + (we>w_max2).*Vfd*Cmd/(Vs_lim*Cs);
    cos_angle = sqrt(1-sin_angle.^2);

Vq = Vs_lim*cos_angle.*(we<=w_max2) +(we>w_max2)*Ibus./(Cs*we);
Vd = Vs_lim*sin_angle.*(we<=w_max2) + (we>w_max2)*Cmd*Vfd/Cs;
Vf = ones(1,length(RPM))*Vfd;
id = -we*Cs.*Vq;
iq = Cs*we.*Vd - Cmd*Vf.*we;
I = sqrt(id.^2 + iq.^2);
Te = -(3/2)*P*Cmd*Vf.*Vq;
V_out = sqrt(Vd.^2 + Vq.^2 );

%Plot machine performance plots
f1 =figure('Units', 'inches', ...
    'Position', [1 1 5 5]);
sb1 = subplot(5,1,1);
plot(RPM,I,'LineWidth',3);
sb1.YLabel.String = 'Current [A]';
ylim([0 0.25]);

sb2 = subplot(5,1,2);
hold on
plot(RPM,V_out/1e3,'LineWidth',3)
sb2.YLabel.String = 'Voltage [kV]';
ylim([0 5]);
yticks([0 2.5 5]);

sb3 = subplot(5,1,3);
plot(RPM,Te,'LineWidth',3);
ylim([0 11]);
yticks([0 5 10]);
sb3.YLabel.String = 'Torque [Nm]';
```

```
sb4 = subplot(5 ,1,4);
plot(RPM,Te.*wr/1000,'LineWidth',3);
ylim([0 0.5]);
sb4.YLabel.String = 'Power [kW]';

sb5 = subplot(5 ,1,5);
plot(RPM,(Te.*wr)./(1.5*V_out.*I),'LineWidth',3);
ylim([0 01]);
sb5.YLabel.String = 'Power factor';
sb5.XLabel.String = 'Speed [RPM]';
%%
f2 =figure('Units', 'inches', ...
    'Position', [1 1 5 1.5]);
hold on
plot(RPM,Vq/1e3,'LineWidth',3)
plot(RPM,Vd/1e3,'LineWidth',3)
plot(RPM,Vf/1e3,'LineWidth',3,'Color','k')
sb1 = gca;
sb1.YLabel.String = 'Voltage [kV]';
sb1.XLabel.String = 'Speed [RPM]';
ylim([-10 6]);
%%
f3 =figure('Units', 'inches', ...
    'Position', [1 1 5 1.5]);
hold on
plot(RPM,iq,'LineWidth',3)
plot(RPM,id,'LineWidth',3)
plot(RPM,I,'LineWidth',3,'Color','k')
sb1 = gca;
ylim([-.25 .25]);
sb1.YLabel.String = 'Current [A]';
sb1.XLabel.String = 'Speed [RPM]';
```

C.2 Rotor Side Field Weakening

In this simulation, the field is weakened by reducing the rotor field to reduce back-mmf. The field voltage is selected as -8kV to generate a positive torque for a positive q-axis voltage.

DSP and MATLAB Code C.2, Rotor Side Field Weakening

```
%%SEM Torque Speed Curves
clear all
close all
Vq = 4000;Vd = 0;
Vs_lim = 4000;
Vfd = −8000;
Cmd = 2.2e−9; Cs = 13.8e−9;
RPM = 0:1:362;
wr = 2∗pi∗RPM/60;
P = 96;
we = P∗wr;
%Compute maximum speed based on voltage limit, machine parameters and bus current
Ibus = 0.2;
w_max =(Ibus)∗sqrt(1/((−Cmd∗Vfd)^2+(Cs∗Vs_lim)^2));
Vq = ones(1,length(RPM))∗Vs_lim;
Vd = ones(1,length(RPM))∗0;
Vf = Vfd.∗(we<w_max) + −(we>=w_max).∗sqrt(Ibus^2./(we.^2∗Cmd^2) − Vs_lim^2∗Cs^2/(Cmd
    ↪ ^2));
id = −we∗Cs.∗Vq;
iq = Cs∗we.∗Vd − Cmd∗Vf.∗we;
I = sqrt(id.^2 + iq.^2);
Te = −(3/2)∗P∗Cmd.∗Vf.∗Vq;
V_out = sqrt(Vd.^2 + Vq.^2 );
%Plot machine performance plots
f1 =figure('Units', 'inches', ...
    'Position', [1 1 5 7]);
sb1 = subplot(6,1,1);
plot(RPM,I,'LineWidth',3);
sb1.YLabel.String = 'Current[A]';
ylim([0 0.25]);
```

```
xlim([0 362]);

sb2 = subplot(6,1,2);
hold on
plot(RPM,V_out/1e3,'LineWidth',3)
sb2.YLabel.String = 'Voltage [kV]';
ylim([0 5])
yticks([0 2.5 5]);

xlim([0 362])
sb3 = subplot(6,1,4);
plot(RPM,Te,'LineWidth',3);
ylim([0 11])
sb3.YLabel.String = 'Torque [Nm]';
xlim([0 362]);

sb4 = subplot(6 ,1,5);
plot(RPM,Te.*wr/1000,'LineWidth',3);
ylim([0 0.5]);
xlim([0 362]);
sb4.YLabel.String = 'Power [kW]';

sb5 = subplot(6 ,1,6);
plot(RPM,(Te.*wr)./(1.5*V_out.*I),'LineWidth',3);
ylim([0 01]);
xlim([0 362]);
sb5.YLabel.String = 'Power factor';
sb5.XLabel.String = 'Speed [RPM]';

sb5 = subplot(6 ,1,3);
plot(RPM,(Vf/1e3),'LineWidth',3);
ylim([-10 0]);
xlim([0 362]);
sb5.YLabel.String = 'Field [kV]';
```